Anaplerotic nutrient stress drives synergy of angiogenesis inhibitors with therapeutics targeting tumor metabolism

Sunada Khadka[1,2,3], Yu-Hsi Lin[2], Jeffrey Ackroyd[2,3], Yi-An Chen[4], Yanghui Sheng[5], Wubin Qian[5], Sheng Guo[5], Yining Chen[2], Eliot Behr[2], Yasaman Barekatain[1,2,3], Md. Nasir Uddin[2], Kenisha Arthur[2], Victoria Yan[1,3], Wen-Hao Hsu[1], Qing Chang[6], Anton Poral[2], Theresa Tran[2], Surendra Chaurasia[1], Dimitra K. Georgiou[2], John M. Asara[6], Floris P. Barthel[4], Steve W. Millward[2], Ronald A. DePinho[1], and Florian L. Muller[2,3,8]*.

1. Department of Cancer Biology, The University of Texas MD Anderson Cancer Center, Houston, TX, USA
2. Department of Cancer Systems Imaging, The University of Texas MD Anderson Cancer Center, Houston, TX, USA
3. MD Anderson UT Health Graduate School of Biomedical Sciences, Houston, TX, USA
4. Cancer and Cell Biology Division, The Translational Genomics Research Institute (TGen), Phoenix, AZ, USA
5. Crown Bioscience Inc., Suzhou Industrial Park, 218 Xinghu Rd, Jiangsu, China
6. Department of Genomic Medicine, The University of Texas MD Anderson Cancer Center, Houston, TX, USA
7. Department of Medicine, Beth Israel Deaconess Medical Center and Harvard Medical School, Boston, MA, USA
8. Present address: Sporos Bioventures, Houston, TX, USA

*Corresponding author

ABSTRACT

Tumor angiogenesis is a cancer hallmark, and its therapeutic inhibition has provided meaningful, albeit limited, clinical benefit. While anti-angiogenesis inhibitors deprive the tumor of oxygen and essential nutrients, cancer cells activate metabolic adaptations to diminish therapeutic response. Despite these adaptations, angiogenesis inhibition incurs extensive metabolic stress, prompting us to consider such metabolic stress as an *induced vulnerability* to therapies targeting cancer metabolism. Metabolomic profiling of angiogenesis-inhibited intracranial xenografts showed universal decrease in tricarboxylic acid cycle intermediates, corroborating a state of anaplerotic nutrient deficit or stress. Accordingly, we show strong synergy between angiogenesis inhibitors (Avastin, Tivozanib) and inhibitors of glycolysis or oxidative phosphorylation through exacerbation of anaplerotic nutrient stress in intracranial orthotopic xenografted gliomas. Our findings were recapitulated in GBM xenografts that do not have genetically predisposed metabolic vulnerabilities at baseline. Thus, our findings cement the central importance of the tricarboxylic acid cycle as the nexus of metabolic vulnerabilities and suggest clinical path hypothesis combining angiogenesis inhibitors with pharmacological cancer interventions targeting tumor metabolism for GBM tumors.

41 **INTRODUCTION**

42 Angiogenesis inhibitors, particularly Avastin, a humanized, anti-hVEGFA monoclonal
43 antibody, have become a mainstay for the treatment of vascularized solid tumors as a first line or
44 second line therapy[1]. Avastin significantly restricts blood flow to the tumor and given in
45 combination with chemotherapy, can elicit a survival benefit in some cancers[2,3]. However, the
46 tumor static effects of angiogenesis inhibition are often transient due to a multitude of cancer cell
47 intrinsic and extrinsic adaptive mechanisms[4–6]. Despite this limitation, anti-angiogenic therapies
48 such as Avastin still remain important in the treatment of many cancer types, including
49 glioblastoma multiforme (GBM), which is a highly vascularized, infiltrative, and invariably fatal
50 disease[7]. In GBM patients, Avastin alone or in combination with chemotherapy, alleviates cancer-
51 related symptoms, elicits a radiological response, and improves progression-free survival[7,8].
52 However, a transient response combined with the invasiveness of glioma cells and their co-option
53 of existing vasculature has dampened the clinical utility of Avastin in GBM[7]. At the same time,
54 angiogenesis inhibition can instigate significant tumor-intrinsic and -extrinsic metabolic
55 adaptations to sustain tumor growth, prompting speculation of targetable induced
56 vulnerabilities[9,10].

57 Preclinical studies have demonstrated that metabolic rewiring by the tumors is a proximal
58 consequence of angiogenesis inhibition[3,5,11]. In support, clinical magnetic resonance imaging
59 (MRI) studies show reduced tumor perfusion[12–14] and subsequent induction of intratumoral
60 hypoxia in response to anti-angiogenic treatments[2,13,15–17]. One prominent response to
61 angiogenesis inhibition-induced oxygen deficiency is HIF-1α stabilization, which can trigger a
62 cascade of metabolic adaptations to facilitate tumor growth and metastasis in an oxygen- and
63 nutrient-deficient microenvironment[18,19]. The elucidation of such adaptive mechanisms could
64 reveal cancer-specific vulnerabilities that may inform more effective combination therapies.

65 Glucose and glutamine are among the most critical nutrients that tumors derive from
66 blood[20]. Tumors consume glucose voraciously to generate biosynthetic precursors necessary for
67 proliferation via glycolysis; this includes ribose (glucose-6-phosphate—pentose phosphate
68 pathway), purines (3-phosphoglycerate—one carbon metabolism), and lipid head groups
69 (dihyroxyacetone-phosphate—glycerol)[20,21]. While pyruvate, the end-product of glycolysis, is
70 mostly secreted as lactate to enable NAD+ regeneration and maintain glycolytic flux, a significant
71 portion of glucose-derived pyruvate also enters the tricarboxylic acid (TCA) cycle[20,21]. Glutamine
72 also converges on the TCA cycle and serves as a carbon and nitrogen donor for nucleotide
73 synthesis and transamination reactions and is essential for glutathione generation[20,22]. Continued
74 proliferation of cancer cells is contingent upon continuous replenishment of TCA cycle carbon
75 atoms (anaplerosis) that are drained for macromolecule biosynthesis (cataplerosis)[23]. Depletion
76 of TCA cycle intermediates is characteristic of Avastin-treated tumors, which suggests that
77 angiogenesis inhibition induces anaplerotic nutrient stress[24].
78 To better understand how angiogenesis inhibition influences tumor metabolism and might
79 inform on effective combination therapies, we characterized the metabolomic and transcriptomic
80 profile of intracranial orthotopic gliomas on Avastin treatment. Angiogenesis inhibition led to a
81 marked reduction in TCA-cycle metabolites, indicative of anaplerotic nutrient stress. Indeed, we
82 demonstrate robust anti-tumor synergy and profound nutrient stress with combined Avastin and
83 glycolysis/OxPhos inhibitor treatment. Our findings indicate that disruptions to energy
84 metabolism in tumors treated with angiogenesis inhibitors constitute an "induced vulnerability"
85 that invite a systematic study of how such vulnerabilities might be exploited to potentiate the
86 efficacy of angiogenesis inhibition.
87

88 **RESULTS**

89 **Angiogenesis inhibition enhances hypoxia and anaplerotic nutrient stress in**
90 **intracranial tumors.** We implanted intracranial *ENO1*-deleted GBM xenografts into *Foxn1*$^{nu/nu}$
91 nude mice and administered the anti-human VEGFA antibody Avastin – which neutralizes
92 (human) glioma cell-secreted human VEGFA but does not neutralize endogenous mouse VEGFA
93 (**Supplementary Figure 1 a)**. After one week, we assessed the effect of the treatment on tumor
94 growth with T1-weighted MRI with and without the non-permeable contrast enhancement agent
95 gadobutrol (Gadavist ®) and T2-weighted MRI (**Figure 1a**). Untreated intracranial tumors
96 exhibited edema, which was visible as a hyperintense region on T2-weighted MRI and on
97 contrast-enhanced T1-weighted MRI (**Figure 1a**). In contrast, Avastin-treated tumors showed
98 attenuated contrast enhancement, indicating restoration of mature tumor vasculature (normalized)
99 and re-sealing of the BBB (**Figure 1a**) in a manner consistent with human tumor studies[25–30].
100 Thus, our findings confirm that intracranial D423 *ENO1*-deleted tumor xenografts have a
101 breached BBB that can be resealed with angiogenesis inhibitor treatment.

102 While vascular normalization improves perfusion, multiple studies have documented
103 elevated tumor hypoxia as a proximal consequence of angiogenesis inhibition[25](**Supplementary**
104 **Figure 2a-b)**. Specifically, the hypoxia imaging PET tracer ^{18}F-fluoromisonidazole (FMISO)
105 shows increased retention following Avastin treatment[31]. Consistent with these clinical
106 observations, post-mortem histopathological analyses of Avastin-treated gliomas revealed a
107 substantial increase in hypoxic areas, as evidenced by elevated CA9 expression (**Figure 1b-c**) as
108 well as impaired tumor growth but no regressions (**Figure 1d-f**). These observations prompted us
109 to consider that angiogenesis inhibition may also reduce access to blood-borne nutrients needed
110 to meet the anabolic demands of rapidly proliferating cancer cells (**Supplementary Figure 1c-e**).
111 To directly test this notion, we conducted an unbiased metabolomics analysis of intracranial
112 tumors treated with Avastin, which revealed a substantial reduction in the levels of TCA cycle

113 intermediates, including oxaloacetate, citrate, and fumarate (**Figure 1g**). Together, these results
114 indicate that Avastin treatment spurs metabolic stress in intracranial tumors.

115 **Re-sealing of the blood-brain barrier does not abrogate glycolysis inhibition nor the**
116 **anti-neoplastic effect of the phosphonate enolase inhibitor HEX.** We previously reported the
117 anti-neoplastic efficacy of a phosphonate inhibitor of enolase ("HEX") in an intracranial
118 orthotopic murine model of GBM[32]. As resealing the BBB is a hallmark of tumors treated with
119 angiogenesis inhibitors[25–30] and HEX shows poor BBB penetration[33], we employed T2-weighted
120 MRI to assess tumor growth of Avastin and HEX treatments, alone and in combination (**Figure**
121 **2a**). Treatment with Avastin or HEX slowed the growth of *ENO1*-deleted gliomas and was not
122 associated with frank tumor regression (**Figure 2a-d**); whereas combined treatment resulted in
123 profound tumor regression (**Figure 2a-d**) and increased survival: 67 days for combined therapy
124 compared with 42 days for HEX, 48 days for Avastin (median: 48 days), and 31 days for vehicle
125 control (**Figure 2e**), without any adverse effects (**Supplementary Figure 3a-d**) . Consistent with
126 therapeutic synergy, tumors showed markedly decreased proliferation (phosphor-histone H3) and
127 increased apoptosis (cleaved caspase 3) relative to monotherapy and control tumors (**Figure 2f-**
128 **h)**.

129 To determine whether the accentuated anti-tumor activity of the combination of Avastin
130 with HEX could be explained by enhanced glycolysis inhibition, we performed unbiased
131 comprehensive metabolomic profiling of the single and combination treated intracranial tumors.
132 Inhibition of glycolysis, evidenced by accumulation of glycolytic intermediates upstream of
133 enolase reaction, was specifically observed only in tumors of mice treated with either HEX as a
134 monotherapy or in combination with Avastin (**Supplementary Figure 3a**). The extent of
135 disruption of glycolysis was comparable between tumors treated with either HEX as a
136 monotherapy or in combination with Avastin (**Supplementary Figure 3a**).

137 Avastin only neutralizes human VEGFA secreted by human malignant xenografted cancer
138 cells and does not bind to endogenous mouse Vegfa[34]. Murine stroma-secreted Vegfs could
139 continue to promote neovascularization despite Avastin treatment, prompting us to pursue an
140 orthogonal approach with Tivozanib, which is effective against both mouse and human
141 VEGFR1/2/3[35], either as a single agent or in combination with HEX (**Supplemental Figure 1b**
142 **and 5a-e**). Tivozanib monotherapy yielded modest stasis of tumor growth, while combination
143 therapy with HEX yielded significant regression of intracranial tumors, including complete tumor
144 eradication (**Figure 2a-d and Supplemental Figure 5a-d**) and prolonged survival (63 days)
145 (**Supplemental Figure 5e**). Notably, the combination of Avastin or Tivozanib with HEX was
146 well-tolerated, as evidenced by no significant changes in body weight change before and after
147 treatment initiation (**Supplemental Figure 3a,c,e,f**).

148 **Disruption of TCA cycle anaplerosis, but not enhanced hypoxia, drives the synergy**
149 **between Avastin and HEX.** Hypoxia induction is one of the proximal consequences of
150 angiogenesis inhibition in the intracranial tumors (**Figure 1b-c**). Limited oxygen is known to
151 constrain the amount of ATP produced by oxidative phosphorylation (OxPhos), forcing cancer
152 cells to become increasingly reliant on anaerobic glycolysis to generate ATP[18,19]. Therefore, we
153 reasoned that such metabolic drift to glycolysis could further sensitize *ENO1*-deleted tumors to
154 glycolysis inhibition. *ENO1*-deleted tumor spheres *in vitro* were dramatically more sensitive to
155 POMHEX (a cell-permeable prodrug of HEX) under hypoxic conditions (1% O_2), as evidenced
156 by a dose-dependent decrease in the TMRE signal, compared to normoxic conditions (21% O_2)
157 (**Supplementary Figure 6a-d**). Notably, the potency of POMHEX under hypoxia was not limited
158 to *ENO1*-deleted cells as even *ENO1*-intact cells, which are relatively resistant to POMHEX under
159 normoxia, were significantly sensitized to POMHEX under hypoxic conditions (**Supplementary**

160 **Figure 6a-d**). These findings suggest that hypoxia dramatically enhances the anti-neoplastic
161 efficacy of enolase inhibition by promoting reliance on glycolysis.

162 Tumor hypoxia is a complex process determined by both demand (consumption) and
163 supply (vascular perfusion) of oxygen to the cells (**Figure 3a**)[36]. Two accurate determinants of
164 tumor hypoxia are: first, oxygen availability (perfusion hypoxia) and second, the rate at which the
165 tumor consumes oxygen in the mitochondria (consumptive hypoxia)[36]. Perfusion hypoxia is
166 dictated by blood perfusion to tumors. Consumptive hypoxia is determined by availability of
167 respiratory substrates such as pyruvate **(Figure 3a**).

168 Because HEX inhibits pyruvate production, we first examined the effect of enolase
169 inhibition on hypoxia *in vitro* (**Figure 3b**). Treatment with HEX significantly decreases hypoxia
170 *in vitro* under normoxia and hypoxia, as evidenced by a decrease in the expression of HIF1α and
171 carbonic anhydrase 9 (CA9) and a concomitant increase in mitochondrial OxPhos marker CPT1A
172 (**Figure 3c, Supplemental Figure 7a**). One explanation could be that diminished production of
173 glucose-derived pyruvate, a key substrate for mitochondrial oxidative phosphorylation, results in
174 a decrease in consumptive hypoxia[37] (**Figure 3b**). To further understand the mechanism of
175 synergy of combined angiogenesis and glycolysis inhibition, we performed unbiased
176 transcriptomic analysis on intracranial tumor xenografts treated with HEX and Avastin as mono-
177 or combination therapies. We identified the top 40 genes from the TCGA GBM transcriptomic
178 studies that positively correlated with CA9, a well-known hypoxia marker (Spearman
179 coefficient >0.5; **Figure 3d**). Consistent with our *in vitro* findings, the hypoxia transcriptomic
180 signature is significantly elevated in Avastin-treated intracranial tumors compared to other
181 treatment groups (**Figure 3d-g**). Interestingly, the combination of Avastin and HEX did not
182 significantly alter hypoxia signature (**Figure 3d-g**). This could be explained by a decrease in
183 consumptive hypoxia (mitochondrial oxygen consumption) from enolase inhibition, which

184 negates Avastin-induced perfusion hypoxia (**Figure 3a**). Our *in vitro* observations were
185 corroborated by transcriptomic analysis of hypoxia markers CA9 and VEGFA in intracranial
186 tumor lysates (**Figure 3h-j**) and fixed brain tumor sections (**Figure 3k-l**). Immunoblots on tumor
187 lysates showed an increased CA9 expression in Avastin-treated tumors, a near complete
188 elimination of CA9 expression for HEX-treated tumors, and overall diminished CA9 expression
189 on tumors treated with Avastin and HEX (**Figure 3h-i**). Similarly, immunohistochemistry on
190 fixed intracranial tumors from the Avastin treatment group showed an overall increase in CA9
191 staining (**Figure 3k-l**). In contrast, tumors from either HEX monotherapy or Avastin + HEX
192 combination therapy produced considerably diminished CA9 expression compared to control or
193 Avastin monotherapy groups (**Figure 3k-l**). Our data reinforce the influence of 'consumptive'
194 hypoxia on overall tumor hypoxia and show that 'perfusion' hypoxia does not drive the synergy
195 between Avastin and HEX in intracranial tumors in vivo.

196 Another explanation for the synergy between Avastin and HEX could be the restriction of
197 blood-borne nutrients to tumors caused by angiogenesis inhibition, thereby creating a nutrient-
198 deficient tumor microenvironment **(Supplementary Figure 2c-e**). We previously showed that
199 lower levels of carbon precursors in the medium translate to markedly higher sensitivity to
200 inhibition of glycolysis[37]. Specifically, glycolysis inhibition by (POM)HEX together with low
201 nutrient availability in culture medium, strongly abrogated anabolic reactions crucial for tumor
202 growth[37]. Treatment with Avastin models a nutrient starved tumor microenvironment in vivo
203 (**Figure 1g**). We reasoned that the combination of HEX and Avastin could exacerbate anaplerotic
204 nutrient stress in tumors. As expected, whereas treatment with Avastin or HEX alone modestly
205 depleted TCA cycle intermediates, combined treatment exacerbated this effect (**Figure 5a**). We
206 also found that combined treatment yielded broadly diminished levels of amino acids, including
207 those derived from transamination of TCA cycle intermediates (**Figure 5b**).

208 Unbiased transcriptomic analysis of the tumors treated with monotherapy of Avastin or HEX,
209 or combination of Avastin and HEX, revealed notable transcriptomic changes. Using DESeq2
210 analysis, we observed minor changes in differentially up- or down-regulated genes in HEX or
211 Avastin monotherapy groups. In contrast, the combination treatment produced significantly
212 greater changes in differentially expressed genes (DEGs; up: log2Fc ≥ ; down: log2Fc ≤ -1; padj
213 ≤ 0.05), indicative of a synergistic effect of the drugs on tumor transcriptome (**Figure 4c-f**). For
214 the combination treatment group, genes that overlapped with monotherapy groups also displayed
215 a greater fold change, which supports a synergistic effect of the combination treatment observable
216 at the transcriptomic level (**Figure 4c-f, Supplementary Figure 8a-c**). Gene set enrichment
217 analysis (GSEA) further revealed multiple pathways that are enriched in different treatment
218 groups (**Figure 4g-m**). Treatment with HEX monotherapy or combination of Avastin + HEX
219 enriched pathways involved in cellular response to nutrient deficiency—an effect that was
220 exacerbated in combination treatment compared to HEX alone (**Figure 4i, m and**
221 **Supplementary Figure 9a-b**) which corroborates the metabolomic data (**Figure 4a-b**). GSEA
222 showed statistically significant (q<0.05, NES<-2), negative enrichment of pathways unique to
223 combined treatment, such as those relevant to mitosis, DNA replication, and DNA repair (**Figure**
224 **4m**). These observations provide mechanistic support that combined treatment with Avastin and
225 HEX exaggerate anaplerotic nutrient stress and abrogate the anabolic reactions critical for cancer
226 cell proliferation and lead to activation of nutrient stress adaptation response (**Figure 4 and**
227 **Supplementary Figure 9**).

228 **Angiogenesis inhibition generates broad metabolic vulnerabilities beyond glycolysis.**
229 Given the dramatic synergy between Avastin and HEX in *ENO1*-deleted intracranial tumors, we
230 sought to determine whether other metabolism-targeting therapies would also display similar
231 synergy. Similar to enolase inhibition, inhibition of mitochondrial OxPhos is also marked by
232 depletion of TCA cycle metabolites and most prominently, the amino acid aspartate [38]. We tested

233 the effects of IACS-010759, an inhibitor of mitochondrial complex 1, on *ENO1*-deleted cells[38]
234 (**Figure 5**). Previous studies have shown that treatment with IACS-010759 significantly decreases
235 TCA cycle intermediates[38] (**Figure 5a-f**). Interestingly, toxicity of IACS-010759 in *ENO1*-
236 deleted cells depended on whether cells were cultured in nutrient-rich or nutrient-deplete
237 conditions. Cells grown in nutrient-rich medium treated with IACS-010759 had minimally
238 impacted survival and energy homeostasis, as evidenced by phosphocreatine levels comparable
239 to controls (**Supplemental Figure 10a-d)**. However, cells grown in medium with low anaplerotic
240 content were significantly more sensitive to IACS-010759, as evidenced by a significant reduction
241 in phosphocreatine levels—demonstrating exacerbated bioenergetic collapse (**Supplemental**
242 **Figure 10a-d**). These in vitro observations suggested that in vivo tumors growing in a nutrient-
243 deficient environment induced by angiogenesis inhibition could also be predisposed to
244 sensitization by IACS-010759.

245 *ENO1*-deleted intracranial tumors were treated with either IACS-010759 or Avastin as
246 monotherapies or in combination for 28 days. While treatment with IACS-010759 alone
247 minimally impacted tumor growth in vivo, combined treatment with IACS-010759 and Avastin
248 dramatically delayed tumor growth and produced frank regression of some tumors. (**Figure 5g-**
249 **j)**. These data suggest that angiogenesis inhibition exacerbates metabolic stress and potentiates
250 the anti-neoplastic effect of metabolic inhibitors such as IACS-010759. Additionally, our
251 preliminary experiments also show that that the angiogenesis inhibitor Tivozanib also synergizes
252 with IACS-010759 in xenografts of the NB1 (*PGD*-homozygously deleted) cell line with
253 complete regression observed at doses of IACS-010759 that are ineffective as a monotherapy
254 (**Supplementary Figure 11A-B**).

255 **Combined inhibition of angiogenesis and metabolism is synergistic against non-**
256 **glycolysis-compromised orthotopic tumors.** We investigated whether inherent compromise of
257 glycolysis was required for Avastin and metabolic inhibitors to exert a synergistic anti-neoplastic

258 effect. Accordingly, we compared the efficacy of Avastin and HEX as single agents or in
259 combination in mice bearing *ENO1*-wildtype (U87) intracranial tumors with the same dosing
260 regimen as we had applied for those with *ENO1*-deleted (D423) tumors (225 mpk BID) for two
261 weeks (**Figure 2**). *ENO1*-deleted tumors showed moderate sensitivity to HEX or Avastin as single
262 agents, and the combined treatment yielded synergistic regression of tumors even with two weeks
263 of treatment (**Figure 6a-d**). However, in *ENO1*-wildtype tumors, with the same treatment regimen
264 and duration, Avastin and HEX as single agents only minimally delayed growth, while combined
265 treatment exerted an enhanced, and possibly additive anti-tumor activity (**Figure 6e-i**). The degree
266 of growth inhibition achieved in *ENO1*-wildtype tumors was dependent on the dose of HEX
267 (**Supplemental Figure 12**). In a separate dose escalation study where HEX was administered 200
268 mpk three times a day for 8 days, we observed a modest improvement in the efficacy of HEX as
269 a single agent against *ENO1* WT tumors (**Supplemental Figure 12a-c**). Interestingly, the
270 combination of high-dose HEX and Avastin significantly suppressed the growth of *ENO1* WT
271 intracranial tumors with 8 days of treatment (**Supplemental Figure 12a-c**). Histopathological
272 analyses also showed modest decrease in phospho-histone H3 and increase in cleaved caspase-3
273 signals (**Supplemental Figure 12d-e**).

274 We also tested if the same rationale could be extended to the treatment of *ENO1*-wildtype
275 U87 intracranial tumors with other metabolic inhibitors. Treatment with Avastin sensitized
276 intracranial tumors to IACS-010759, resulting in a significant inhibition of tumor growth, but
277 without frank tumor regression (**Supplemental Figure 13**). Together, these findings indicate that
278 angiogenesis and metabolic inhibitors can work synergistically to inhibit the growth of both
279 glycolysis-compromised tumors and non-glycolysis-compromised tumors, raising the possibility
280 of broad clinical applicability.

281 **Sensitivity to Avastin is associated with low expression signatures of mitochondrial**
282 **metabolism and the TCA cycle.** Xenografted tumors from different cell lines differ significantly

283 in their response to Avastin and other angiogenesis inhibitors. In the context of this study, we
284 sought to understand the broad molecular features underpinning response to angiogenesis
285 inhibitors—specifically, whether anaplerotic nutrient stress or diminished mitochondrial
286 metabolism is a determinant of sensitivity to Avastin in human tumors. To that end, we
287 interrogated a set of PDX models from CrownBio that had corresponding transcriptomics and
288 data on anti-tumor response to Avastin (**Supplemental Figure 14**); transcriptomic analyses were
289 performed on tumors prior to Avastin treatment initiation. We searched for specific transcriptomic
290 characteristics that correlated with anti-tumor responsiveness across a range of independent
291 PDXs. Our analysis revealed a strong negative correlation between Avastin sensitivity and
292 mitochondrial metabolic gene signature in tumors at baseline (**Supplemental Figure 14-c**). More
293 specifically, tumors possessing elevated gene signature for mitochondrial metabolic processes,
294 such as mitochondrial complex I biogenesis, ATP biosynthesis, TCA cycle and mitochondrial
295 respiratory chain reactions, better tolerated Avastin treatment relative to PDXs with lower
296 mitochondrial metabolic gene signature (**Supplemental Figure 14b-c**). We also found that
297 tumors with enrichment in gene signatures that bolster response to nutrient deficiency at baseline,
298 were less sensitive to Avastin reinforcing the notion that nutrient stress adaptation may predict
299 Avastin sensitivity (**Supplemental Figure 14b**). These PDX findings complement our key
300 observation that anaplerotic nutrient stress achieved by treatment with either glycolysis inhibitor
301 HEX or mitochondrial OxPhos inhibitor IACS-010759 sensitizes tumors to angiogenesis
302 inhibition.

303 **DISCUSSION**

304 Here, we sought to uncover potential angiogenesis-inhibition induced metabolic
305 vulnerabilities. Comprehensive metabolomic and transcriptomic analysis of intracranial tumor
306 xenografts revealed that anti-angiogenic therapy generates an anaplerotic nutrient deficit and
307 sensitizes xenografted tumors to inhibitors of key energy metabolism pathways, such as glycolysis

308 and oxidative phosphorylation. Combined treatment of the angiogenesis inhibitor Avastin and the
309 glycolysis inhibitor HEX yielded synergistic anti-tumor effects accompanied by dramatically
310 exacerbating metabolomic and transcriptomic signatures of anaplerotic nutrient stress in
311 intracranial tumors.

312 The blood-brain-barrier is poorly permeable to small hydrophilic molecules such as HEX and
313 an initial explanation for its efficacy as a monotherapy would have posited permeation through
314 the tumor-associated leaky vasculature. The dramatic synergy between Avastin and HEX, despite
315 Avastin's effect on normalizing (sealing) the BBB, indicates that HEX must be reaching the
316 malignant glioma cells through another mechanism. Low molecular weight phosphonate drugs
317 are known to reach the brain through fenestrations in the blood-CSF barrier[32,39]. Unlike the BBB,
318 capillaries in the blood-CSF barrier have fenestrations, which allow low molecular weight,
319 hydrophilic drugs to permeate into the brain; one prominent example of such is the antibiotic
320 fosfomycin, which is used clinically to target brain abscesses (**Supplementary Figure 4b**)[39].
321 Given the high physiochemical similarity – it is most likely that HEX reaches brain and brain
322 tumor through permeation via the blood-CSF barrier and the Avastin-induced re-sealing of the
323 BBB is inconsequential for HEX entry (**Supplementary Figure 4b**). Furthermore it is worth
324 noting that the combination of HEX and angiogenesis inhibitors may yield superior results in
325 humans given that HEX has a an unusually short half-life in mice; with the drug being
326 undetectable in plasma in as little as 2 hours after injection[33]. This is in contrast to rat, dog and
327 non-human primate where the half-life of HEX is ~10-fold longer[33].

328 We also showed that Avastin treatment sensitizes *ENO1* deleted tumors to inhibition of
329 mitochondrial oxidative phosphorylation by IACS-010759. Previous studies reported that
330 homozygous deletion of *PGD* causes even stronger OxPhos inhibitor vulnerability[38,40].
331 Accordingly, we showed that angiogenesis inhibitor Tivozanib also synergizes with IACS-

332 010759 in xenografts of the NB1 (*PGD*-homozygously deleted) cell line with complete regression
333 observed at doses of IACS-010759 that are ineffective as monotherapy. Importantly, studies have
334 suggested a therapeutic benefit in combining Avastin with the mitochondrial complex I inhibitor,
335 metformin for the treatment of recurrent type I endometrial cancer, ovarian cancer, and non-small
336 cell lung cancer[41–43]. Our findings are consistent with this line of reasoning and provide a
337 mechanistic basis for the efficacy of the combination treatment modality. Finally, combined
338 treatment with Avastin and HEX/IACS-010759 also showed therapeutic benefit against
339 glycolysis intact wild-type tumors, raising the possibility of therapeutic relevance across a broad
340 range of malignancies. With respect to clinical application, it is worth noting that we can achieve
341 significant regression of tumors at doses of IACS-010759 which are far lower than those
342 employed in published literature[38]. This is important since inhibition of mitochondrial OxPhos
343 yielded grade 3 peripheral neuropathy in recent phase 1 trials: 11/23 patients in the solid tumor
344 trial and 4/11 patients in the relapsed/refractory acute myeloid leukemia trial (NCT02882321,
345 NCT03291938)[44]. A dose-reduction of IACS-010759 enabled by combination with angiogenesis
346 inhibitors may allow resuscitation of this drug given its very sharp dose-limited toxicity[44].
347 To definitively correlate our pre-clinical findings with human clinical data, it would be
348 highly desirable to perform a thorough metabolomic profiling of primary human tumors subjected
349 to angiogenesis inhibitors. However, due to hemorrhagic complications and challenges associated
350 with wound healing, anti-angiogenic therapies preclude surgical resection of tumors (treatment
351 discontinuation required for at least 28 days before surgery)[1], which restricts a systematic
352 assessment of metabolic alterations caused by angiogenesis inhibition in human tumors. This may
353 also explain why, despite the widespread use of angiogenesis inhibitors in the clinic, limited
354 investigations have been performed to understand how these drugs affect the transcriptomic or
355 metabolic landscape of human tumors. We circumvented this key limitation by employing human
356 cell line-derived xenograft (CDX) as well as patient-derived xenografts (PDX). Using different -

357 omic profiling approaches, we identified crucial, exploitable vulnerabilities associated with
358 angiogenesis inhibition. Overall, our data strongly suggests that anaplerotic nutrient stress
359 incurred by tumors due to angiogenesis inhibition enhances sensitivity to therapies targeting
360 tumor metabolism.

361 In conclusion, our findings reinforce clinical evidence showing that Avastin, despite
362 significantly reducing blood flow to the tumors, only temporarily halts tumor growth. However,
363 essential metabolic adaptations that arise in the context of angiogenesis inhibition can be
364 leveraged to sensitize tumors to different metabolism-targeting therapies. Our preclinical data
365 strongly invite a systematic investigation of combinations of angiogenesis inhibitors with
366 therapies targeting cancer-specific metabolic vulnerabilities beyond HEX and IACS-010759. For
367 instance, therapeutic agents that target pathways converging on anaplerosis, such as
368 glutaminolysis inhibitors (glutaminase inhibitor CB-839, the ASCT2 inhibitor V-9302[45]), or other
369 anabolic and catabolic pathways involving the metabolism of asparagine, (L-arsparaginase[46])
370 methionine (MAT2A inhibitor AG-270, PRMT5 inhibitor GSK3326595[47] and arginine (ADI-
371 PEG20[48,49]) (**Figure 7**). An additional mechanism worth investigating may be interactions with
372 metabolic therapies involving caloric restriction or specific macronutrient intake, such as
373 ketogenic diets which restrict carbohydrates, which may further enhance the therapeutic efficacy
374 of anti-angiogenic therapies. Our paper thus demonstrates the mechanistic basis for combining
375 anti-metabolic and anti-angiogenesis therapies to potentiate anti-tumor efficacy and potentially
376 improve overall patient survival.

377 **METHODS**

378 **Cell Lines**

379 The H423/D423-MG (CVCL_1160, glioblastoma) cell line, which has a 1p36
380 homozygous deletion spanning *ENO1*, was generously provided by D. Bigner[50]. D423 *ENO1*, an
381 isogenic cell line with ectopic constitutive expression of *ENO1*, was generated by our lab as

382 described previously. The *ENO1*-WT cell lines LN319 (CVCL_3958, a **sub-clone** of LN-992)
383 and U87 (CVCL_0022) were obtained from the Department of Genomic Medicine/IACS Cell
384 Bank at MD Anderson.

385 All cells were used below passage 25 and maintained in DMEM (pH 7.4) supplemented
386 with 4.5 g/L glucose, 110 mg/L pyruvate, and 584 mg/L glutamine (Cellgro/Corning #10-013-
387 CV) at 37°C in a 5% CO2 atmosphere unless indicated otherwise. DMEM was supplemented to
388 achieve a composition of 10% fetal bovine serum (Gibco/Life Technologies #16140-071), 1%
389 PenStrep (Gibco/Life Technologies #15140-122), and 0.1% amphotericin B (Gibco/Life
390 Technologies #15290-018). Cell lines were regularly checked for mycoplasma contamination
391 with the MycoAlert PLUS detection kit (Lonza) and authenticated by STR fingerprinting with the
392 Promega PowerPlex 16 System. STR fingerprinting was conducted by personnel in MD
393 Anderson's Characterized Cell Line Core (CLCC). STR profiles were compared to both the
394 CLCC database and external cell databases (DSMZ/ATCC/RIKEN/JCRB).

395 **Intracranial orthotopic tumor cell implantation**

396 All experiments involving mice were performed at MD Anderson under a protocol approved by
397 MD Anderson's Institutional Animal Care and Use Committee (IACUC).

398 Intracranial glioma tumors were generated by injecting 200,000 cells into the brains of 4- to 6-
399 month-old immunocompromised female nude Foxn1nu/nu mice, which were bred at MD
400 Anderson's Experimental Radiation Oncology Breeding Core. Prior to intracranial tumor cell
401 injection, a bolt (a plastic screw with a hole in its center) was drilled into the skull of each animal.
402 The animals were allowed to recover for 2 weeks, during which time they were monitored for
403 signs of morbidity. Two weeks after bolt implantation, the cells were injected through the bolt
404 using a Hamilton syringe. Animals exhibiting any severe neurological morbidities were after
405 tumor implantations were euthanized. Intracranial bolting and injections were performed by

406 personnel in MD Anderson's Intracranial Injection Fee-for-Service Core[51]. All procedures were
407 performed in accordance with the regulations of MD Anderson's IACUC.

408 **Tumor volume measurement in vivo**

409 Mice bearing intracranial tumors underwent T2-weighted MRI weekly on a 7T Biospec
410 USR707/30 scanner (Bruker Biospin MRI, Billerica, MA) in MD Anderson's Small Animal
411 Imaging Facility. Prior to imaging, the animals were briefly anesthetized with isoflurane.
412 Throughout the imaging procedure, the animals' body temperatures were maintained with a
413 heating blanket; their bodies and heads were restrained with a stereotactic holder; and their heart
414 and breathing rates were monitored.

415 For T2-weighted MRI, a low-resolution axial scan was first taken to calibrate the scanner
416 position. Then, two high-resolution axial scans and one high-resolution coronal scan were taken.
417 For the axial scans, the slice thickness was 0.500 mm, and the increment between each slice was
418 1.000 mm. To obtain better tumor coverage, we offset the two axial scans by 0.500 mm, which
419 was equal to the difference between the slice increment and slice thickness. The coronal scans
420 had a slice thickness of 0.750 mm and a slice increment of 1.000 mm. The total number of slices
421 for each scan was based on the size of the tumor. The MRI scans were analyzed with the open-
422 source image-processing software program 3D Slicer (v4.10, http://www.slicer.org)[52].

423 MRI series were independently reviewed, and tumor volumes determined in 3D Slicer, by
424 three lab members. The draw tool in the editor module of 3D Slicer was used to manually delineate
425 tumor tissues slice-by-slice. Enhanced contrast due to edema, as well as hollow areas of tumor
426 caused by bolting, were excluded. The tumor volume of each scan was calculated automatically
427 by using the Label Statistics module, which calculates the tumor volume for a scan by converting
428 the selected pixel area on each slice to squared centimeters, multiplying that value by the slice
429 increment, and then summing up the slice volumes. The tumor volume for each mouse was

430 calculated as the average of the three scans (2 sets of axial scans and one set of coronal scans).
431 Finally, all three independent measurements were averaged.

432 **Polar metabolite profiling**

433 The mice were euthanized following the standard IACUC protocol. The animals were then
434 dissected to extract subcutaneous tumors. The weights of the tumors were recorded, and the
435 tumors were cut into two pieces, one of which was snap-frozen in liquid nitrogen for metabolomic
436 analysis. The tumor pieces snap-frozen in liquid nitrogen were cut into small pieces (~50 mg) and
437 placed into pre-cooled microcentrifuge tubes (Fisher Scientific, cat. 02-681-291) containing steel
438 beads (Qiagen). To these tubes, we added 1 mL of 80% methanol pre-cooled to -80 °C. Tumor
439 tissue was bead-mill homogenized with the Qiagen TissueLyser by shaking tubes at 28 Hz for
440 multiple rounds of 45 s each. To the tubes of the homogenized tumor lysates, we added 80%
441 methanol to create a final weight-adjusted volume of 25 mg/ml. After incubation for 15 min on
442 dry ice, tumor lysates were homogenized once more using a vortex mixer for 1 min. The samples
443 were then centrifuged for 5 min at 14,000 x g at 4 °C. Cell debris and non-polar metabolites
444 precipitated and were separated from the polar metabolites, which collected in the supernatant.
445 The polar metabolites were transferred into chilled 1.5-ml Eppendorf tubes and dried in a
446 SpeedVac (Thermo Fisher). The dried and concentrated polar metabolites were submitted to John
447 Asara's Polar Metabolite Profiling Platform at Beth Israel Deaconess Medical Center. There, the
448 samples were subjected to tandem mass spectrometry via selected reaction monitoring with
449 polarity switching for 300 total polar metabolite targets using a 5500 QTRAP hybrid triple
450 quadrupole mass spectrometer (SCIEX). The mass spectrometer was coupled to a high-
451 performance liquid chromatography system (Shimadzu) with an amide hydrophilic interaction
452 liquid chromatography column (Waters) run at pH=9.0 at 400 mL/min. Q3 peak areas were
453 integrated using MultiQuant 2.1 software[32].

454 **Immunohistochemistry**

455 Tumor-bearing mice were euthanized at the end of the experiment or earlier if they exhibited
456 neurological symptoms, and their brains were harvested and then fixed in 10% paraformaldehyde.
457 Mouse brains were dissected and submitted to MD Anderson's Veterinary Pathology Core for
458 dehydration, paraffin embedding, and tissue sectioning. Tissue sections were dried overnight at
459 60 °C and then deparaffinized in xylene. The deparaffinized sections were rehydrated by a series
460 of washes in aqueous solutions of decreasing ethanol concentration. Antigens were retrieved by
461 boiling the sections in citrate buffer (1:100 Vector Antigen Unmasking Solution [Citrate-Based]
462 H-3300 250 mL) for 10 min and then cooling the sections for 30 min. Tissue sections were
463 blocked with 2% goat serum (Vector S-1000 Normal Goat Serum; 20 mL) in PBS (Quality
464 Biological PBS [10X], pH 7.4; 1000 mL) for 1 h. The sections were then incubated with
465 monoclonal anti-cleaved caspase 3 rabbit (cleaved caspase-3 (Asp175) (5A1E) rabbit mAb; CST#
466 9664T, Cell Signaling Technology) or anti-phospho S10 histone H3 (rabbit anti-phospho histone
467 H3 [S10] IHC antibody, affinity purified; Bethyl Laboratories, IHC-00061 or rabbit anti-carbonic
468 anhydrase 9 antibody (CST#5649)) diluted to 1:1000 with 2% goat serum in PBS overnight at
469 4°C. The next day, the sections were washed three times with PBS in a shaker. After washing
470 with PBS, the sections were incubated with 1X goat anti-rabbit IgG poly HRP secondary antibody
471 (Invitrogen by Thermo Scientific) for 30 min and then washed in PBS and Tween 20 (Fisher
472 BioReagents BP337-500). The sections were stained with either ImpactNOVAred (Vector Labs
473 SK-4805) or EnzMet^{tm} (Nanoprobes #6001-30 mL) and then counterstained with hematoxylin or
474 with hematoxylin and eosin, respectively. The stained sections were mounted using Denville Ultra
475 Microscope Cover Glass (#M1100-02) and Thermo Scientific Cytoseal 60 and dried overnight at
476 room temperature.

477 **RNA sequencing, and data analysis from treated xenografted tumors**

478 Tumors were extracted from frozen brain sections from mice treated with vehicle, Avastin, HEX
479 or Avastin + HEX for 14 days. Briefly, whole brain was dissected out from the mice following

480 euthanasia and immediately snap frozen in liquid nitrogen. Xenografted tumors from frozen
481 whole brain was carefully cut out as 2 mm wide cross-sectional slices. Axial MRI scans were
482 used as guide to cut xenografted tumor from the whole brain. For RNA extraction from the
483 tumors, approximately 1ml of Trizol reagent was added to 5 mg of frozen xenografted tumors
484 and homogenized using a homogenizer (POLYTRON® PT 1200E, Kinematica #9112212) 200
485 µl chloroform was added to the homogenized tumors in Trizol, and after a vigorous shaking of
486 the tubes, phase separation was performed by centrifugation. Aqueous phase solution was
487 precipitated with isopropanol, and RNA purification was performed using the Qiagen RNA
488 extraction kit (steps 4-8). Approximately, 200 ng of RNA was submitted to BGI to perform 100
489 bp paired end for 30 million transcript reads. The FASTQ files obtained from BGI were aligned
490 with hg19 to generate sam files using the HISAT/StringTie/Ballgown modules[53]. Differential
491 gene expression between the control and experimental groups were determined by using the
492 edgeR package v3.34.0, To identify significant differentially expressed genes, we used the
493 following criteria: $\log_2$ fold change ($\log_2$Fc) ≥ 1 (for the Up-regulated gene) or $\log_2$Fc ≤ -1 (for
494 the down-regulated gene), and an adjusted p-value (padj) ≤ 0.05. Reactome pathway enrichment
495 was determined using the gene set enrichment analysis (GSEA)[54] with default parameters and
496 Reactome subset (c2.cp.reactome.v2022.1.Hs.symbols.gmt from Human MSigDB
497 Collections)[55]. Heatmaps were generated using the ggplots or pheatmap package in R v4.0.3.

498 **Patient-derived xenograft (PDX) models (Crown Bio datasets)**

499 PDX models were developed and established in immunodeficient mice at Crown Bioscience as
500 previously described[56]. Briefly, cryopreserved or fresh tumor tissues were cut into small pieces
501 (~2-3 mm in diameter), and subcutaneously transplanted in the right flank of NOD/SCID or
502 BALB/c nude mice. Tumor growth was checked twice a week using a caliper. Pharmacological
503 dosing started when tumor size reached 100-300 mm^3. Tumor-bearing mice were euthanized
504 when tumor size reached 3000 mm^3. All procedures were performed in pathogen-free animal

505 facility at Crown Bioscience under the approved protocols by the Institutional Animal Care and
506 Use Committee.

507 **RNA-seq**

508 Library construction for RNA-seq was performed using MGIEasy RNA Library Prep Set (MGI,
509 catalog no. 1000006383) following the manufacturer's instructions. Briefly, poly-A mRNA was
510 captured from total RNA using Oligo-dT-attached magnetic beads (Agencourt, catalog no.
511 A63987) and fragmented. cDNA was synthesized and purified, followed by A-tailing and
512 ligation of adapters. DNA fragments with adapters were selected and amplified by PCR. The
513 quality of the final library was checked by Qubit and Agilent 2100 Bioanalyzer. Paired-end
514 sequencing with a read length of 150bp was performed following the manufacturer's
515 instructions (MGI, catalog no. 1000012555).

516 **Alignment and quantification of transcripts**

517 The quality of raw data was checked by FastQC (version 0.11.9). Adapter and low-quality
518 sequences were trimmed by Trimmomatic software (version 0.40)[57]. Sequencing reads were
519 mapped to human (hg19) reference genomes using STAR (version 2.7.10a)[58], based on which
520 alignment yielded fewer mismatches, they were subsequently sorted into human or mouse
521 groups, representing cancer or stromal transcriptomes, respectively. Ambiguous reads were
522 discarded. Transcript-level read counts were quantified using kallisto (version v0.46.1)[59]; and
523 subsequently summarized to gene-level count and abundance estimates. The count estimates
524 were used as inputs in differential expression analysis (see **Differential expression analysis on**
525 **CDX dataset**). The gene-level transcript abundance values (in transcripts per million, or TPM)
526 were used as inputs in biomarker discovery (see **Biomarker discovery in PDX dataset**).

527 **Differential expression analysis on CDX dataset**

528 Differential expression analysis was performed using DESeq2 (version 1.34.0)[60] cancer (human)
529 and stroma (mouse) genes. The following generalized linear model was fit to explain the

530 expression level of each gene with respect to treatment groups, accounting for possible

531 interaction between Avastin and HEX treatments:

532 $$\log(\mu_{ij}) = \beta_0 + \beta_1 \text{Avastin}_{ij} + \beta_2 \text{HEX}_{ij} + \beta_3 \text{Avastin}_{ij} \times \text{HEX}_{ij} + \log(s_j),$$

533 where read count for gene *i*, sample *j* is assumed to follow a negative binomial distribution with

534 fitted mean μ_{ij} and sample-specific size factor s_j. Regression coefficients β_1 and β_2 measure the

535 effects of Avastin and HEX treatments on gene expression, and β_3 measures how the effect of

536 Avastin treatment changes when HEX treatment is also present.

537 **Biomarker discovery in PDX dataset**

538 The Crown Bioscience PDX dataset consist of tumor volume records in 21 PDX models under

539 Avastin and negative control treatments, as well as the cancer transcriptomic profiles of these

540 PDX models. The 21 PDX models used in this study comprise following cancer types: breast (n

541 = 1), cervix (n = 4), cholangiocarcinoma (n = 2), colon (n = 7), kidney (n = 1), liver (n = 2),

542 lung (n = 2), and ovary (n = 2). The following linear mixed model was used to explain tumor

543 volume at day *t* for mouse *i* in PDX model *j*:

544 $$\log(TV_{tij}) = \beta_0 + \beta_1 \log(TV_{0ij}) + \beta_2 Day_t + \beta_3 Avastin_{ij} \times Day_t + \beta_4 Avastin_{ij} \times Gene_j \times Day_t + u_{0j} + u_{1j} \times Day_t + u_{(0i|j)} + u_{(1i|j)} \times Day_t + \varepsilon_{tij},$$

545 where *t*, *i*, *j* indicates time point, mouse, and PDX, respectively. 'Gene' is a covariate for gene-

546 level transcript abundance values in log scale. For a detailed description of the fixed and random

547 effect terms, please refer to Guo *et al*[56]. Using Benjamini-Hochberg adjusted p-value < 0.05 as

548 cut-off, we obtained a list of genes whose expression levels significantly impact the efficacy of

549 Avastin treatment ($\beta_4 \neq 0$). This gene list was used as input in gene set enrichment analysis.

550 **Gene set enrichment analysis**

551 Gene set enrichment analysis (GSEA)[54] performed using clusterProfiler (version 4.2.2)[61].The

552 input gene lists were ranked based on Q = sign(β)·log(p), where β and p are the regression

553 coefficient and its associated p-value obtained from the differential expression and biomarker

554 analyses described in previous sections. Gene Ontology and REACTOME gene sets were
555 retrieved using msigdbr (version 7.5.1).

556 **Western blots**

557 **Cells**

558 Cells were grown in 6 well plates and treated with POMHEX for 48 hours in hypoxic (5% O_2)
559 and normoxic conditions (21%). Whole cell lysates were harvested by washing the cells twice
560 with ice cold phosphate-buffered saline (PBS). RIPA buffer (ice-cold) was supplemented with
561 protease (cOmplete™ mini, Roche#11836153001) and phosphatase inhibitors (PhosSTOP,
562 Roche, #5892970001), added and the samples were then sonicated.

563 **Tumors**

564 Frozen intracranial tumors were cut into smaller pieces and approximately 20 mg of tumors was
565 used to prepare lysates. RIPA buffer supplemented with protease and phosphatase inhibitors was
566 added to the tumor samples and thoroughly homogenized. The tumor homogenates were further
567 sonicated and centrifuged.

568 The protein concentrations in cell/tumor lysates were determined using the BCA assay
569 (ThermoFisher, #23227). After being separated by Nu-PAGE SDS-PAGE (4-12% gradient)
570 (TransBlot turbo), proteins were deposited onto nitrocellulose membranes using the semi-dry
571 technique. The successful transfer of proteins onto the membrane was confirmed with Ponceau S
572 staining. To block the non-specific membrane sites, 5% non-fat dried milk in tris-buffered saline
573 (TBS) with 0.1% Tween 20 (TBST) was used as the blocking agent. The membranes were treated
574 with primary antibodies overnight at 40C with moderate rocking. The membranes were TBST-
575 washed three times for five minutes on the second day. After that, membranes were gently rocked
576 for an hour while incubating in HRP-tagged secondary antibody (1:5000). The antibodies used in
577 our investigations were: (HIF1-α (CST #14179), β-actin (CST#3806), CA9 (CST#5649),

578 Vinculin (CST#13901), Atg5 (CST#9980), LC3B(CST#3868), pAkt (CST#9271), Akt
579 (CST#9272), CPT1A (CST#12252), anti-rabbit HRP linked antibody (CST#7074), anti-mouse
580 HRP linked antibody (CST#70776)).

581 **Statistical analysis**

582 Statistical analyses reported in this study were performed using either Microsoft Excel or
583 Graph Pad Prism 8. Unpaired Student's test and 1- or 2-way ANOVA were used where
584 appropriate. Tukey's post hoc analysis was used to determine statistical significance following
585 ANOVA. $P<0.05$ was used as a threshold to determine statistical significance.

586 **Illustration**

587 All illustrations were made using BioRender.

588 **Competing Interests**

589 We declare no competing financial interests. F.L.M. is inventor on a patent covering the concept
590 of targeting ENO1-deleted tumors with inhibitors of ENO2 (US patent 9,452,182 B2) and
591 inventor on a patent application describing the synthesis and utility of novel pro-drug inhibitors
592 of enolase US 62/797,315 (Filed Jan 27, 2019). F.L.M. and Y-H.L. are inventors on a patent
593 application for the use of enolase inhibitors for the treatment of ENO1-deleted tumors (US patent
594 10,363,261 B2).

595 **Funding**

596 We appreciate all the generous financial support that enabled our investigation. Briefly: The Small
597 Animal Imaging Facility at The UT MD Anderson Cancer Center is supported by the NIH/NCI
598 Cancer Center Support Grant P30CA016672. This work was supported by the CPRIT Research
599 Training Award CPRIT Training Program (RP210028) (E.B.), NIH R21CA226301 (F.L.M.), NIH
600 CDP SPORE P50CA127001-07 (F.L.M.), NIH SPORE 2P50CA127001-11A1(F.L.M), ACS
601 RSG-15-145-01-CDD (F.L.M), NCCN YIA170032 (F.L.M. Young Investigator Award), Elsa U.

602 Pardee Foundation (F.L.M.), The Uncle Kory Foundation (F.L.M), The Larry Deaven Fellowship,
603 MD Anderson UT Health Graduate School of Biomedical Sciences (S.K) and CPRIT Research
604 Training Grant (RP170067) (S.K).

605 **Author's contributions**

606 SK and FLM conceived the study and designed the experiments. SK and YL performed all
607 intracranial animal experiments, including drug treatments and MRI imaging, with help from KA
608 and SC. SK, YH, YC, EB, AP, and TN calculated tumor volumes from MRI scans. SK and FLM
609 analyzed the data from all *in vivo* experiments. JA, AP, and TN performed immunohistochemistry
610 and EC scanned the histology slides. YH performed *in vivo* metabolomics experiments and JA
611 performed mass-spectrometry analysis. SK, YC, WH, FB, YS, and SG analyzed the
612 transcriptomic data. MNU synthesized HEX for animal treatments. DG assisted with the logistics
613 for animal experiments, data analysis and figure preparations. SM provided financial support, and
614 RAD provided key insights on the study and supervised experiments. SK wrote the manuscripts
615 with assistance from FLM and VCY. All authors approved the final manuscript.

616 **Acknowledgements**

617 We thank Charles Kingsley and the team from MD Anderson SAIF for their assistance with MRI
618 scans of intracranial tumors. We thank the Editing Services team at Research Medical Library at
619 the University of Texas MD Anderson Cancer Center for the editorial support on our manuscript.
620 We thank Michael Hazel from Crown Bioscience, Dr. Seth Gammon, Dr. Brian Engel from MD
621 Anderson Cancer Center for helpful discussions pertinent to our investigation.

622

623 References:

624 1. *AVASTIN (bevacizumab) injection, for intravenous use*.
625 https://www.gene.com/download/pdf/avastin_prescribing.pdf.

626 2. Hattingen, E. *et al.* Bevacizumab impairs oxidative energy metabolism and shows
627 antitumoral effects in recurrent glioblastomas: a 31P/1H MRSI and quantitative magnetic
628 resonance imaging study. *Neuro-Oncol.* **13**, 1349–1363 (2011).

629 3. McIntyre, A. & Harris, A. L. Metabolic and hypoxic adaptation to anti-angiogenic therapy: a
630 target for induced essentiality. *EMBO Mol. Med.* **7**, 368–379 (2015).

631 4. Hurwitz, H. *et al.* Bevacizumab plus irinotecan, fluorouracil, and leucovorin for metastatic
632 colorectal cancer. *N. Engl. J. Med.* **350**, 2335–2342 (2004).

633 5. Keunen, O. *et al.* Anti-VEGF treatment reduces blood supply and increases tumor cell
634 invasion in glioblastoma. *Proc. Natl. Acad. Sci. U. S. A.* **108**, 3749–3754 (2011).

635 6. Mittal, K., Ebos, J. & Rini, B. Angiogenesis and the tumor microenvironment: vascular
636 endothelial growth factor and beyond. *Semin. Oncol.* **41**, 235–251 (2014).

637 7. Friedman, H. S. *et al.* Bevacizumab alone and in combination with irinotecan in recurrent
638 glioblastoma. *J. Clin. Oncol. Off. J. Am. Soc. Clin. Oncol.* **27**, 4733–4740 (2009).

639 8. Wick, W. *et al.* Lomustine and Bevacizumab in Progressive Glioblastoma. *N. Engl. J. Med.*
640 **377**, 1954–1963 (2017).

641 9. Hu, Y.-L., Jahangiri, A., De Lay, M. & Aghi, M. K. Hypoxia-induced tumor cell autophagy
642 mediates resistance to anti-angiogenic therapy. *Autophagy* **8**, 979–981 (2012).

643 10. Bergers, G. & Hanahan, D. Modes of resistance to anti-angiogenic therapy. *Nat. Rev.*
644 *Cancer* **8**, 592–603 (2008).

645 11. Xu, J. *et al.* Colorectal cancer cells refractory to anti-VEGF treatment are vulnerable to
646 glycolytic blockade due to persistent impairment of mitochondria. *Mol. Cancer Ther.* **12**,
647 717–724 (2013).

648 12. Willett, C. G. *et al.* Direct evidence that the VEGF-specific antibody bevacizumab has
649 antivascular effects in human rectal cancer. *Nat. Med.* **10**, 145–147 (2004).
650 13. Mehta, S. *et al.* Assessing early therapeutic response to bevacizumab in primary breast
651 cancer using magnetic resonance imaging and gene expression profiles. *J. Natl. Cancer Inst.*
652 *Monogr.* **2011**, 71–74 (2011).
653 14. Van der Veldt, A. A. M. *et al.* Rapid decrease in delivery of chemotherapy to tumors
654 after anti-VEGF therapy: implications for scheduling of anti-angiogenic drugs. *Cancer Cell*
655 **21**, 82–91 (2012).
656 15. Jahangiri, A. *et al.* Gene expression profile identifies tyrosine kinase c-Met as a
657 targetable mediator of antiangiogenic therapy resistance. *Clin. Cancer Res. Off. J. Am. Assoc.*
658 *Cancer Res.* **19**, 1773–1783 (2013).
659 16. Yopp, A. C. *et al.* Antiangiogenic therapy for primary liver cancer: correlation of
660 changes in dynamic contrast-enhanced magnetic resonance imaging with tissue hypoxia
661 markers and clinical response. *Ann. Surg. Oncol.* **18**, 2192–2199 (2011).
662 17. DeLay, M. *et al.* Microarray analysis verifies two distinct phenotypes of glioblastomas
663 resistant to antiangiogenic therapy. *Clin. Cancer Res. Off. J. Am. Assoc. Cancer Res.* **18**,
664 2930–2942 (2012).
665 18. Semenza, G. L. Oxygen sensing, hypoxia-inducible factors, and disease
666 pathophysiology. *Annu. Rev. Pathol.* **9**, 47–71 (2014).
667 19. Favaro, E., Lord, S., Harris, A. L. & Buffa, F. M. Gene expression and hypoxia in breast
668 cancer. *Genome Med.* **3**, 55 (2011).
669 20. DeBerardinis, R. J. & Chandel, N. S. Fundamentals of cancer metabolism. *Sci. Adv.* **2**,
670 e1600200 (2016).
671 21. DeBerardinis, R. J. & Chandel, N. S. We need to talk about the Warburg effect. *Nat.*
672 *Metab.* **2**, 127–129 (2020).

673 22. Martínez-Reyes, I. & Chandel, N. S. Cancer metabolism: looking forward. *Nat. Rev.*
674 *Cancer* **21**, 669–680 (2021).
675 23. Owen, O. E., Kalhan, S. C. & Hanson, R. W. The key role of anaplerosis and
676 cataplerosis for citric acid cycle function. *J. Biol. Chem.* **277**, 30409–30412 (2002).
677 24. Fack, F. *et al.* Bevacizumab treatment induces metabolic adaptation toward anaerobic
678 metabolism in glioblastomas. *Acta Neuropathol. (Berl.)* **129**, 115–131 (2015).
679 25. Thompson, E. M., Frenkel, E. P. & Neuwelt, E. A. The paradoxical effect of
680 bevacizumab in the therapy of malignant gliomas. *Neurology* **76**, 87–93 (2011).
681 26. Pope, W. B., Lai, A., Nghiemphu, P., Mischel, P. & Cloughesy, T. F. MRI in patients
682 with high-grade gliomas treated with bevacizumab and chemotherapy. *Neurology* **66**, 1258–
683 1260 (2006).
684 27. Moustakas, A. & Kreisl, T. N. New treatment options in the management of
685 glioblastoma multiforme: a focus on bevacizumab. *OncoTargets Ther.* **3**, 27–38 (2010).
686 28. Ali, S. A. *et al.* Bevacizumab and irinotecan therapy in glioblastoma multiforme: a series
687 of 13 cases. *J. Neurosurg.* **109**, 268–272 (2008).
688 29. Narayana, A. *et al.* Antiangiogenic therapy using bevacizumab in recurrent high-grade
689 glioma: impact on local control and patient survival. *J. Neurosurg.* **110**, 173–180 (2009).
690 30. Bokstein, F., Shpigel, S. & Blumenthal, D. T. Treatment with bevacizumab and
691 irinotecan for recurrent high-grade glial tumors. *Cancer* **112**, 2267–2273 (2008).
692 31. Hirata, K., Yamaguchi, S., Shiga, T., Kuge, Y. & Tamaki, N. The Roles of Hypoxia
693 Imaging Using 18F-Fluoromisonidazole Positron Emission Tomography in Glioma
694 Treatment. *J. Clin. Med.* **8**, 1088 (2019).
695 32. Lin, Y.-H. *et al.* An enolase inhibitor for the targeted treatment of ENO1-deleted
696 cancers. *Nat. Metab.* **2**, 1413–1426 (2020).

697 33. Barekatain, Y. *et al.* Quantification of Phosphonate Drugs by 1H-31P HSQC Shows
698 That Rats Are Better Models of Primate Drug Exposure than Mice. *Anal. Chem.* **94**, 10045–
699 10053 (2022).
700 34. Yu, L. *et al.* Interaction between bevacizumab and murine VEGF-A: a reassessment.
701 *Invest. Ophthalmol. Vis. Sci.* **49**, 522–527 (2008).
702 35. Nakamura, K. *et al.* KRN951, a highly potent inhibitor of vascular endothelial growth
703 factor receptor tyrosine kinases, has antitumor activities and affects functional vascular
704 properties. *Cancer Res.* **66**, 9134–9142 (2006).
705 36. Gammon, S. T. *et al.* Mechanism-Specific Pharmacodynamics of a Novel Complex-I
706 Inhibitor Quantified by Imaging Reversal of Consumptive Hypoxia with [18F]FAZA PET In
707 Vivo. *Cells* **8**, 1487 (2019).
708 37. Khadka, S. *et al.* Impaired anaplerosis is a major contributor to glycolysis inhibitor
709 toxicity in glioma. *Cancer Metab.* **9**, 27 (2021).
710 38. Molina, J. R. *et al.* An inhibitor of oxidative phosphorylation exploits cancer
711 vulnerability. *Nat. Med.* **24**, 1036–1046 (2018).
712 39. Pfeifer, G., Frenkel, C. & Entzian, W. Pharmacokinetic aspects of cerebrospinal fluid
713 penetration of fosfomycin. *Int. J. Clin. Pharmacol. Res.* **5**, 171–174 (1985).
714 40. Sun, Y. *et al.* Functional Genomics Reveals Synthetic Lethality between
715 Phosphogluconate Dehydrogenase and Oxidative Phosphorylation. *Cell Rep.* **26**, 469-482.e5
716 (2019).
717 41. Indraccolo, S. *et al.* Metformin: a modulator of bevacizumab activity in cancer? A case
718 report. *Cancer Biol. Ther.* **16**, 210–214 (2015).
719 42. Markowska, A., Sajdak, S., Markowska, J. & Huczyński, A. Angiogenesis and cancer
720 stem cells: New perspectives on therapy of ovarian cancer. *Eur. J. Med. Chem.* **142**, 87–94
721 (2017).

722 43. Marrone, K. A. *et al.* A Randomized Phase II Study of Metformin plus
723 Paclitaxel/Carboplatin/Bevacizumab in Patients with Chemotherapy-Naïve Advanced or
724 Metastatic Nonsquamous Non-Small Cell Lung Cancer. *The Oncologist* **23**, 859–865 (2018).
725 44. Yap, T. A. *et al.* Complex I inhibitor of oxidative phosphorylation in advanced solid
726 tumors and acute myeloid leukemia: phase I trials. *Nat. Med.* **29**, 115–126 (2023).
727 45. Schulte, M. L. *et al.* Pharmacological blockade of ASCT2-dependent glutamine
728 transport leads to antitumor efficacy in preclinical models. *Nat. Med.* **24**, 194–202 (2018).
729 46. Egler, R. A., Ahuja, S. P. & Matloub, Y. L-asparaginase in the treatment of patients with
730 acute lymphoblastic leukemia. *J. Pharmacol. Pharmacother.* **7**, 62–71 (2016).
731 47. Sanderson, S. M., Gao, X., Dai, Z. & Locasale, J. W. Methionine metabolism in health
732 and cancer: a nexus of diet and precision medicine. *Nat. Rev. Cancer* **19**, 625–637 (2019).
733 48. Miraki-Moud, F. *et al.* Arginine deprivation using pegylated arginine deiminase has
734 activity against primary acute myeloid leukemia cells in vivo. *Blood* **125**, 4060–4068 (2015).
735 49. Kelly, M. P. *et al.* Arginine deiminase PEG20 inhibits growth of small cell lung cancers
736 lacking expression of argininosuccinate synthetase. *Br. J. Cancer* **106**, 324–332 (2012).
737 50. Duncan, C. G. *et al.* Integrated genomic analyses identify ERRFI1 and TACC3 as
738 glioblastoma-targeted genes. *Oncotarget* **1**, 265–277 (2010).
739 51. Lal, S. *et al.* An implantable guide-screw system for brain tumor studies in small
740 animals. *J. Neurosurg.* **92**, 326–333 (2000).
741 52. Fedorov, A. *et al.* 3D Slicer as an image computing platform for the Quantitative
742 Imaging Network. *Magn. Reson. Imaging* **30**, 1323–1341 (2012).
743 53. Pertea, M., Kim, D., Pertea, G. M., Leek, J. T. & Salzberg, S. L. Transcript-level
744 expression analysis of RNA-seq experiments with HISAT, StringTie and Ballgown. *Nat.*
745 *Protoc.* **11**, 1650–1667 (2016).

746 54. Subramanian, A. *et al.* Gene set enrichment analysis: a knowledge-based approach for
747 interpreting genome-wide expression profiles. *Proc. Natl. Acad. Sci. U. S. A.* **102**, 15545–
748 15550 (2005).
749 55. Liberzon, A. *et al.* The Molecular Signatures Database (MSigDB) hallmark gene set
750 collection. *Cell Syst.* **1**, 417–425 (2015).
751 56. Guo, S., Jiang, X., Mao, B. & Li, Q.-X. The design, analysis and application of mouse
752 clinical trials in oncology drug development. *BMC Cancer* **19**, 718 (2019).
753 57. Bolger, A. M., Lohse, M. & Usadel, B. Trimmomatic: a flexible trimmer for Illumina
754 sequence data. *Bioinforma. Oxf. Engl.* **30**, 2114–2120 (2014).
755 58. Dobin, A. *et al.* STAR: ultrafast universal RNA-seq aligner. *Bioinforma. Oxf. Engl.* **29**,
756 15–21 (2013).
757 59. Bray, N. L., Pimentel, H., Melsted, P. & Pachter, L. Erratum: Near-optimal probabilistic
758 RNA-seq quantification. *Nat. Biotechnol.* **34**, 888 (2016).
759 60. Love, M. I., Huber, W. & Anders, S. Moderated estimation of fold change and
760 dispersion for RNA-seq data with DESeq2. *Genome Biol.* **15**, 550 (2014).
761 61. Yu, G., Wang, L.-G., Han, Y. & He, Q.-Y. clusterProfiler: an R package for comparing
762 biological themes among gene clusters. *Omics J. Integr. Biol.* **16**, 284–287 (2012).
763

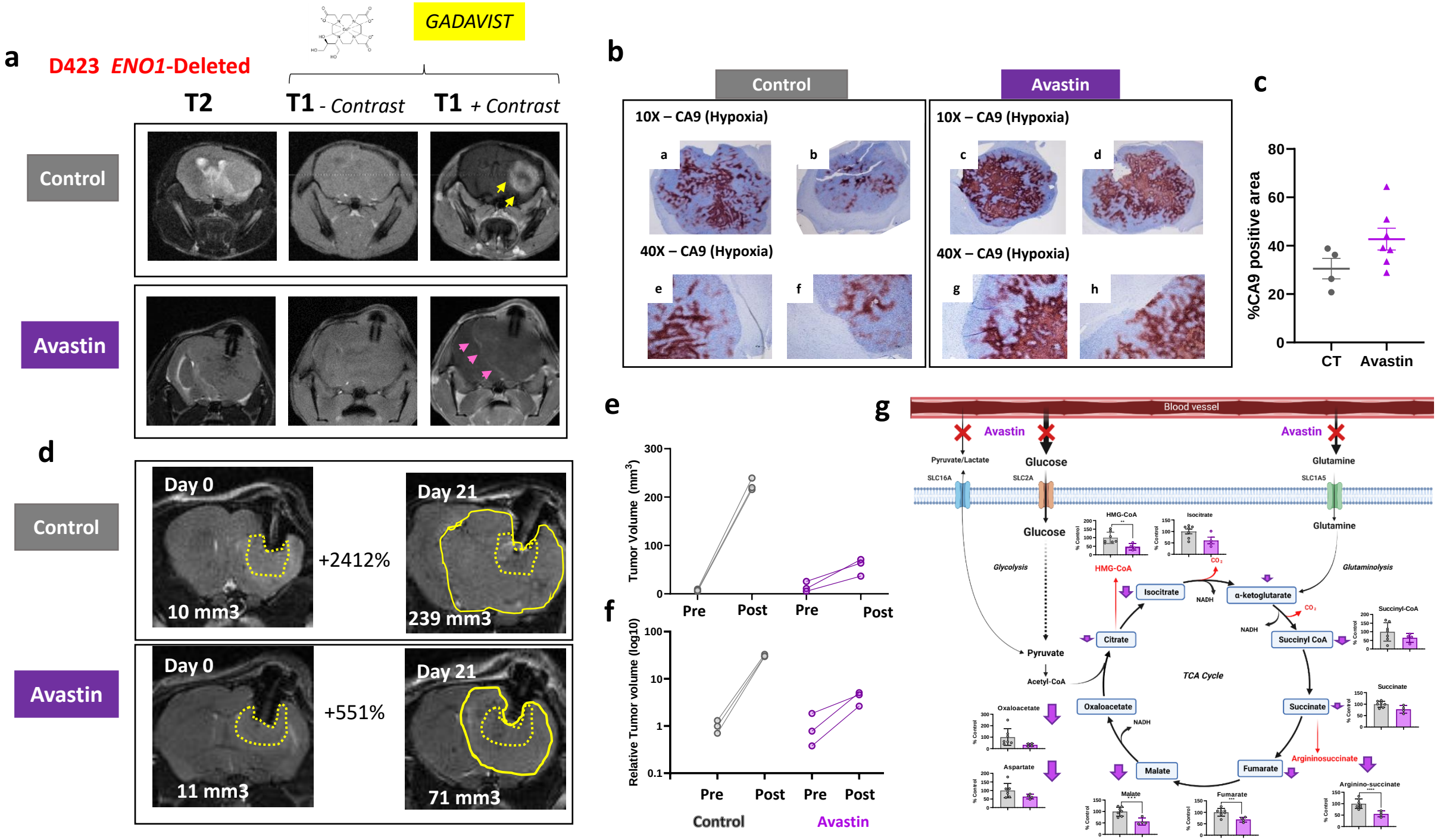
a
D423 ENO1-Deleted
GADAVIST
T2
T1 - Contrast
T1 + Contrast
Control
Avastin
b
Control
Avastin
10X – CA9 (Hypoxia)
40X – CA9 (Hypoxia)
c
%CA9 positive area
CT
Avastin
d
Day 0
Day 21
10 mm3
239 mm3
+2412%
11 mm3
71 mm3
+551%
e
Tumor Volume (mm3)
Pre
Post
f
Relative Tumor volume (log10)
Control
Avastin
g
Blood vessel
Avastin
Pyruvate/Lactate
Glucose
Glutamine
SLC16A
SLC2A
SLC1A5
Glycolysis
Glutaminolysis
HMG-CoA
Isocitrate
α-ketoglutarate
Succinyl CoA
Citrate
Pyruvate
Acetyl-CoA
TCA Cycle
Oxaloacetate
Succinate
Fumarate
Malate
Argininosuccinate
Aspartate
NADH

Figure 1: **Angiogenesis inhibition re-seals the breached blood brain barrier, impairs perfusion and nutrient import, and modestly inhibits tumor growth. a.** Intracranial tumors were generated by implanting D423 *ENO1* homozygously deleted glioma cells in Foxn1$^{nu/nu}$ nude mice. Tumor growth was followed by T2-weighted MRI every two weeks. Animals in the Avastin group were treated with Avastin (5mpk, x2 per week). After one week of treatment, T1 MRI with and without contrast (Gadavist, IV) was performed on untreated and Avastin treated mice. Untreated tumors exhibited consistent contrast enhancement (yellow arrows), indicative of a breached blood-brain-barrier(BBB) in these tumors. Avastin treated tumors showed a dramatic decrease in contrast enhancement, with a residual weak signal apparent at the tumor edges (pink arrows), suggesting an effective resealing of the BBB by Avastin treatment. **b-c.** Avastin treatment causes significant elevation in hypoxia, determined by the carbonic anhydrase 9 (CA9, a hypoxia marker) staining in intracranial tumors (**b**). Quantification of hypoxic areas (brown) in tumors are plotted (**c**). **d-e.** T2-weighted MRI scans showing the size of the tumors on day zero (dotted yellow line) and on day 21 (solid yellow line). Tumor volumes are indicated on the bottom left corner of each image. Pre- and post-treatment tumor volume comparisons (raw and relative) of control and Avastin treated mice after 21 days of treatment. **f.** Angiogenesis inhibition by Avastin significantly impairs import of major blood borne anaplerotic nutrients into the tumors, resulting in significant metabolic stress in tumors. Avastin treatment leads to a global decrease in TCA cycle intermediates, which are crucial for the generation of biosynthetic intermediates in cancer cells. Data are mean ± SD. Asterik(*) represents statistical significance ($p<0.05$) achieved by two-tailed t-test (**g**).

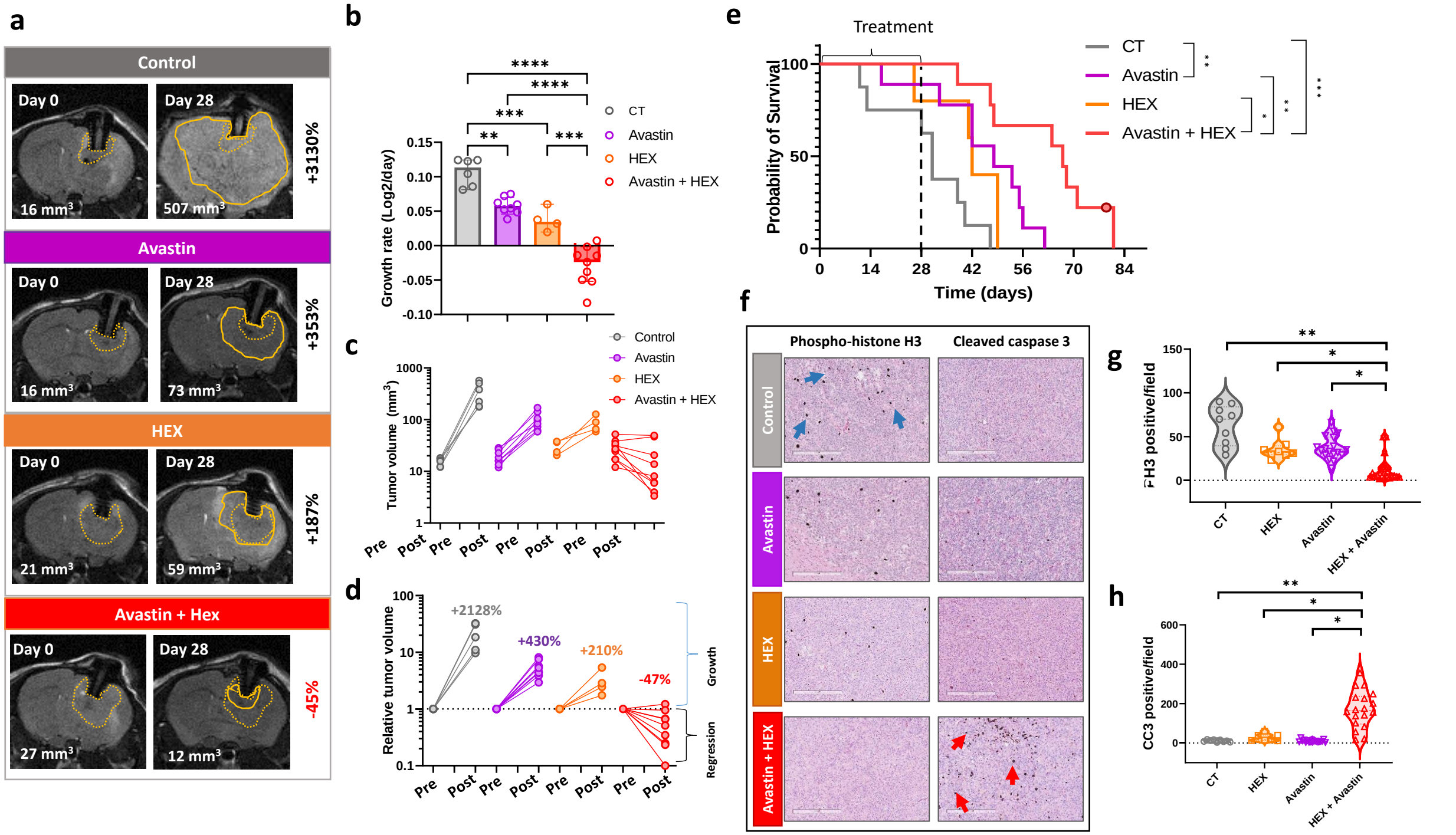
a
Control
Day 0
16 mm³
Day 28
507 mm³
+3130%
Avastin
Day 0
16 mm³
Day 28
73 mm³
+353%
HEX
Day 0
21 mm³
Day 28
59 mm³
+187%
Avastin + Hex
Day 0
27 mm³
Day 28
12 mm³
-45%
b
Growth rate (Log2/day)
CT
Avastin
HEX
Avastin + HEX
c
Tumor volume (mm³)
Control
Avastin
HEX
Avastin + HEX
Pre
Post
d
Relative tumor volume
+2128%
+430%
+210%
-47%
Growth
Regression
e
Treatment
Probability of Survival
Time (days)
CT
Avastin
HEX
Avastin + HEX
f
Phospho-histone H3
Cleaved caspase 3
Control
Avastin
HEX
Avastin + HEX
g
PH3 positive/field
CT
HEX
Avastin
HEX + Avastin
h
CC3 positive/field
CT
HEX
Avastin
HEX + Avastin

Figure 2: **Long-term combination of angiogenesis inhibitor Avastin and Enolase inhibitor HEX results in regression of intracranial tumors at doses where either drug is only tumor-static as a monotherapy.**
Intracranial tumors were generated in Foxn1 $^{nu/nu}$ nude mice by implanting D423 *ENO1* homozygously deleted glioma cells and tumor growth was monitored every week by T2-weighted MRI. Four weeks later, when tumors reached approximately 20 mm^3 in volume, mice were separated into four groups; control(vehicle), Avastin (5 mpk, 2X per week), Enolase inhibitor HEX (225 mpk, 12X per week) or Avastin plus HEX (Avastin, 5mpk 2X per week + 225 mpk SC 12X per week) were administered for 28 days. MRI scans were taken every two weeks to monitor tumor growth in response to treatment, and tumor volume changes were calculated. **a.** T2-weighted MRI images of animals before and after 28 days of treatment with tumor volumes indicated in mm^3 in the lower left corner of the image; initial tumor outlines are shown in dotted yellow lines, while tumors after 28 days are shown in solid lines. **b-d**. Growth rates of tumors (**b**) and pre- and post-treatment tumor volume (**c-d**) in different treatment groups. Treatment with Avastin or HEX as single agents substantially attenuated tumor growth but did not result in actual tumor regression. However, the combination of Avastin with HEX resulted in tumor regression in all treated animals, and a complete eradication of tumors in some animals. Animals were taken off the treatments on day 28 and probability of survival after treatment discontinuation in each group was determined. Highlighted data point indicates mouse that died of reasons unrelated to tumor burden. **e**. Avastin and HEX combination lead to a significant extension of survival compared to HEX and Avastin alone. **f-i.** Histopathological analyses of brain tumor sections extracted from the mice show a dramatic reduction in phospho-histone H3 (PH3) positive cells (**f,g**) (an index of proliferation, blue arrows in the picture) in tumors treated with the combination of Avastin and HEX, concomitant to a dramatic increase in dying cells cleaved caspase 3 (CC3) positive cells (**f,h**), (an index of apoptosis, red arrows in picture), compared to the control, Avastin and HEX groups. Data are mean ± SD. Asterik(*) represents statistical significance ($p<0.05$) achieved by ordinary one-way ANOVA and Tukey's multiple comparisons test (**b**,**g,h**).

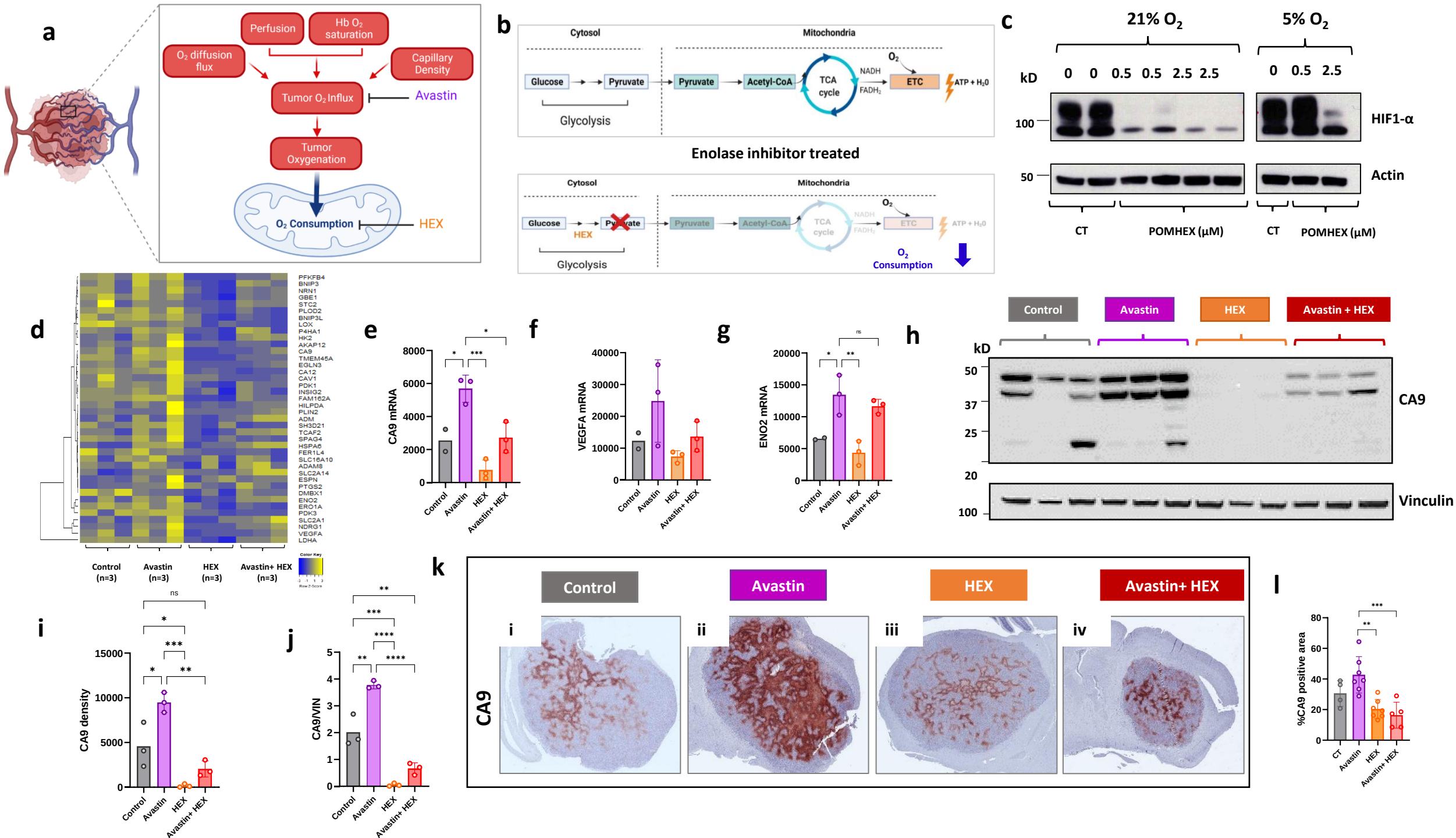
a
Perfusion
Hb O2 saturation
O2 diffusion flux
Capillary Density
Tumor O2 Influx
Avastin
Tumor Oxygenation
O2 Consumption
HEX
b
Cytosol
Mitochondria
Glucose
Pyruvate
Pyruvate
Acetyl-CoA
TCA cycle
NADH
FADH2
O2
ETC
ATP + H2O
Glycolysis
Enolase inhibitor treated
HEX
O2 Consumption
c
21% O2
5% O2
kD
0 0 0.5 0.5 2.5 2.5
0 0.5 2.5
100
50
HIF1-α
Actin
CT
POMHEX (μM)
CT
POMHEX (μM)
d
PFKFB4
BNIP3
NRN1
GBE1
STC2
PLOD2
BNIP3L
LOX
P4HA1
HK2
AKAP12
CA9
TMEM45A
EGLN3
CA12
CAV1
PDK1
INSIG2
FAM162A
HILPDA
PLIN2
ADM
SH3D21
TCAF2
SPAG4
HSPA6
FER1L4
SLC16A10
ADAM8
SLC2A14
ESPN
PTGS2
DMBX1
ENO2
ERO1A
PDK3
SLC2A1
NDRG1
VEGFA
LDHA
Control (n=3)
Avastin (n=3)
HEX (n=3)
Avastin+ HEX (n=3)
Color Key
Row Z-Score
e
CA9 mRNA
Control
Avastin
HEX
Avastin+ HEX
f
VEGFA mRNA
g
ENO2 mRNA
h
Control
Avastin
HEX
Avastin + HEX
kD
50
37
25
20
100
CA9
Vinculin
i
CA9 density
j
CA9/VIN
k
Control
Avastin
HEX
Avastin+ HEX
CA9
i
ii
iii
iv
l
%CA9 positive area
CT
Avastin
HEX
Avastin+ HEX

Figure 3: **Combination of Avastin and HEX decreases hypoxia in intracranial tumors by limiting oxygen consumption. a.** Illustrations depicting the roles of vascular perfusion and tumor intrinsic oxygen consuming reactions in overall oxygen tension in the tumors. Hypoxia is a dynamic process and can arise as a result of poor oxygen delivery from the vasculature (perfusion hypoxia) or due to enhanced oxygen consumption by the tumor cells (consumptive hypoxia), or possibly, due to an imbalance in the rates of these two processes. **b.** Schematic demonstrating that mitochondrial oxidative phosphorylation is substrate limited. Inhibition of glycolysis with the POMHEX, a prodrug of Enolase inhibitor HEX, constrains oxidative phosphorylation (oxygen consumption) by blocking formation of pyruvate and decreases consumptive hypoxia. **c**. Western blots showing the effect of glycolysis inhibition by POMHEX on hypoxia (CA9 as a hypoxia marker) in cells *in vitro* in normoxic and hypoxic conditions. **d.** Heatmap representing mRNA transcript levels for hypoxia responsive genes in tumors in each treatment groups. Heatmap shows top 40 hypoxia responsive genes selected from the mRNA profiling studies in the TCGA GBM dataset by correlating CA9 transcript levels (spearman coefficient>0.5) with the whole genome transcripts. **e-g**. Raw mRNA reads of three well-established hypoxia responsive genes, CA9 (**e**), VEGFA (**f**) and ENO2 (**g**) are shown. **h-j**. Immunoblot of intracranial tumors from different treatment groups, showing hypoxia markers CA9 with vinculin as a loading control (**h**). Densitometry analyses of total CA9 signals on each treatment group expressed as total density of signal (**i**) and density of signal relative to the loading control (**j**). **k-l.** Intracranial tumors from mice in control, HEX, Avastin, Avastin and HEX treatment groups, stained with the hypoxia marker CA9 (**k**). Quantification of hypoxic areas (brown) in tumors are plotted for different treatment groups (**l**). Avastin significantly elevates hypoxia in tumors by inhibiting tumor vascularization and impairing perfusion, but HEX treatment reduces hypoxia by inhibiting pyruvate production and suppressing consumptive hypoxia. Avastin and HEX impose a competitive effect on hypoxia, possibly as Avastin elevates perfusion hypoxia while HEX suppresses consumptive hypoxia, leading to a net decrease in intra-tumoral hypoxia. Immunoblot analyses corroborate the results of histopathological analyses, that Avastin and HEX combination significantly decreases hypoxia in intracranial tumors. Data are mean ± SD. Asterik(*) represents statistical significance ($p<0.05$) achieved by ordinary one-way ANOVA and Tukey's multiple comparisons test (**e,f,g,h,I,j,l**).

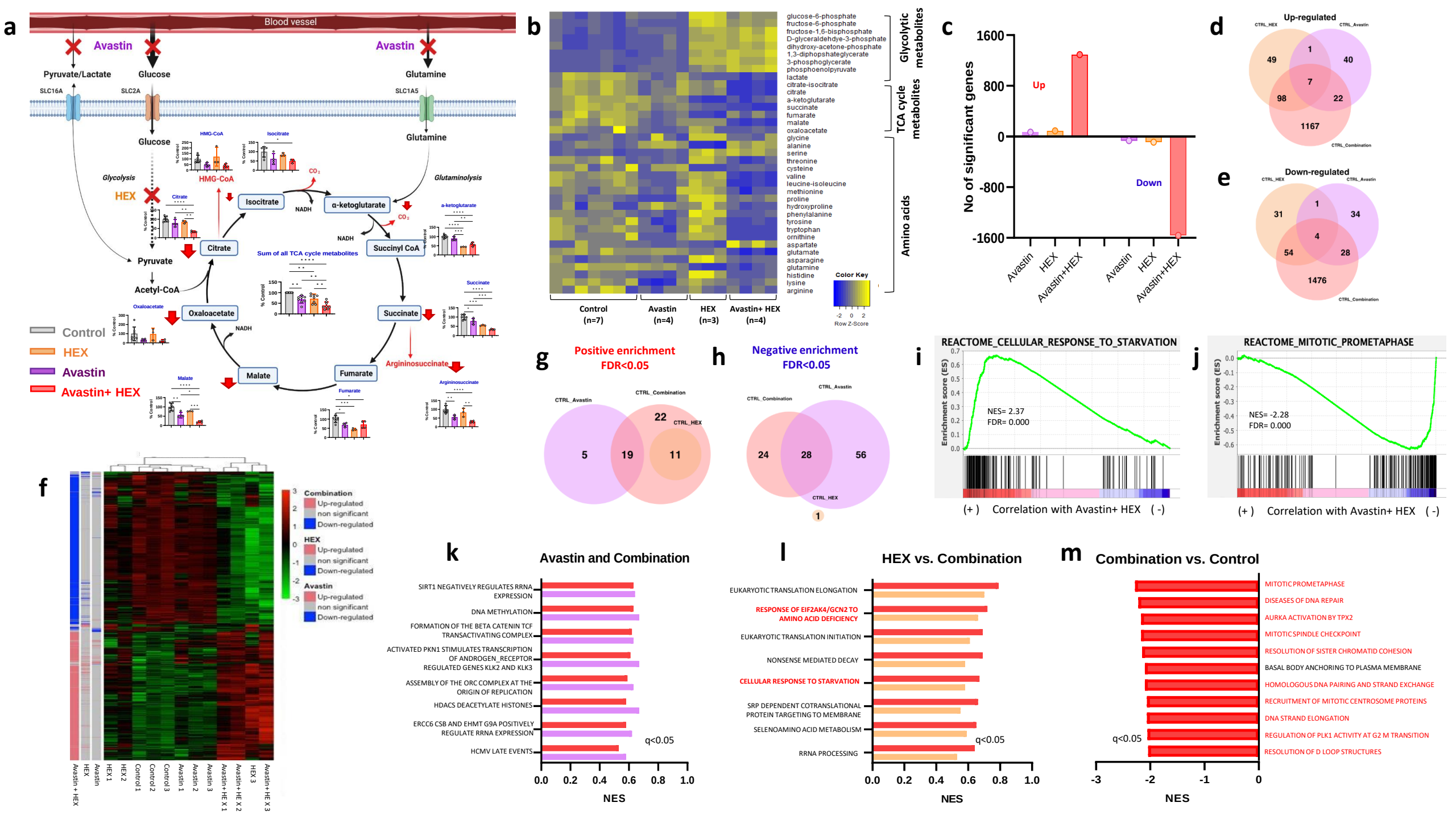
a
Blood vessel
Avastin
Avastin
Pyruvate/Lactate
Glucose
Glutamine
SLC16A
SLC2A
SLC1A5
Glucose
Glutamine
Glycolysis
Glutaminolysis
HEX
HMG-CoA
Isocitrate
α-ketoglutarate
Citrate
Succinyl CoA
Pyruvate
Acetyl-CoA
Oxaloacetate
Succinate
Malate
Fumarate
Argininosuccinate
NADH
Sum of all TCA cycle metabolites
Control
HEX
Avastin
Avastin+ HEX
b
Glycolytic metabolites
TCA cycle metabolites
Amino acids
Control (n=7)
Avastin (n=4)
HEX (n=3)
Avastin+ HEX (n=4)
Color Key
Row Z-Score
c
No of significant genes
Up
Down
Avastin
HEX
Avastin+HEX
d
Up-regulated
CTRL_HEX
CTRL_Avastin
CTRL_Combination
e
Down-regulated
f
Combination
Up-regulated
non significant
Down-regulated
HEX
Avastin
g
Positive enrichment
FDR<0.05
CTRL_Avastin
CTRL_Combination
CTRL_HEX
h
Negative enrichment
FDR<0.05
CTRL_Combination
CTRL_Avastin
CTRL_HEX
i
REACTOME_CELLULAR_RESPONSE_TO_STARVATION
Enrichment score (ES)
NES= 2.37
FDR= 0.000
(+) Correlation with Avastin+ HEX (-)
j
REACTOME_MITOTIC_PROMETAPHASE
NES= -2.28
FDR= 0.000
(+) Correlation with Avastin+ HEX (-)
k
Avastin and Combination
SIRT1 NEGATIVELY REGULATES RRNA EXPRESSION
DNA METHYLATION
FORMATION OF THE BETA CATENIN TCF TRANSACTIVATING COMPLEX
ACTIVATED PKN1 STIMULATES TRANSCRIPTION OF ANDROGEN_RECEPTOR REGULATED GENES KLK2 AND KLK3
ASSEMBLY OF THE ORC COMPLEX AT THE ORIGIN OF REPLICATION
HDACS DEACETYLATE HISTONES
ERCC6 CSB AND EHMT G9A POSITIVELY REGULATE RRNA EXPRESSION
HCMV LATE EVENTS
q<0.05
NES
l
HEX vs. Combination
EUKARYOTIC TRANSLATION ELONGATION
RESPONSE OF EIF2AK4/GCN2 TO AMINO ACID DEFICIENCY
EUKARYOTIC TRANSLATION INITIATION
NONSENSE MEDIATED DECAY
CELLULAR RESPONSE TO STARVATION
SRP DEPENDENT COTRANSLATIONAL PROTEIN TARGETING TO MEMBRANE
SELENOAMINO ACID METABOLISM
RRNA PROCESSING
q<0.05
NES
m
Combination vs. Control
MITOTIC PROMETAPHASE
DISEASES OF DNA REPAIR
AURKA ACTIVATION BY TPX2
MITOTIC SPINDLE CHECKPOINT
RESOLUTION OF SISTER CHROMATID COHESION
BASAL BODY ANCHORING TO PLASMA MEMBRANE
HOMOLOGOUS DNA PAIRING AND STRAND EXCHANGE
RECRUITMENT OF MITOTIC CENTROSOME PROTEINS
DNA STRAND ELONGATION
REGULATION OF PLK1 ACTIVITY AT G2 M TRANSITION
RESOLUTION OF D LOOP STRUCTURES
q<0.05
NES

Figure 4: Tumors under combined angiogenesis and enolase inhibition show profound anaplerotic nutrient stress. a. TCA cycle map representing metabolites from metabolomic analysis of snap frozen micro-dissected intracranial xenografts of *ENO1* homozygously deleted D423 cells from control, Avastin, HEX or Avastin+HEX groups. Red arrow indicates the degree of decrease in Avastin and HEX treatment relative to control. TCA cycle metabolite depletion achieved by Avastin treatment alone is significantly exaggerated by the addition of the Enolase inhibitor HEX. HEX inhibits anaplerotic pyruvate formation from glucose, and together with Avastin causes greater anaplerotic deficit on the tumors. **b**. Heatmap representing the changes in glycolytic and TCA cycle metabolites and amino acids in the intracranial tumors in control, Avastin, HEX, and Avastin+HEX groups. **c**. Bar-graph showing differentially expressed genes (DEGs) that are statistically significant in different treatment groups (Up: $\log2Fc \geq 1$ and $padj \leq 0.05$; Down: $\log2Fc \leq -1$ and $padj \leq 0.05$). **d-e**. Venn-diagram showing the number of DEGs that are common or unique to each treatment group relative to control. **f**. Heatmap showing statistically significant DEGs in each treatment group. Genes that are up- or down-regulated in each treatment relative to controls are shown. **g,h.** Venn-diagrams representing the gene set enrichment analysis (GSEA) of DEGs relative to control. The number of GSEA reactome pathways that are unique to or overlapping between different treatment groups are shown. **i,j.** GSEA plots showing positive enrichment of genes in the cellular response to starvation pathway and negative enrichment of genes in the mitotic and pro-metaphase geneset. **k,l.** Normalized enrichment score showing the GSEA reactome pathways that are positively enriched ($FDR(q)<0.05$) in Avastin and Avastin+HEX, and HEX and Avastin+HEX groups. Highlighted in red are pathways that are relevant to cellular nutrient deficiency response. **m**. GSEA reactome pathways that are negatively enriched in Avastin and HEX treatment group relative to control. Highlighted in red are pathways that are relevant in proliferation. Data are mean ± SD. Asterik(*) represents statistical significance ($p<0.05$) achieved by ordinary one-way ANOVA and Tukey's multiple comparisons test (**a**).

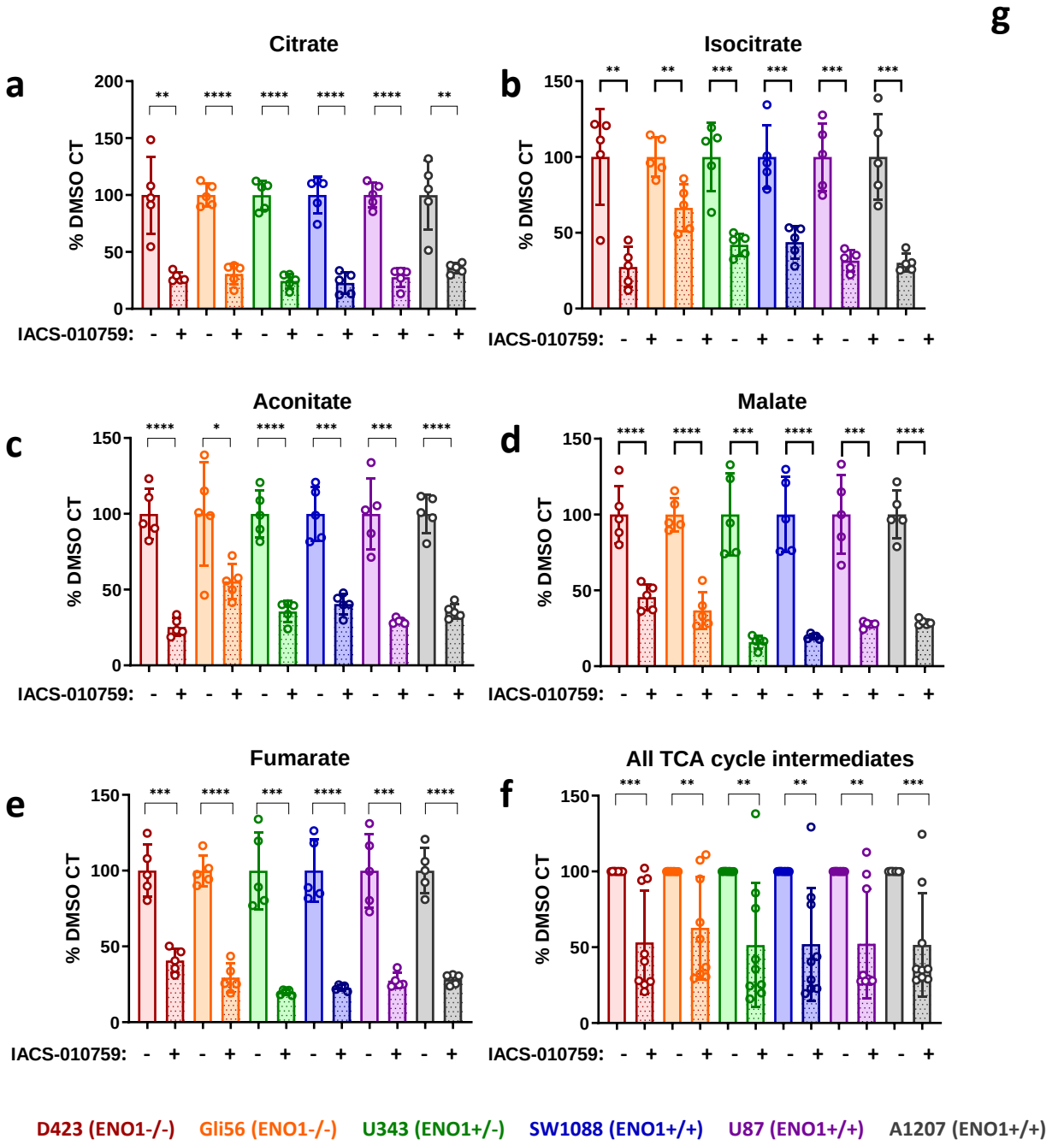
a
Citrate
b
Isocitrate
c
Aconitate
d
Malate
e
Fumarate
f
All TCA cycle intermediates
% DMSO CT
IACS-010759:
D423 (ENO1-/-)
Gli56 (ENO1-/-)
U343 (ENO1+/-)
SW1088 (ENO1+/+)
U87 (ENO1+/+)
A1207 (ENO1+/+)

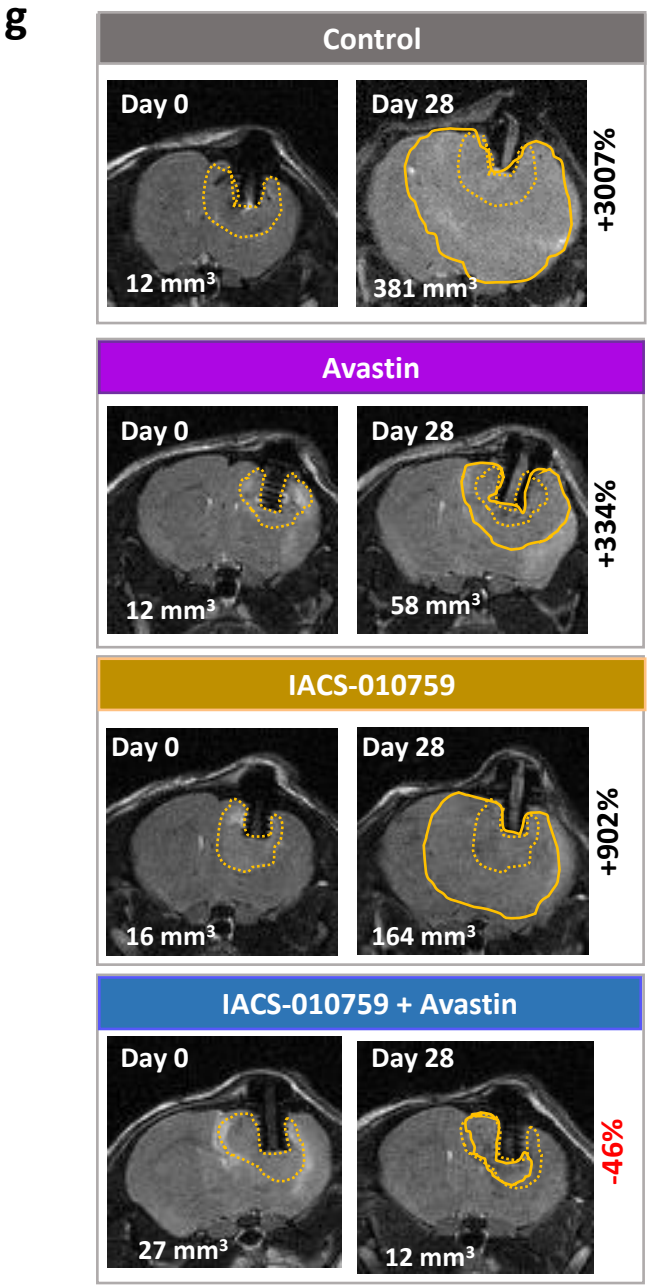
g
Control
Day 0
12 mm³
Day 28
381 mm³
+3007%
Avastin
Day 0
12 mm³
Day 28
58 mm³
+334%
IACS-010759
Day 0
16 mm³
Day 28
164 mm³
+902%
IACS-010759 + Avastin
Day 0
27 mm³
Day 28
12 mm³
-46%

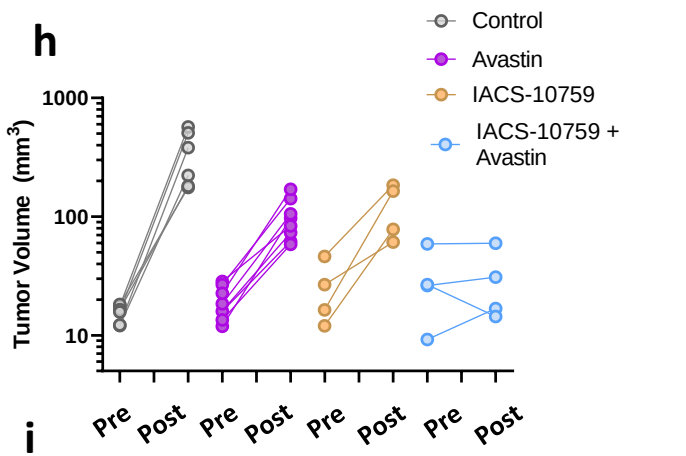
h
Control
Avastin
IACS-10759
IACS-10759 + Avastin
Tumor Volume (mm³)
Pre
Post

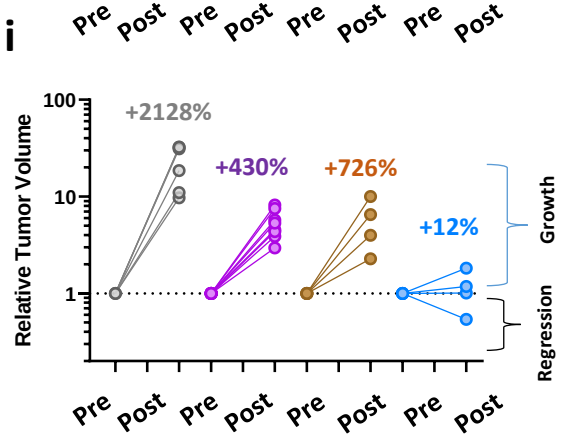
i
Relative Tumor Volume
+2128%
+430%
+726%
+12%
Growth
Regression
Pre
Post

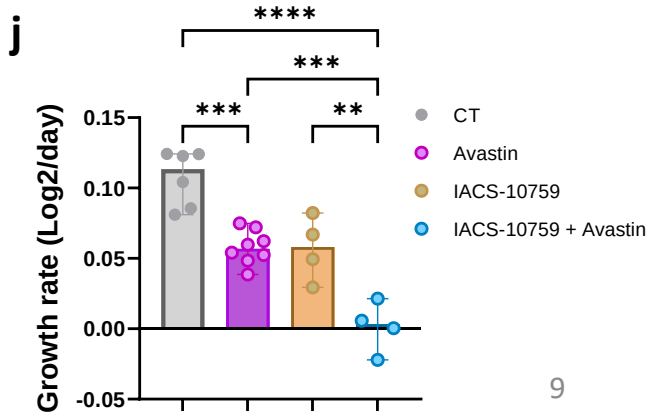
j
Growth rate (Log2/day)
CT
Avastin
IACS-10759
IACS-10759 + Avastin

Figure 5: Avastin and the Complex I inhibitor IACS-010759 synergize to abolish grow of *ENO1*-deleted intracranial tumors. **a-f.** Inhibition of oxidative phosphorylation induces anaplerotic stress in cancer cells**.** Data shown is analyzed from the metabolomic analysis from (Molina et al, Nature Medicine, 2016). Briefly, *ENO1* deleted and *ENO1* intact cancer cells were treated with DMSO or the complex-I inhibitor IACS-010759 and metabolomics was performed to identify different metabolites that are altered in response to mitochondrial complex I inhibition. TCA cycle metabolites are universally diminished by IACS-010759 treatment compared to control in all cell lines irrespective of *ENO1* deletion. **g-j:** Intracranial tumors were generated by implanting *ENO1* deleted glioma cells in Foxn1 $^{nu/nu}$ nude mice. Tumor development was followed by T2-MRI. Treatment was begun when tumors reached ~20 mm^3. **g**. T2-MRI images of animals before and after 28 days of treatment with tumor volumes indicated in mm^3 in the lower part of the image; initial tumor outlines are shown in dotted yellow lines, while tumors after 28 days are shown in solid lines. **h**: Summary of tumor volume changes after 24 days on treatment. Animals were treated continuously with Avastin 2X per week IP, IACS-010759 5 mpk once daily by oral gavage. **i**. Tumor volume plots comparing pre-treatment and 28 days post-treatment raw and relative tumor volumes. j. Growth rate of tumor volumes in each treatment group. The effect of IACS-010759 in *ENO1* deleted gliomas is only marginal, but Avastin treatment led to a modest inhibition of tumor growth. Combination of IACS-010759 and Avastin resulted in significant suppression of tumor growth and a complete eradication of tumors in some cases. Data are mean ± SD. Asterik(*) represents statistical significance ($p<0.05$) achieved by two-tailed unpaired t-test (**a-f**) and ordinary one-way ANOVA and Tukey's multiple comparisons test (**J**). Note that tumor volume data for *ENO1* deleted tumors in control and Avastin treatment group represented in Figure 5 and Figure 2 are from the same experiment.

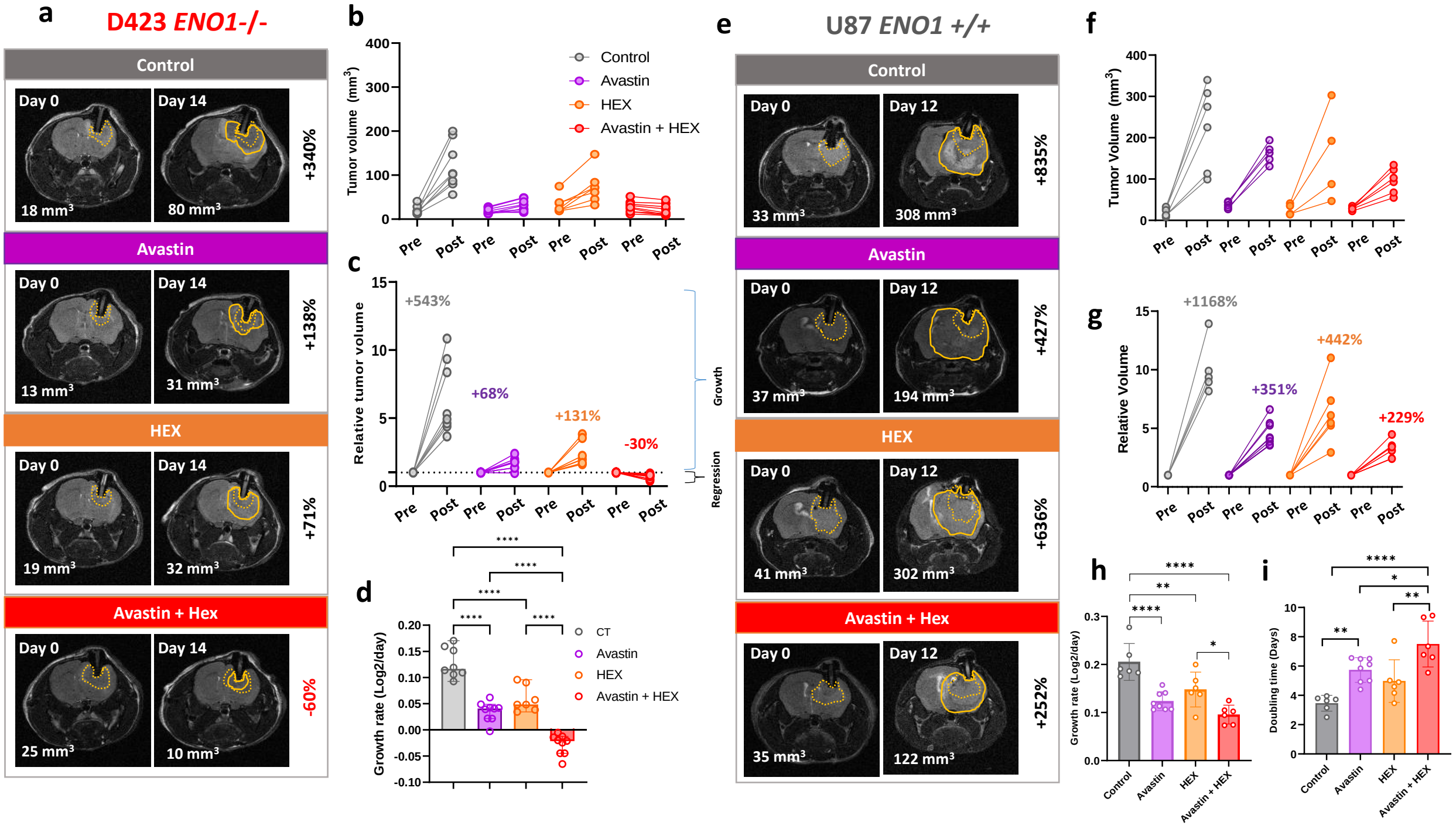
a
D423 ENO1-/-
Control
Day 0
18 mm³
Day 14
80 mm³
+340%
Avastin
Day 0
13 mm³
Day 14
31 mm³
+138%
HEX
Day 0
19 mm³
Day 14
32 mm³
+71%
Avastin + Hex
Day 0
25 mm³
Day 14
10 mm³
-60%
b
Tumor volume (mm³)
Control
Avastin
HEX
Avastin + HEX
Pre
Post
c
Relative tumor volume
+543%
+68%
+131%
-30%
Growth
Regression
d
Growth rate (Log2/day)
CT
Avastin
HEX
Avastin + HEX
****
e
U87 ENO1 +/+
Control
Day 0
33 mm³
Day 12
308 mm³
+835%
Avastin
Day 0
37 mm³
Day 12
194 mm³
+427%
HEX
Day 0
41 mm³
Day 12
302 mm³
+636%
Avastin + Hex
Day 0
35 mm³
Day 12
122 mm³
+252%
f
Tumor Volume (mm³)
g
Relative Volume
+1168%
+351%
+442%
+229%
h
Growth rate (Log2/day)
Control
Avastin
HEX
Avastin + HEX
i
Doubling time (Days)

Figure 6: **Synergistic anti-tumor effect in *ENO1*-deleted tumors and additive effect in *ENO1*-WT tumors by combination of angiogenesis and enolase inhibitor** Intracranial tumors were generated by implanting *ENO1* deleted D423 and *ENO1* intact U87 glioma cells in immunocompromised nude mice. Tumor development was followed by T2-MRI. T2-weighted MRI images of animal brains with *ENO1* deleted (**a**) or *ENO1* intact (**e**) before and after 14 days (*ENO1* deleted) or 12 days (*ENO1* intact) of treatment with tumor volumes indicated in mm^3 in the lower left corner of the image; initial tumor outlines are shown in dotted yellow lines, while tumors after 14 or 12 days are shown in solid lines. Animals were separated into four groups—Control (vehicle), Avastin (5 mpk, 2X per week), Enolase inhibitor HEX (225 mpk, 12X per week) or Avastin plus HEX (Avastin, 5mpk 2X per week + 225 mpk SC 12X per week) were administered. **a-d**: Summary of tumor volume changes and growth rates of *ENO1* deleted tumors after 14 days of treatment. **e-i**: Summary of tumor volume changes, growth rates and tumor volume doubling time of *ENO1* intact tumors after 12 days of treatment. HEX or Avastin as single agents suppress tumor growth in *ENO1* deleted tumors; the combination of HEX and Avastin causes a synergistic regression of *ENO1* deleted tumors at the doses administered. In *ENO1* WT tumors, the effect of Avastin and HEX as single agents is marginal, but the combination of the drugs exert an additive effect on tumor growth inhibition. Data are mean ± SD. Asterik (*) represents statistical significance ($p<0.05$) achieved ordinary one-way ANOVA and Tukey's multiple comparisons test (**d, h, i**). Note that Day 0 tumor volume data for *ENO1* deleted tumors represented in Figure 2 and Figure 6(a-d) are from the same experiment.

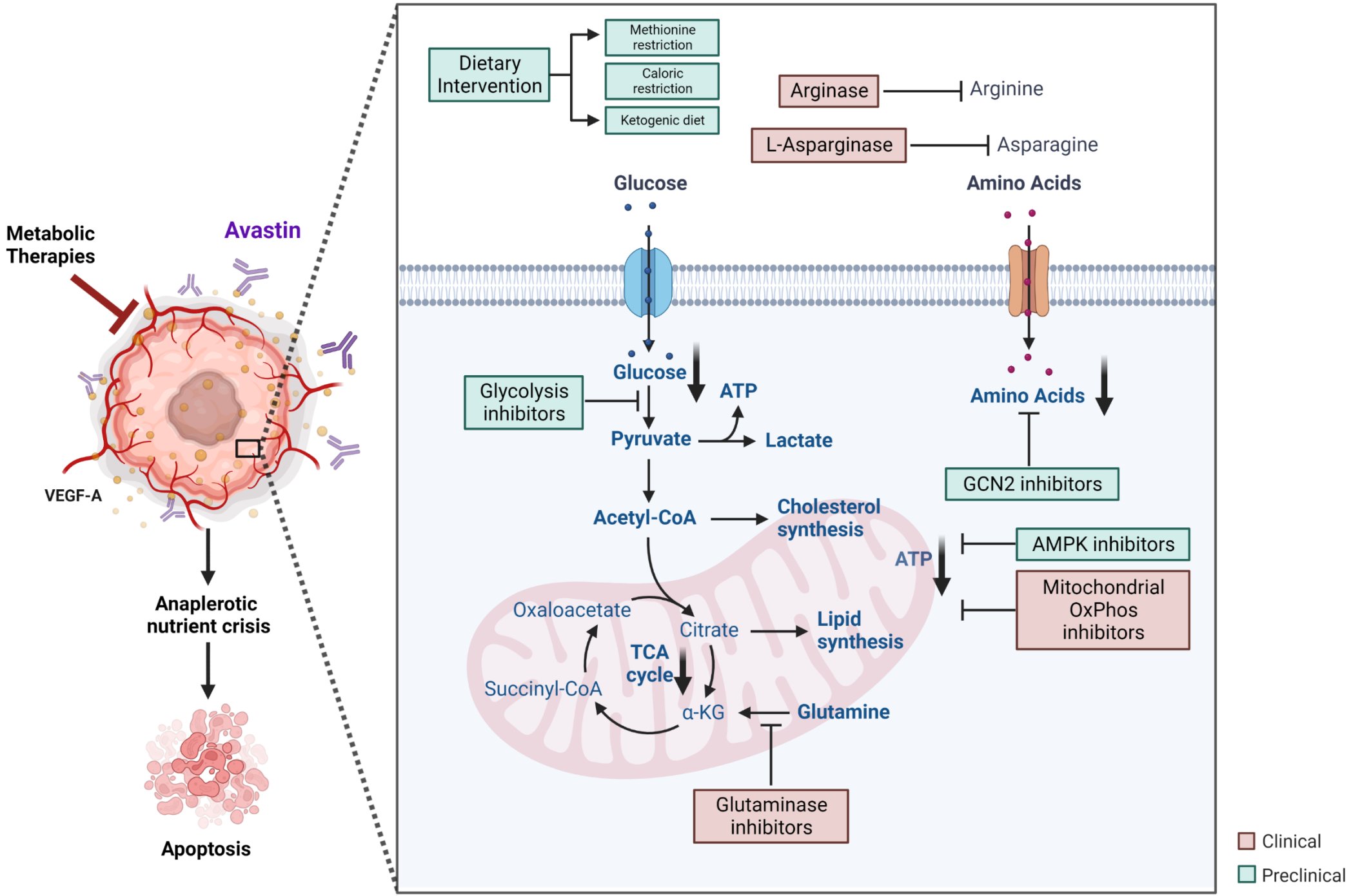
Metabolic Therapies
Avastin
VEGF-A
Anaplerotic nutrient crisis
Apoptosis
Dietary Intervention
Methionine restriction
Caloric restriction
Ketogenic diet
Arginase
Arginine
L-Asparginase
Asparagine
Glucose
Amino Acids
Glucose
ATP
Glycolysis inhibitors
Pyruvate
Lactate
Amino Acids
GCN2 inhibitors
Acetyl-CoA
Cholesterol synthesis
ATP
AMPK inhibitors
Mitochondrial OxPhos inhibitors
Oxaloacetate
Citrate
Lipid synthesis
TCA cycle
Succinyl-CoA
α-KG
Glutamine
Glutaminase inhibitors
Clinical
Preclinical

Figure 7: Potential of angiogenesis inhibitors as adjuvant/combination treatment with metabolic therapies in cancer. Illustration highlighting synergistic anti-tumor therapeutic potential of combining angiogenesis inhibitors with existing and emerging metabolic therapies that result in anaplerotic nutrient stress in cancer cells. Angiogenesis inhibitors such as Avastin impede the delivery of blood-borne nutrients such as glucose and amino acids to cancer, resulting in anaplerotic deficit, and expose a multitude of metabolic vulnerabilities in cancer cells. Such metabolic liabilities may be exploited further through inhibition of glycolysis (POMHEX/HEX), as well as amino acids availability/breakdown (L-asparginase, Arginase, CB-839), impairment of metabolic stress adaptation (GCN2 inhibitors, AMPK inhibitors, autophagy inhibitors), and integration of dietary interventions such as methionine restricted diet, caloric restriction, and ketogenic diet. Together, the combination of angiogenesis inhibition and metabolic therapies may accentuate anaplerotic nutrient crisis and yield a synergistic inhibition of cancer cell growth and proliferation.

Supplementary Figure 1

a

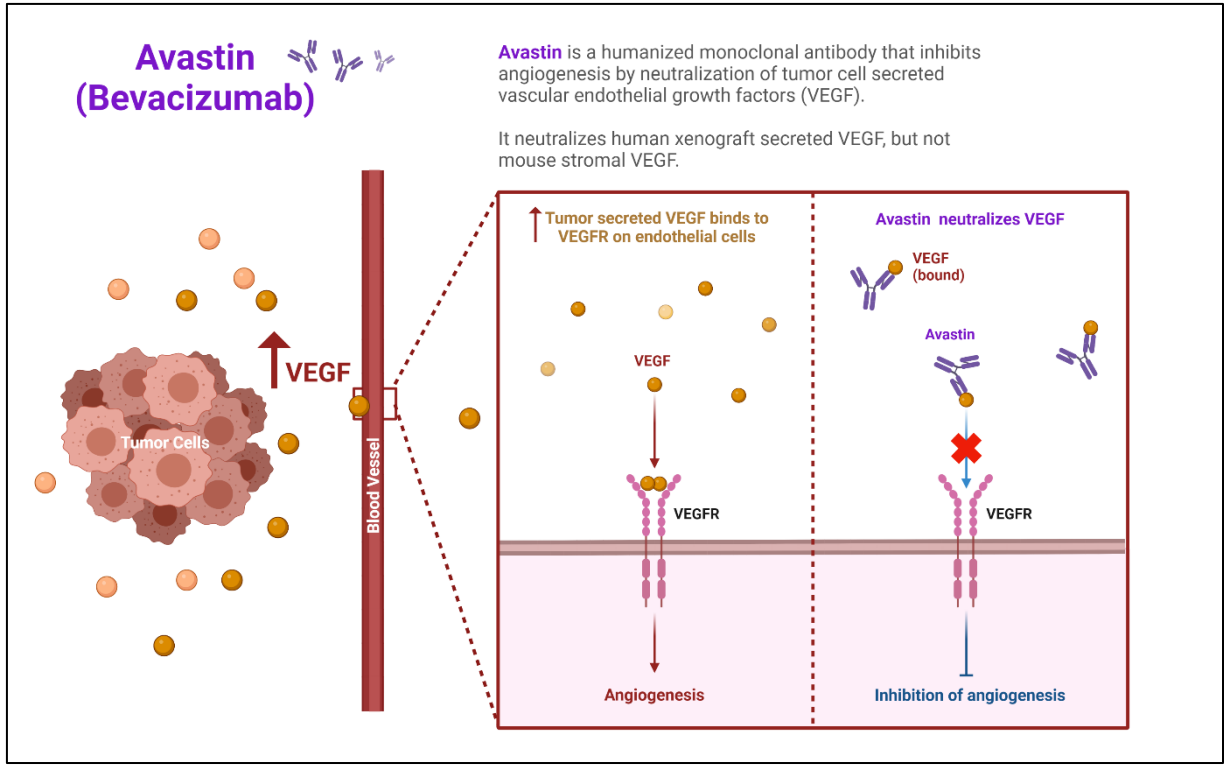

b

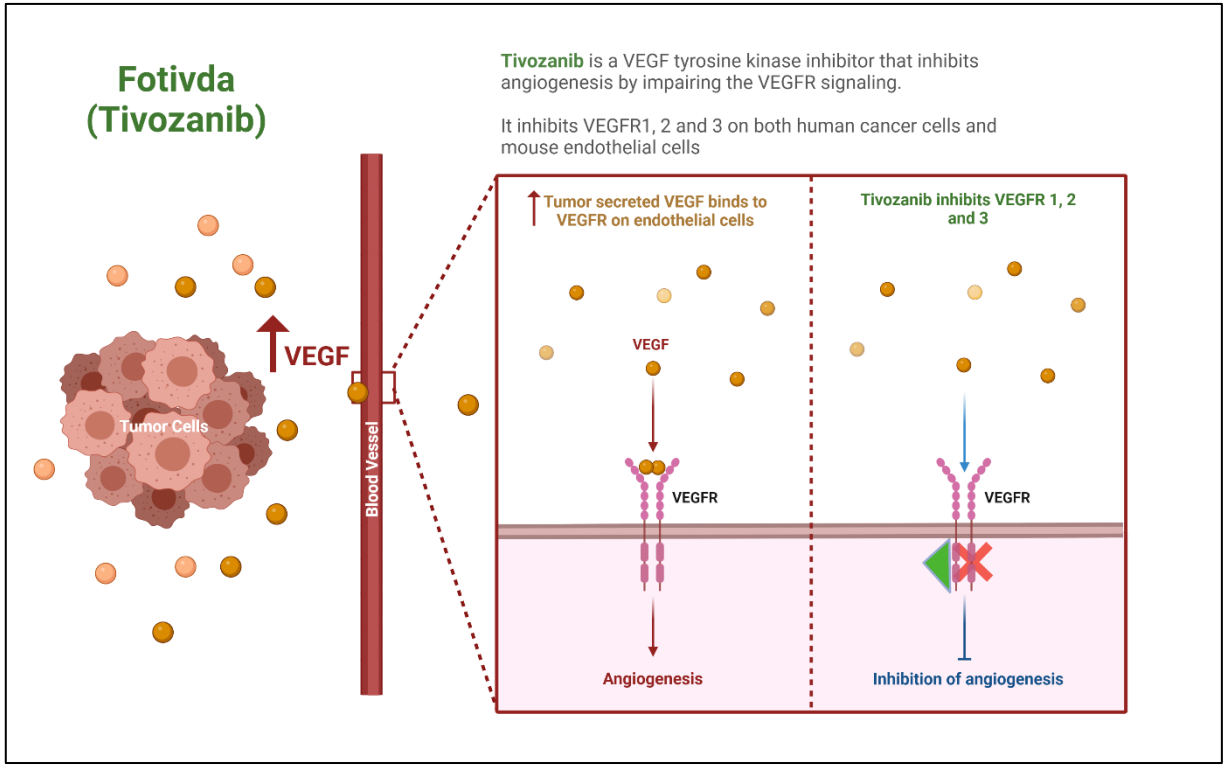

Supplementary Figure 1. **Angiogenesis inhibitors impair neo-vascularization by inhibition of the VEGFR signaling cascade. a.** Bevacizumab (Avastin) is a VEGF-A neutralizing humanized monoclonal antibody that neutralizes the VEGFA secreted by the tumor cells and impairs VEGFR signaling (Ferrara et al. 2004 *Nat Rev Drug Discov.*). Avastin is clinically approved as a frontline therapy for a broad range of malignancies that include glioblastoma multiforme, metastatic colorectal cancer, renal cell carcinoma, ovarian adenocarcinoma among many others. **b.** Tivozanib (Fotivda) is a specific inhibitor of VEGFR 1, 2 and 3 and it abrogates the VEGF signaling pathways through the inhibition of the tyrosine kinase activity of the VEGFRs (Nakamura et al. 2006 *Cancer Res.*).

Supplementary Figure 2

a

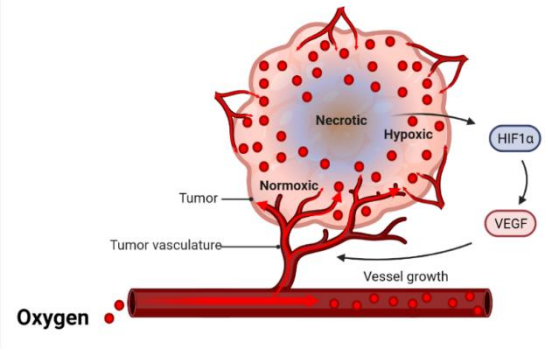

Oxygen delivery from blood to the tumors

b

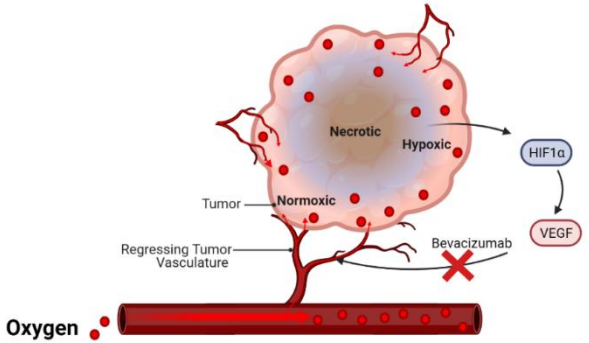

Diminished oxygen delivery after angiogenesis inhibition

c

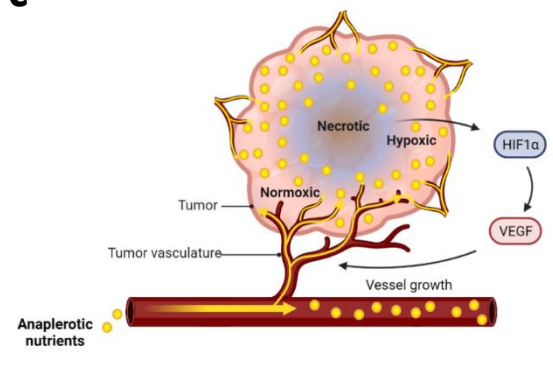

Nutrient delivery from blood to the tumors

d

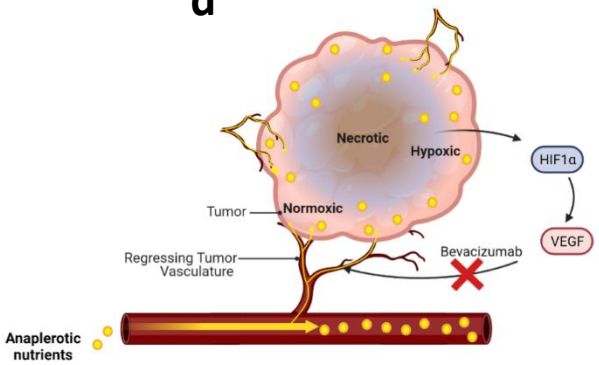

Diminished nutrient delivery after angiogenesis inhibition

e

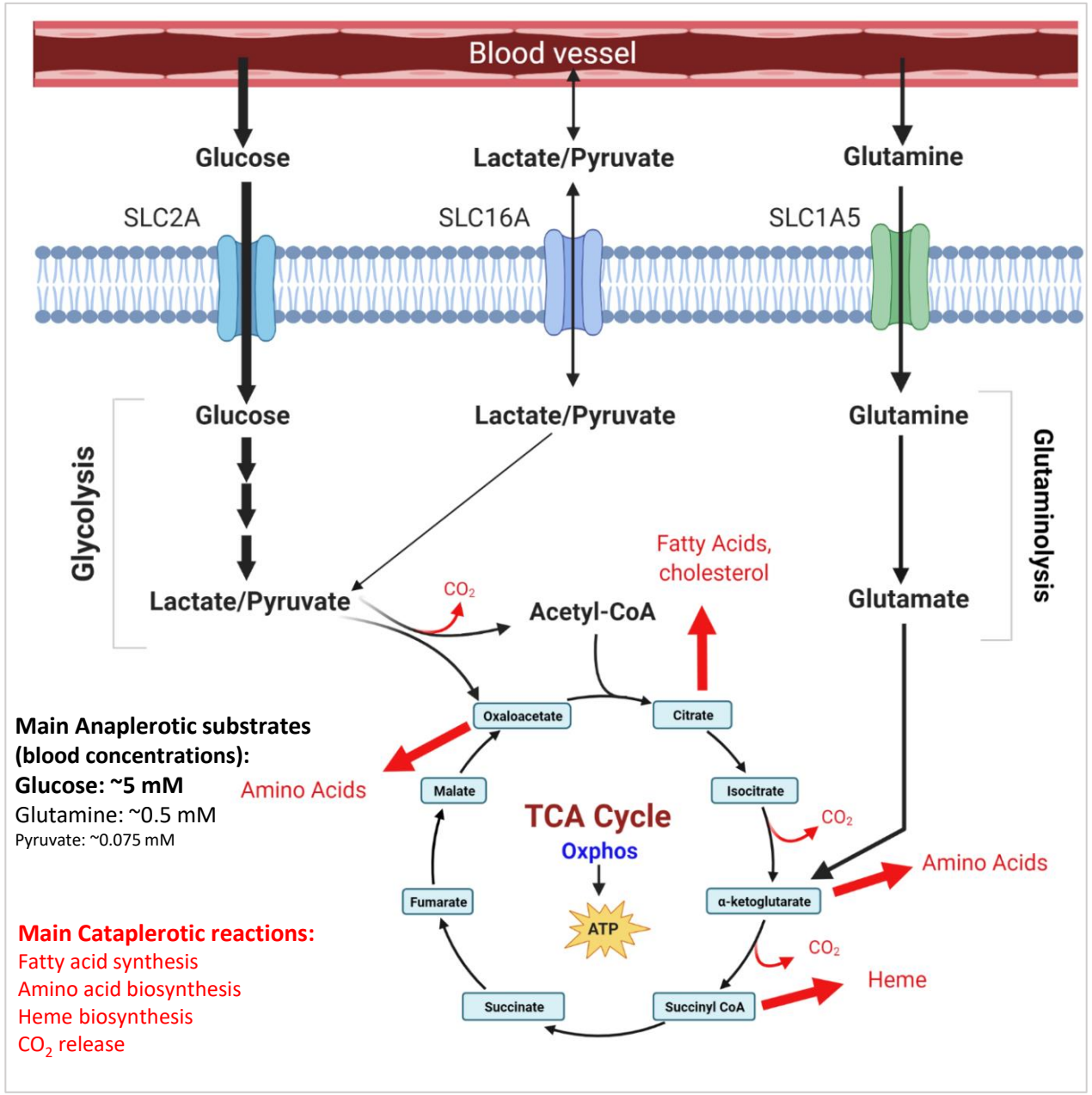

Supplementary Figure 2. **Angiogenesis inhibition impairs neovascularization in tumors, restricts tumor perfusion and delivery of oxygen and blood borne anaplerotic nutrients/Oxphos substrates. (a-d)** Schematic depicting the impact of tumor perfusion on oxygen and nutrient delivery to the tumors following angiogenesis inhibition. Angiogenesis ensures a continuous delivery of oxygen(**a-b**) and import of nutrients(**c-d**) to the tumor cells enabling metabolic processes that generate the biosynthetic and bioenergetic intermediates to support tumor survival and proliferation. Tumors employ multiple signaling pathways, most notably, HIF1α pathway, once they sense a hypoxic environment. One of the direct consequence of HIF1α activation is the secretion of vascular endothelial growth factors (VEGF) by the tumors. VEGFs act on the VEGF receptors (VEGFR) on endothelial cells, which orchestrates the angiogenesis cascade. Inhibition of angiogenesis has been an integral therapeutic approach in cancer. Multiple angiogenesis inhibitors have been developed and are currently in the clinic. **e.** Schematic depicting the consequence on the delivery of blood-borne nutrients to the tumors by angiogenesis inhibition. Apart from diminished oxygenation and elevation of hypoxia in the tumors, angiogenesis inhibition also restricts the import of blood-borne nutrients, that fuel the mitochondrial metabolic processes: the TCA cycle and oxidative phosphorylation. The TCA cycle is a bioenergetic engine and an anabolic hub in cancer cells. In addition to generating reducing equivalents for mitochondrial Oxphos reactions, TCA cycle also plays crucial role in anabolic reactions in cancer cells. The TCA cycle is constantly drained of carbon atoms in the form of CO_2 and when the metabolic intermediates exit the cycle, to generate biosynthetic intermediates (shown in red) to support cancer cell proliferation. To ensure a continuous function of the TCA cycle, the carbon atoms must be replenished back into the TCA cycle by a process called anaplerosis. Cancer cells consume copious amounts of blood borne nutrients such as glucose, glutamine, fatty acids etc, to provide the surplus carbon atoms for the TCA cycle and ensure uncontrolled growth and proliferation.

Supplementary Figure 3

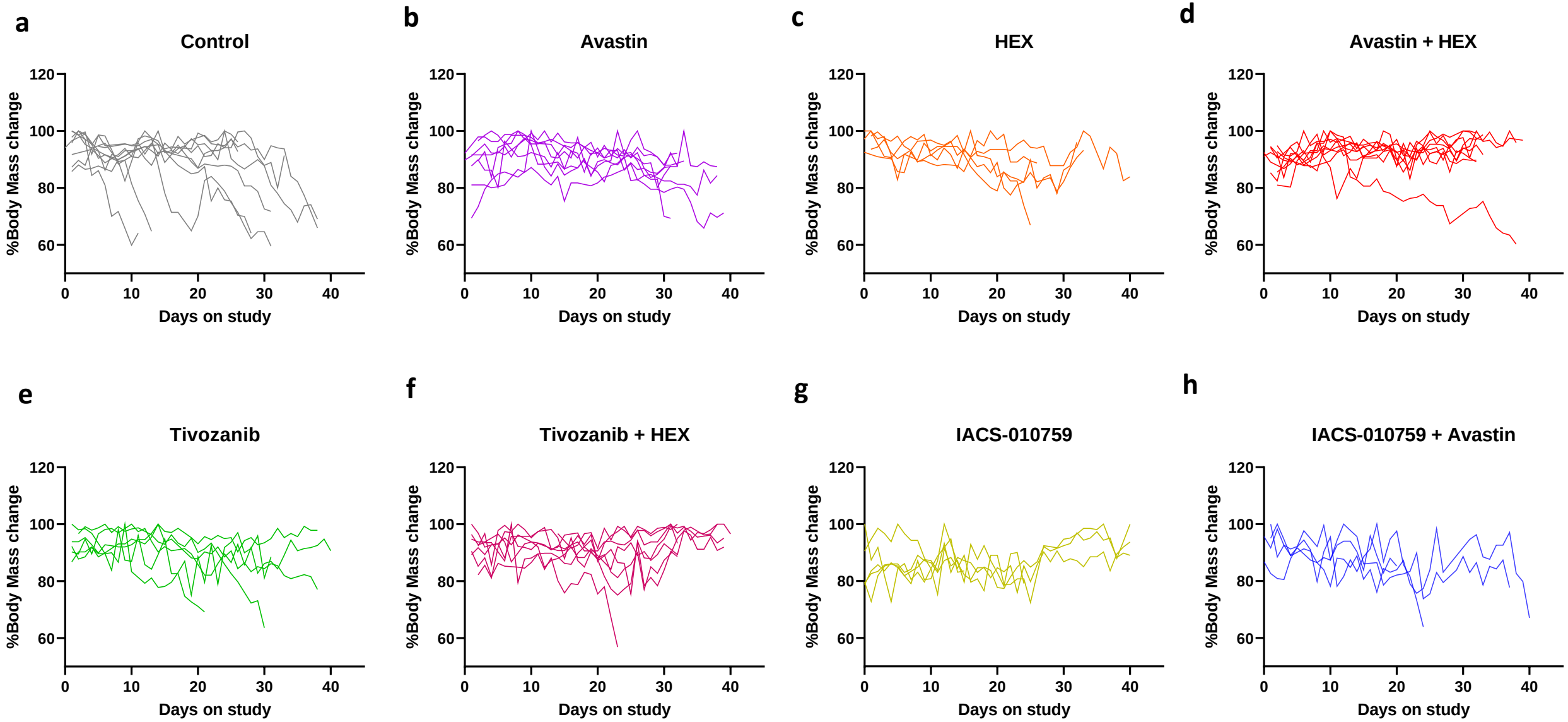

Supplemental Figure 3: **Inhibition of angiogenesis combined with anti-metabolic therapy is well-tolerated in-vivo. a-e.** Body weight is a useful proxy of disease burden in mice that is routinely monitored in toxicology experiments. Body weights of mice bearing ENO1-/- intracranial tumors subjected to Avastin, HEX, Tivozanib or IACS-10759 as monotherapy or to combination of HEX or IACS-10759 with Avastin or Tivozanib over 28 days. Combination therapy does not exhibit toxicity exaggeration in mice compared to the monotherapy and delayed the loss of body weight caused by brain tumor disease burden. The most significant decreases in body weights occurred in mice in the control group and it correlated with most aggressive intracranial tumor growth. Body weights of individual mice show a negative correlation with tumor burden with loss of body weights strongly associated with rapid tumor growth.

Supplementary Figure 4

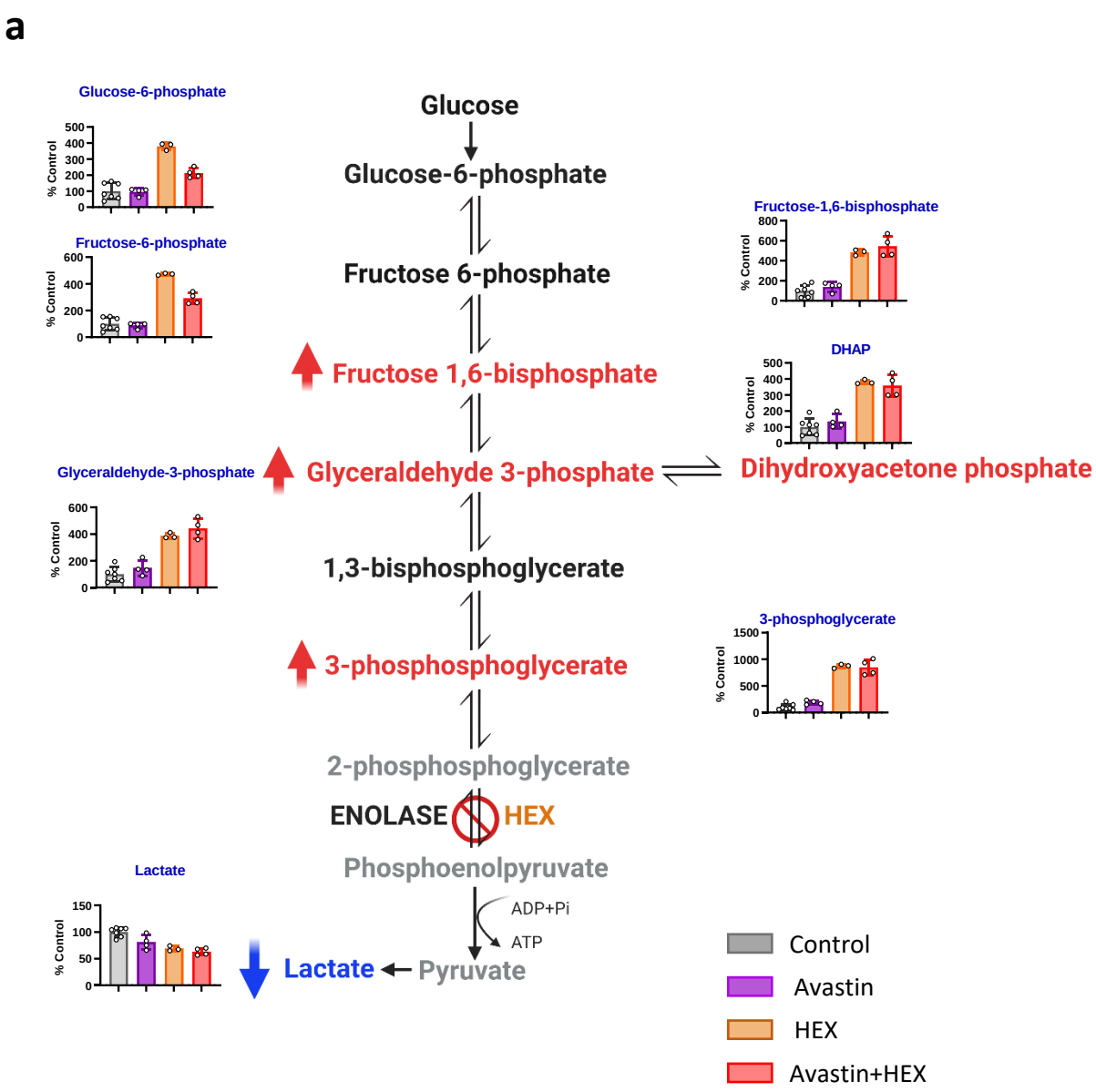

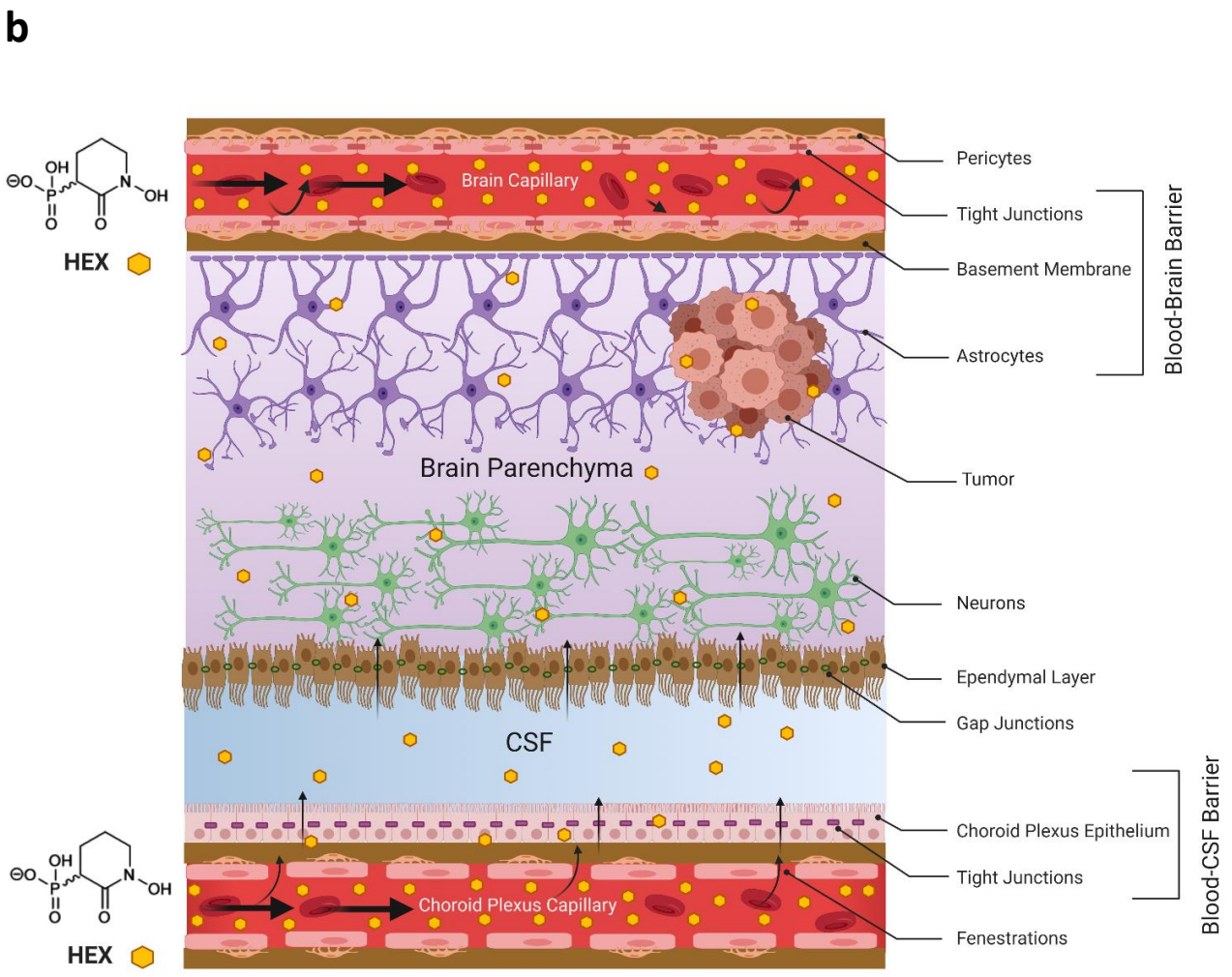

Supplemental Figure 4 : **Avastin treatment does not modulate inhibition of glycolytic flux by the enolase inhibitor HEX. a.** Inhibition of glycolysis by HEX is independent of Avastin mediated BBB resealing. HEX treatment, in HEX alone or Avastin + HEX treated tumors result in a comparable accumulation of glycolytic intermediates upstream of the enolase reaction. This indicates that despite the resealing of the blood brain barrier by Avastin treatment, HEX can still enter the brain and exert its effects. **b.** Small water-soluble phosphonate drug can reach the brain through the blood cerebrospinal fluid (CSF) barrier. Water-soluble phosphonate substrates such as HEX cannot cross the highly selective blood brain barrier (BBB). An alternative route for entry to the brain is through the blood CSF barrier. Unlike the BBB, the capillaries in the blood CSF barrier have fenestrations, which enable penetration of soluble drugs with small molecular weights, such as the antibiotic fosfomycin, which is clinically used to target brain abscesses. When Avastin treatment reseals the leaky tumor vasculature, HEX possibly enters the brain through the blood CSF barrier and exerts its anti-neoplastic effect (Lin *et al* 2020 *Nat Metab*, and Khadka *et al* 2020 *Cancer and Metab*)

Supplementary Figure 5

D423 (*ENO1*-deleted tumors)

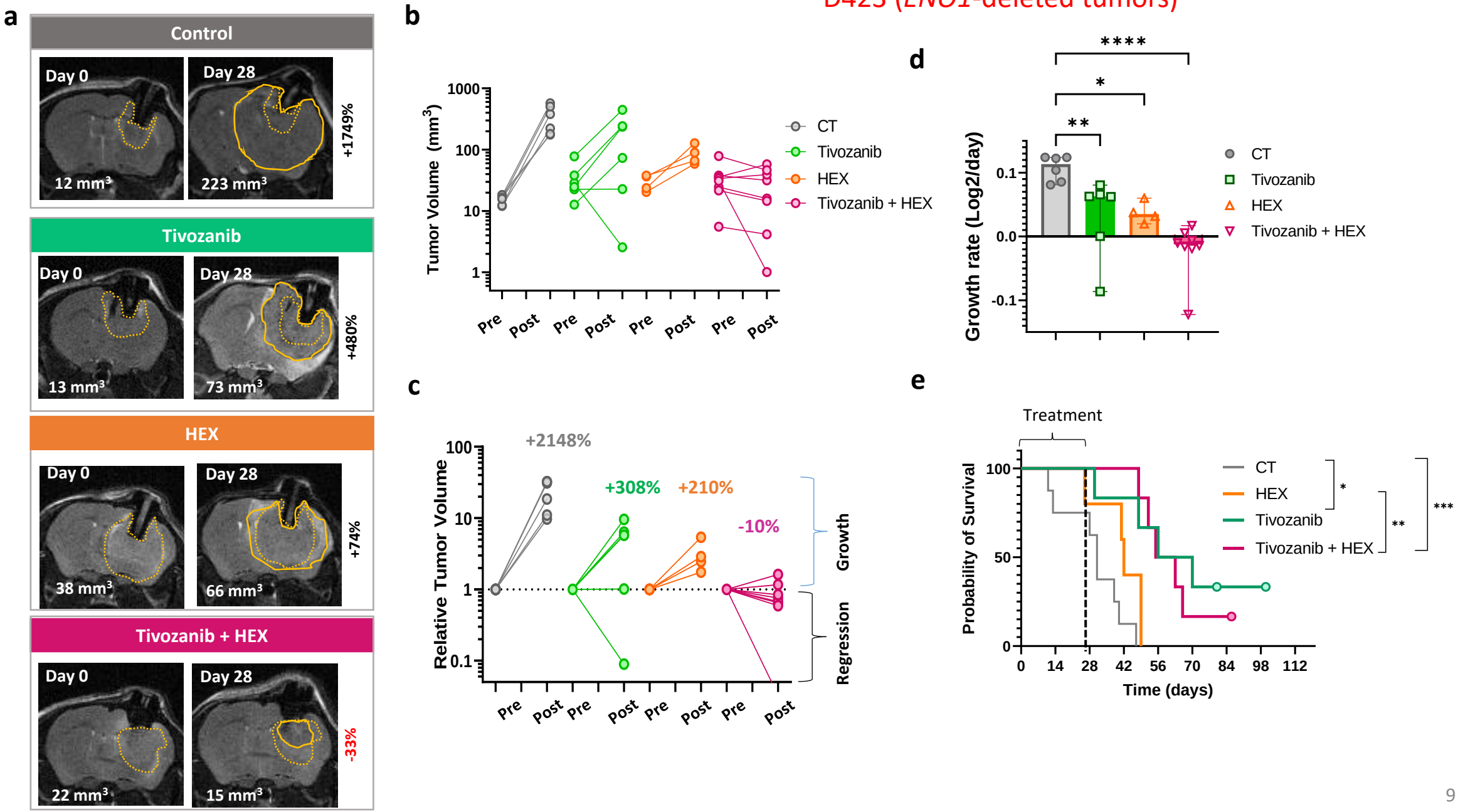

Supplemental Figure 5: **Combination of the enolase inhibitor HEX and VEGFR1/2/3 inhibitor Tivozanib all but eliminates intracranial tumor growth.** Intracranial tumors were generated in Foxn1 $^{nu/nu}$ nude mice by implantation of D423 *ENO1*-homozygously deleted glioma cells and tumor growth was followed every week by T2-weighted MRI. When tumors were approximately 20 mm^3 in volume, mice were separated into four groups: Control (n=6), Tivozanib (n=7), HEX (n=4), Tivozanib + HEX (n=8) and treatments with Tivozanib (2.5 mpk, 7X per week), Enolase inhibitor HEX (225 mpk, 14 doses per week) or Tivozanib plus HEX (Tivozanib, 2.5mpk 7X per week + 225 mpk SC 14X per week) were administered for 28 days. **a.** MRI images with tumor outlines before (dotted yellow) and after (solid yellow) 28 days of treatment. **b-d.** Treatment with Tivozanib as single agent, led to a modest inhibition of tumor growth in most mice, but in two mice, it completely eradicated the tumors. HEX as single agent attenuated tumor growth but did not result in an overall tumor regression. However, the combination of Tivozanib and HEX resulted in tumor regression in all treated animals. Animals were taken off the treatments on day 28 and survival in each group was calculated. Tivozanib as single agent as well as Tivozanib and HEX combination caused a significant extension of survival compared to control and HEX.

Supplementary Figure 6

a

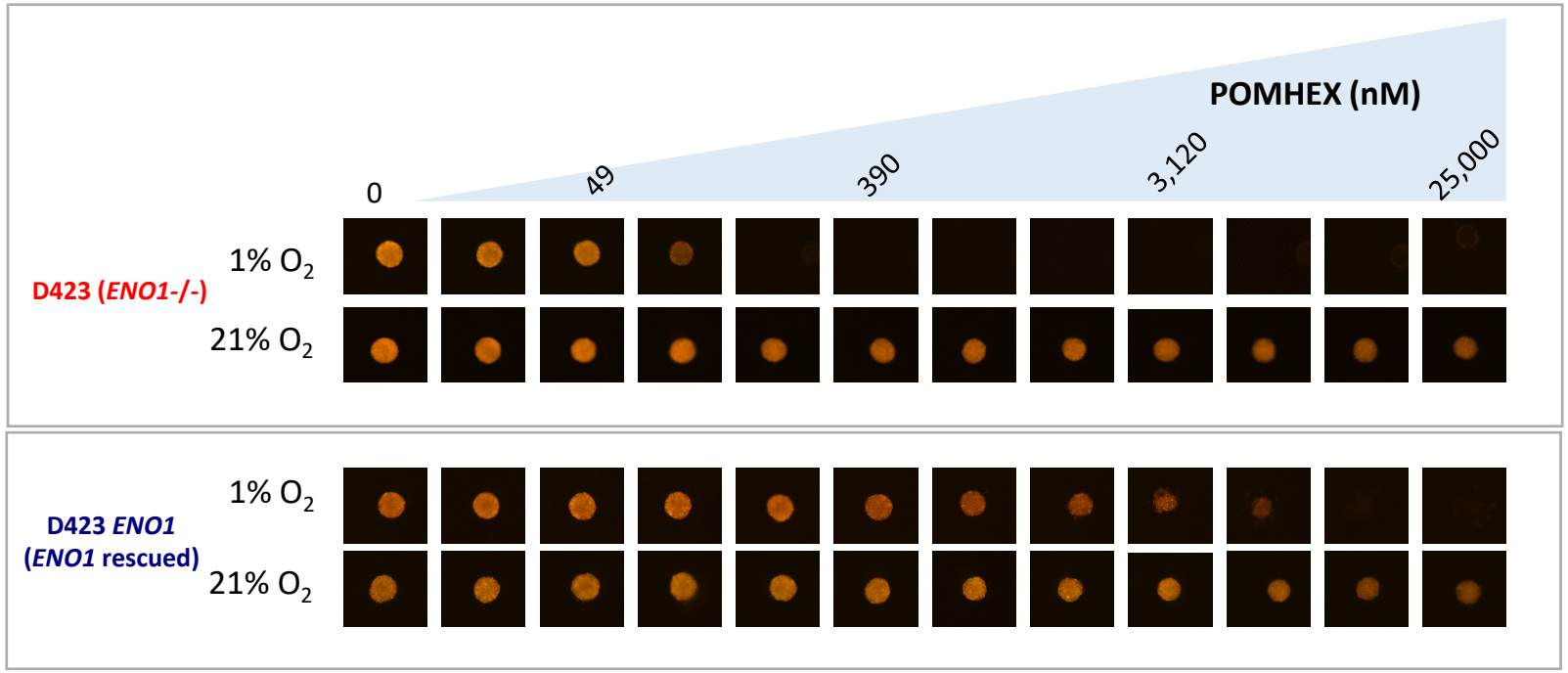

b

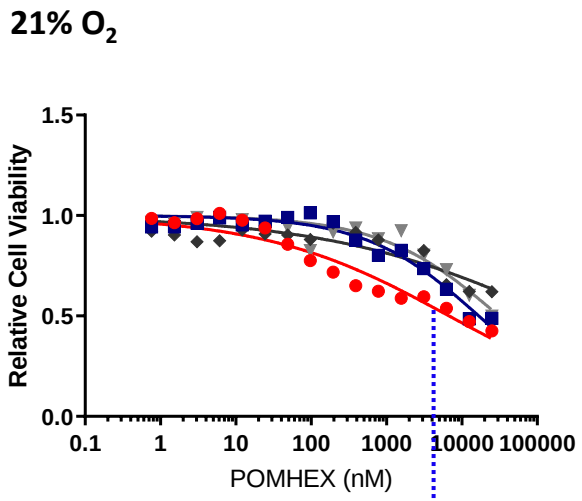

c

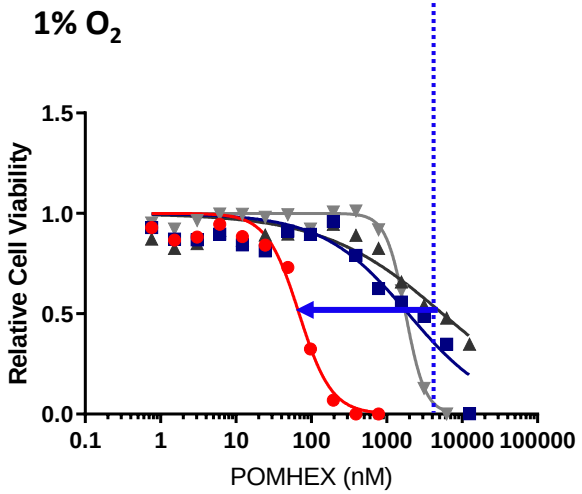

d

Cells	IC_{50} (nM) 1% O_2	IC_{50} (nM) 21% O_2
D423 (ENO1-/-)	68.1	6,759
D423 (ENO1 rescued)	1,931	16,753
U373 (ENO1 +/+)	5,492	173,606
LN319 (ENO1 +/+)	1,779	31,509

Supplemental Figure 6**: Potency of the Enolase inhibitor is dramatically enhanced under hypoxic conditions in 3D spheroids *in vitro*** Tumor spheres of D423 *ENO1*-deleted (red), D423 *ENO1*-rescued (blue), as well as *ENO1*-intact, U373 (dark grey) and LN319 (grey) cells were treated with POMHEX at the concentrations indicated, for 2 days in either a hypoxic incubator (1% O_2) or under 21% O_2 hypoxia. Viable cells were imaged by Tetramethylrhodamine (TMRE, red fluorescence) staining, which was quantified and expressed relative to the vehicle control. **a**. Representative images of *ENO1*-deleted (top panel) and *ENO1*-rescued tumor spheres (bottom panel) at normoxia or 1% hypoxia after 2 days of treatment with POMHEX at the concentrations indicated. **b-c.** Quantification of cell viability by TMRE intensity as a function of POMHEX concentration after two days of treatment under normoxia (**b**) or 1% hypoxia (**c**) for *ENO1*-deleted, *ENO1*-rescued and *ENO1*-WT lines treated with POMHEX. The dotted vertical line is for IC_{50} comparison, and the arrow indicates the shift in IC_{50} between hypoxic and normoxic conditions. **d.** Table indicating the $\mathbf{IC_{50}}$ of each cell line under normoxic and 1% hypoxic conditions. The potency of the Enolase inhibitor POMHEX for killing D423 *ENO1*-deleted glioma cells is dramatically increased in 1% O_2 as compared to in normoxia; hypoxia similarly increases potency of POMHEX against *ENO1*-rescued and *ENO1*-WT glioma cell lines.

Supplementary Figure 7

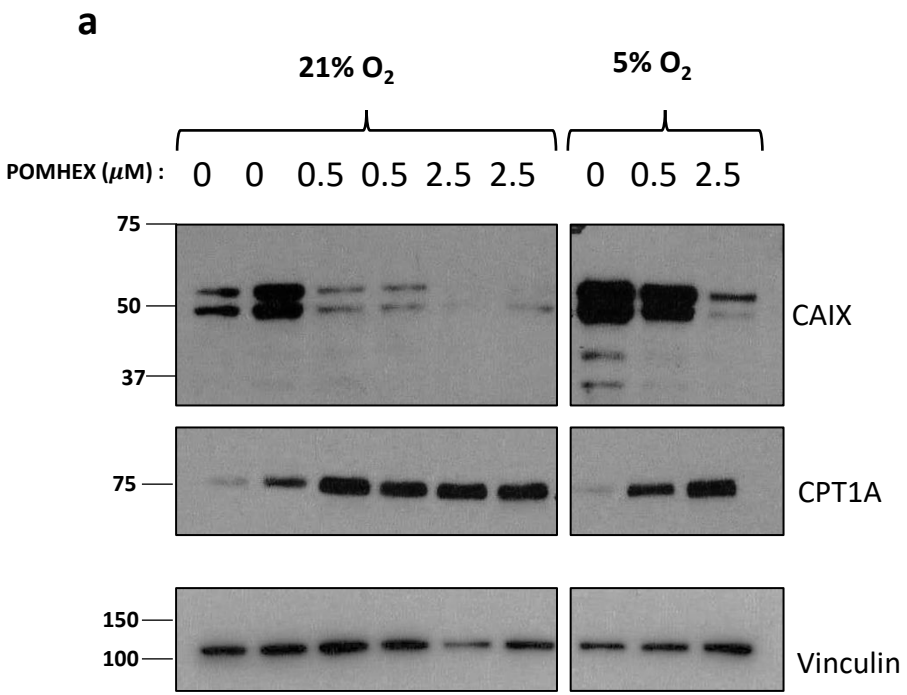

Supplemental Figure 7**: Enolase inhibitor treatment decreases hypoxia by diminishing oxygen consumption.** Enolase inhibitor POMHEX inhibits glycolysis and prevents pyruvate production, a key mitochondrial oxidative phosphorylation (oxygen consuming) substrate. Cells were treated different doses of POMHEX in normoxic and hypoxic conditions and different hypoxia responsive genes were assessed by western blot. **a.** Treatment with the Enolase inhibitor decreases carbonic anhydrase-9, a HIF1α target in both normoxic and hypoxic conditions in a dose dependent manner but increases carnitine palmitoyl-transferase CPT1A levels.

Supplementary Figure 8

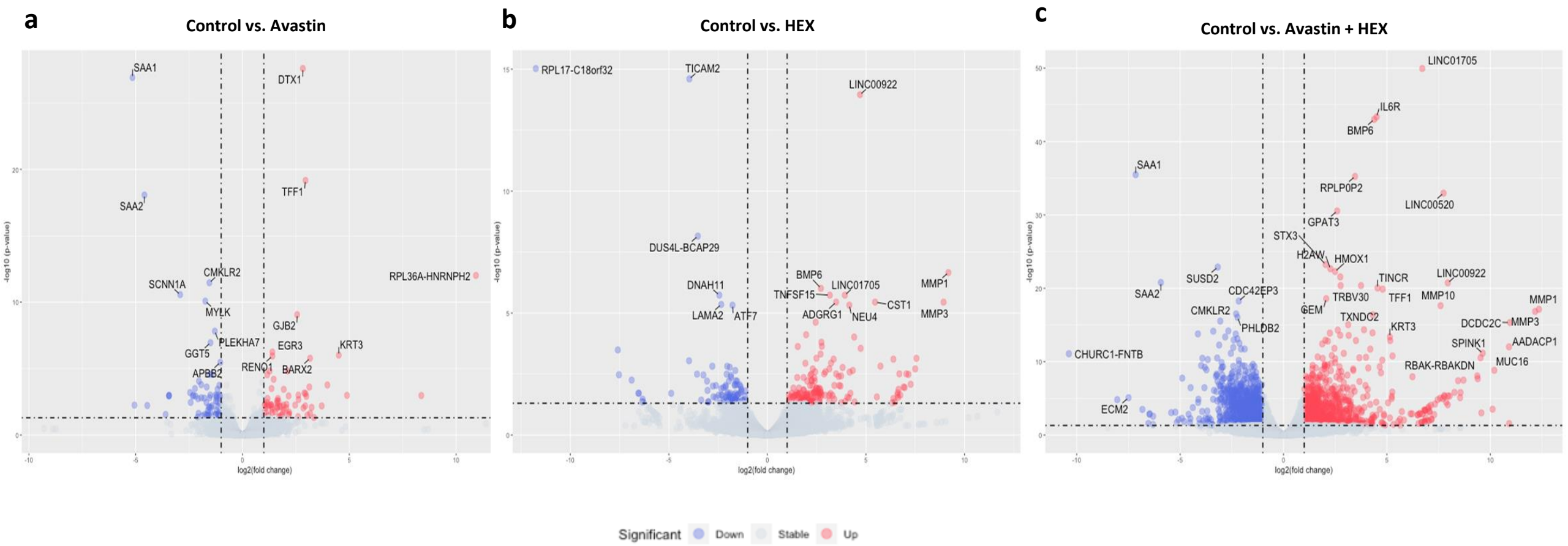

Supplemental Figure 8: **Combination of Avastin and HEX causes synergistic changes in differential gene expression in intracranial tumors**. (**a-c**) Volcano plots representing differentially up-regulated or down-regulated genes in monotherapy of Avastin or HEX, and combination treatment with Avastin and HEX compared to control. Statistically significant up- (red)or down-(blue)regulated genes (Up: $\log2Fc \geq 1$ and $padj \leq 0.05$; Down: $\log2Fc \leq -1$ and $padj \leq 0.05$) are shown in red and blue circles respectively, with gene names highlighted.

Supplementary Figure 9

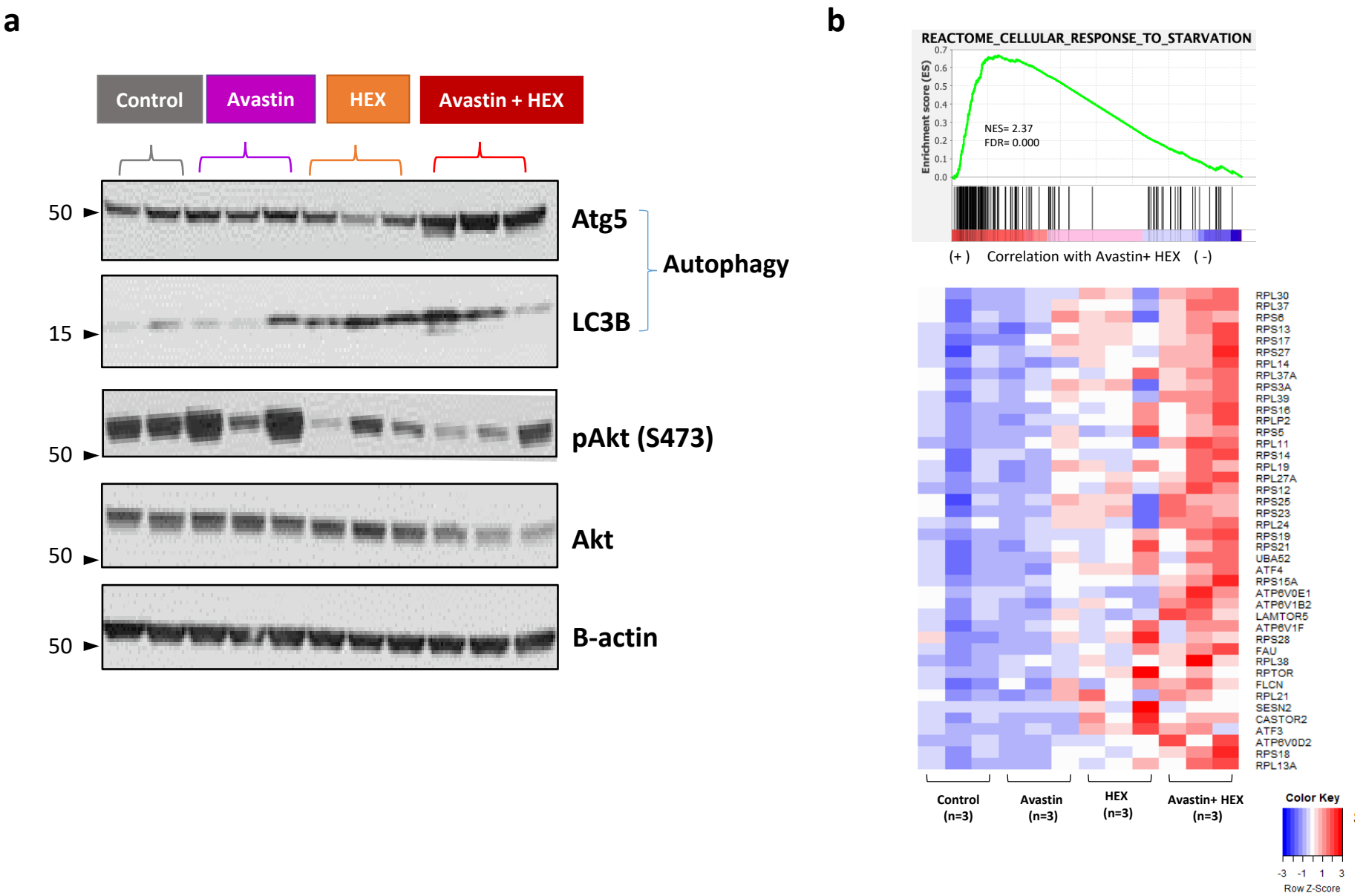

Supplemental Figure 9 : **Combination of angiogenesis and glycolysis inhibition accentuate nutrient stress and adaptation response in tumors**. **a.** Lysates from intracranial tumors from control, Avastin, HEX, and Avastin + HEX treatment groups were immunoblotted for proteins such as Atg5 and LC3B involved in autophagy mediated stress adaptation response, and Akt, a crucial protein at the intersection of many interconnected signaling pathways that control cell survival and growth, apoptosis, as well as cellular metabolism. Combination treatment of Avastin and HEX significantly accentuates autophagic response which is evidenced by increase in Atg5 as well as LC3B compared to monotherapy of HEX or Avastin, and also suppress Akt signaling, by reducing levels of Akt protein as well as its phosphorylation. **b**. GSEA plots showing positive enrichment of genes in the reactome cellular response to starvation gene set in Avastin + HEX group compared to control (**Also shown in Figure 4i**). **c.** The leading-edge genes for all four treatment groups are shown in the heatmap.

Supplementary Figure 10

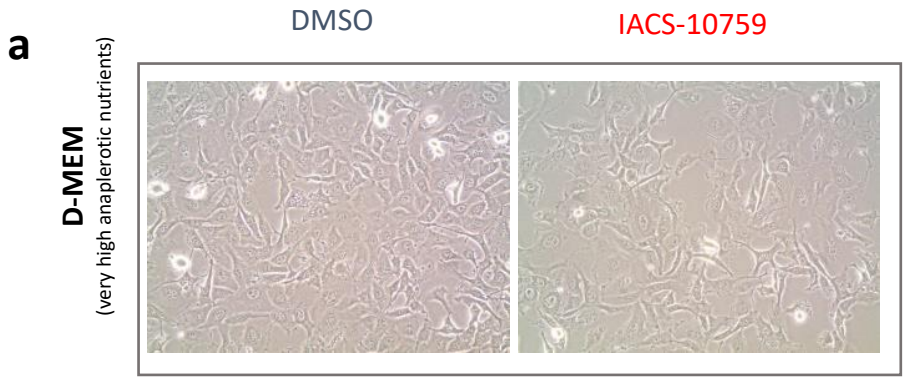

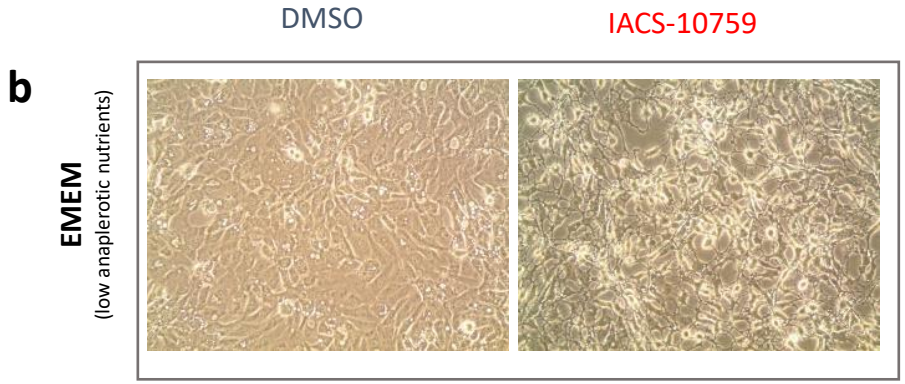

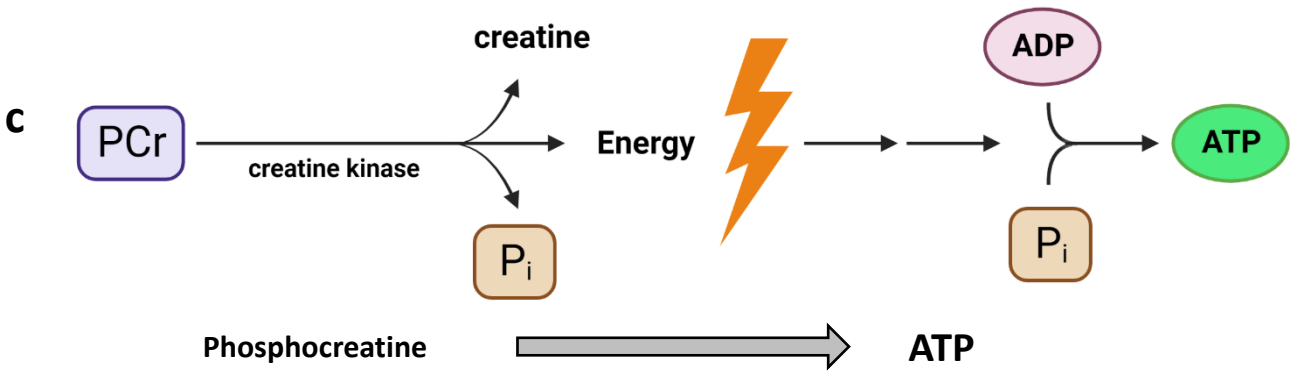

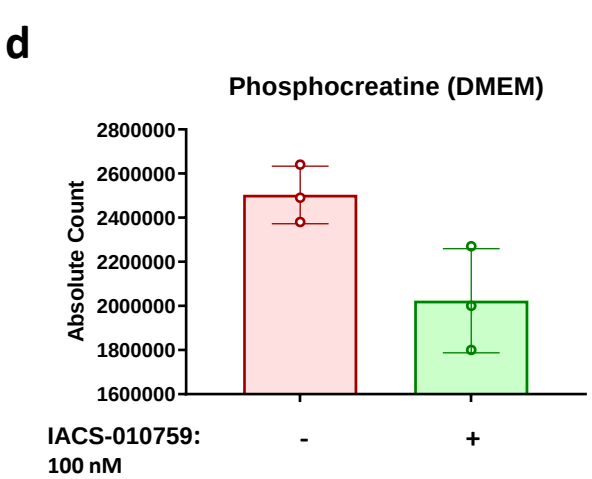

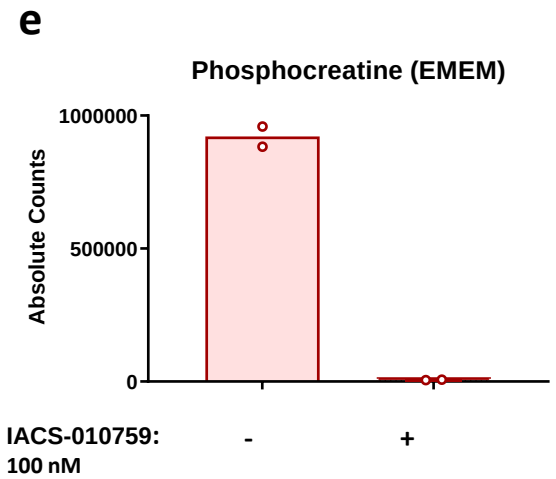

Supplemental Figure 10**: Inhibition of oxidative phosphorylation induces anaplerotic stress, resulting in an exaggerated bioenergetic collapse in nutrient deficient conditions. a-b**. *ENO1* deleted D423 cells treated with IACS-10759 in nutrient replete (**a**) and nutrient depleted conditions (**b**) show that the toxicity of IACS-010759 is exaggerated in low nutrient conditions. **c-e.** Phospho-creatine level, an indicator of bioenergetic state of cells (**c**), reveal a profound disruption of bioenergetics by IACS-010759 treatment in nutrient deficient conditions (**e**) compared to nutrient rich condition (**d**).

Supplementary Figure 11A

a

10/22/2019 11/12/2019 11/27/2019

Day 0 Day 20 Day 35

10759 5 mpk

Tivozanib 1 mpk
10759 5 mpk

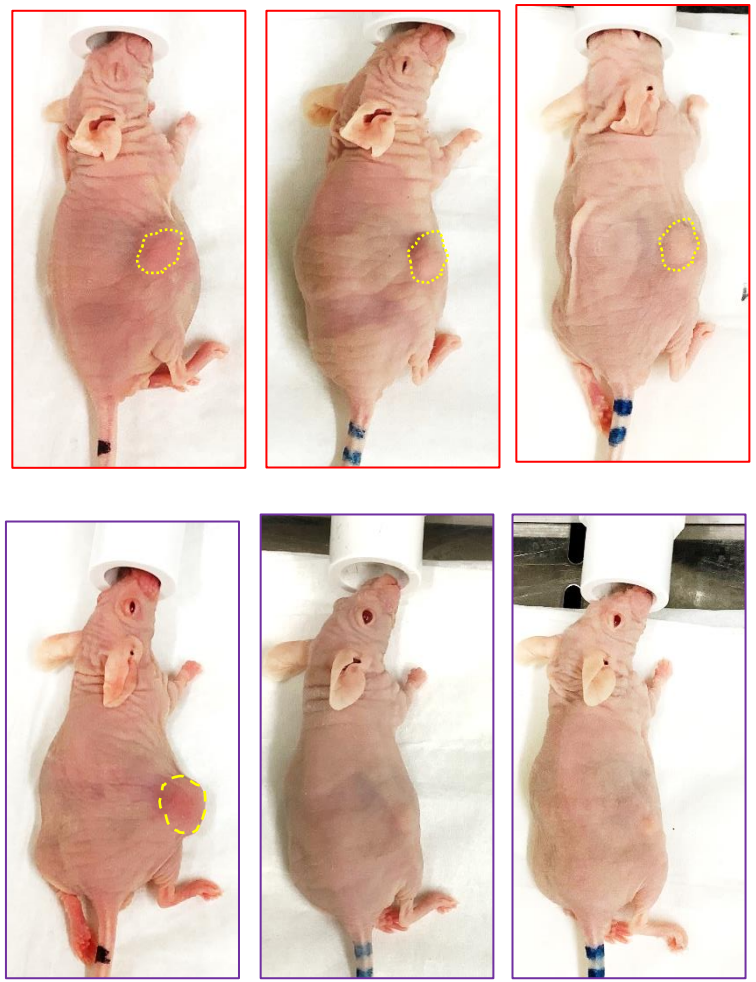

b

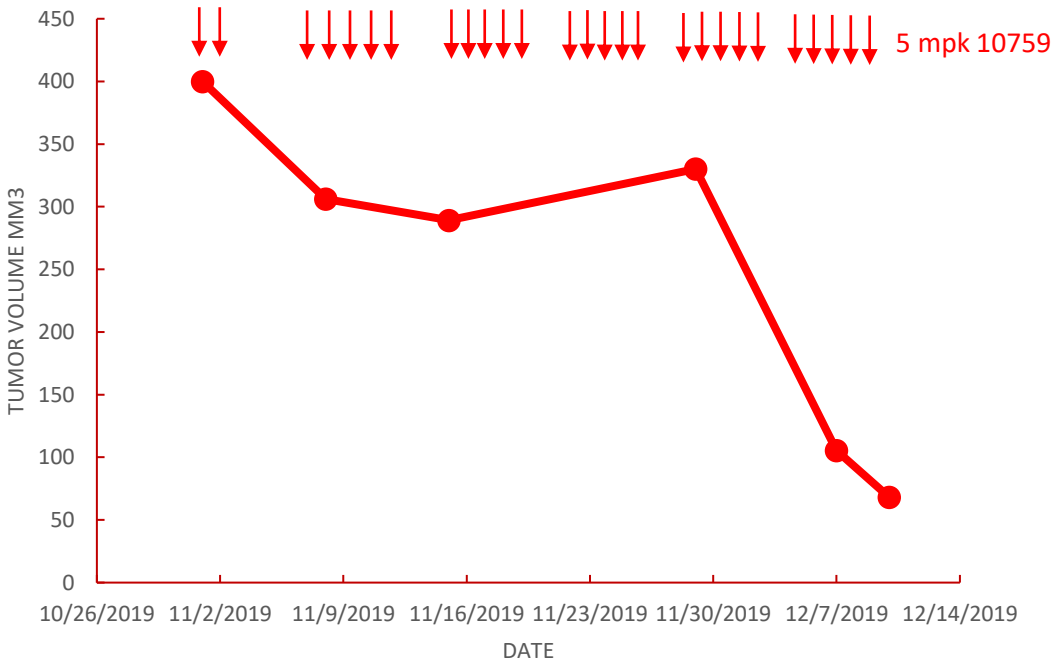

c

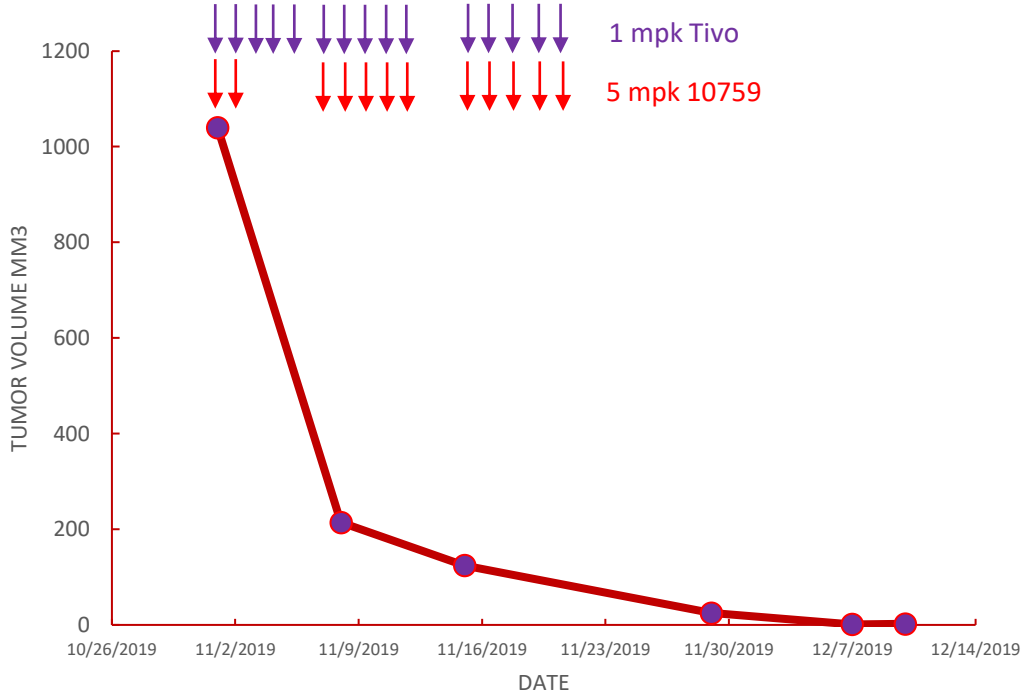

Supplementary Figure 11B

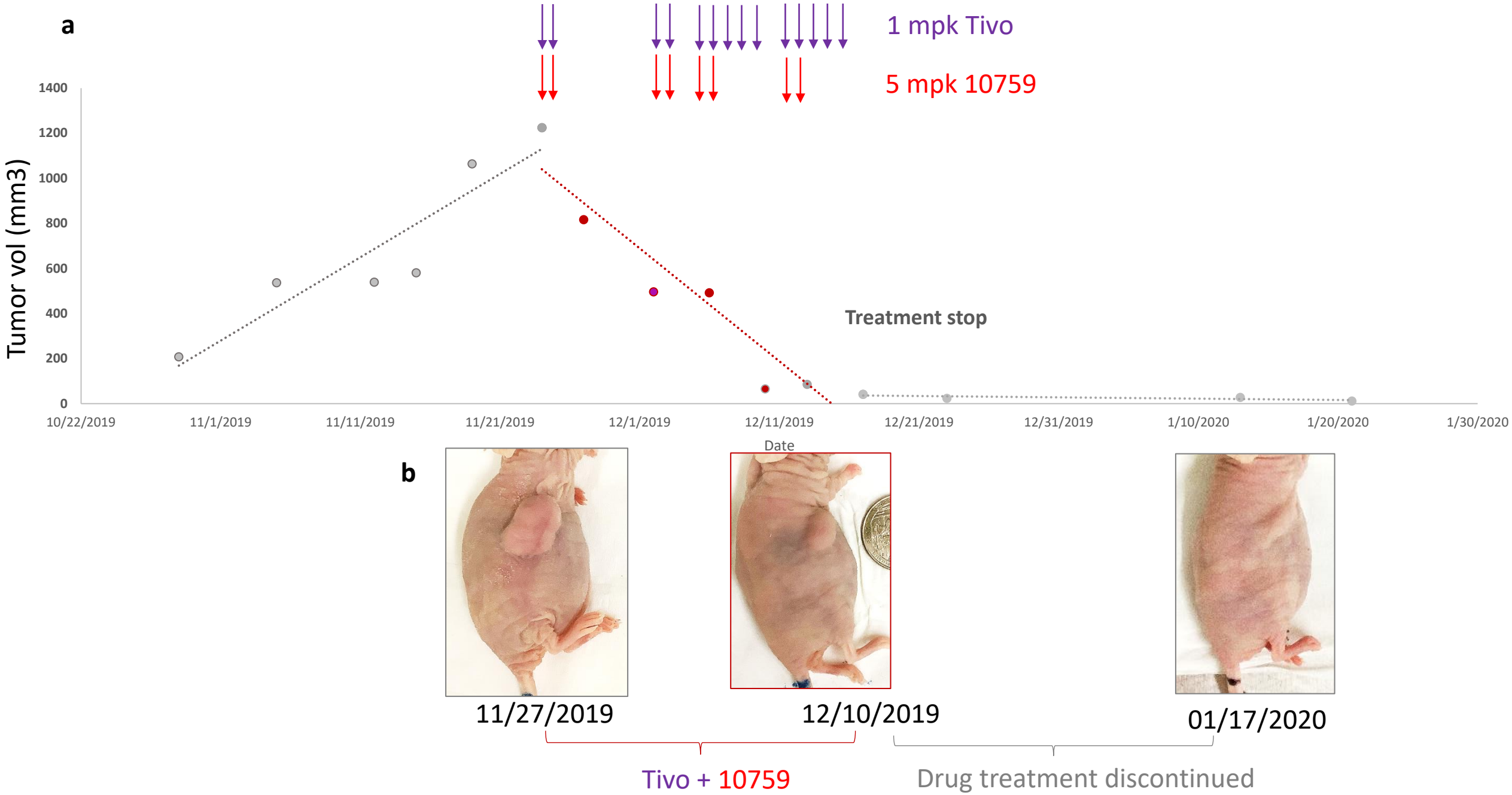

Supplemental Figure 11A and B**: Angiogenesis inhibitor and IACS-010759 drive exceptionally rapid regression even in very large sub-cutaneous tumors.** *PGD*-homozygously deleted NB1 cells were implanted sub-cutaneous in immunodeficient Foxn1 Nude mice. **12A a-c.** When tumors reached large volumes (>400 mm^3) mice were treated with either IACS-010759 alone (each dose indicated by a red arrow) alone or with IACS-010759 plus Tivozanib (each dose indicated by a purple arrow). Tivozanib as a monotherapy decreased tumor growth while IACS-010759 abolished tumor growth and as reported previously – drove tumor regression slowly over the course of weeks of continuous treatment. However – the co-administration of IACS-010759 with Tivozanib led to massive regression (>75% reduction in volume) in only 5 days. **12B a-b.** Given the poor tolerability of IACS-010759 in the clinic; dose-reduction attempts were made here: it was found that only two doses of IACS-010759 per week along with 5 doses of Tivozanib were sufficient to drive complete tumor regression with tumors remaining dormant for extended time after treatment discontinuation. Further experiments were discontinued due to COVID19 shut-downs.

Supplementary Figure 12

U87 (*ENO1* WT tumors)

a

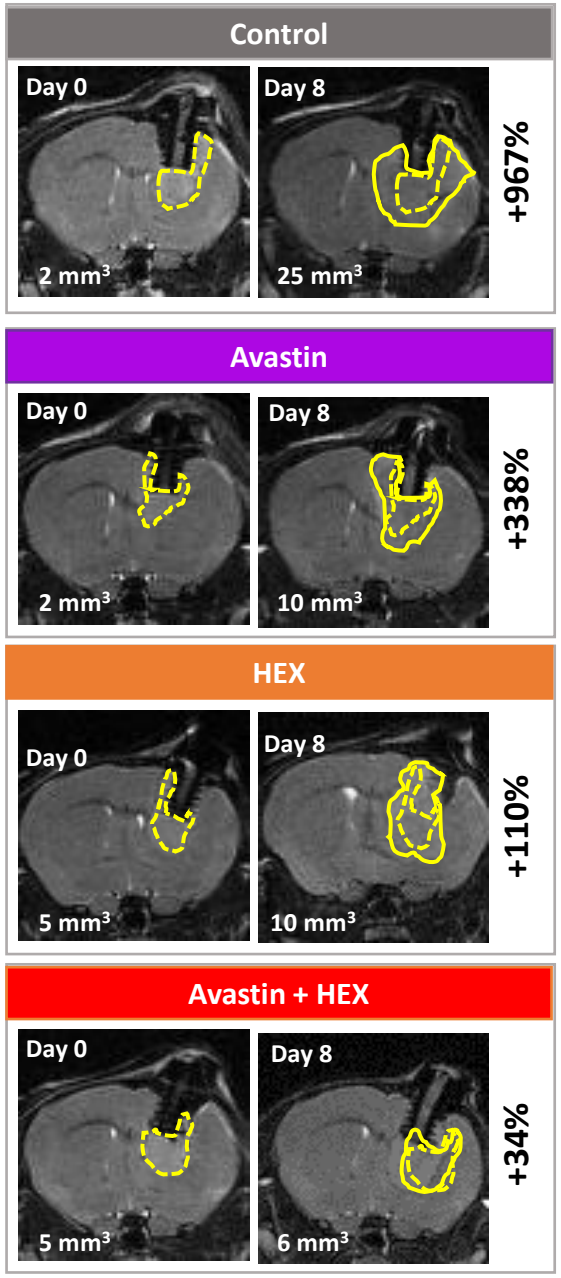

b

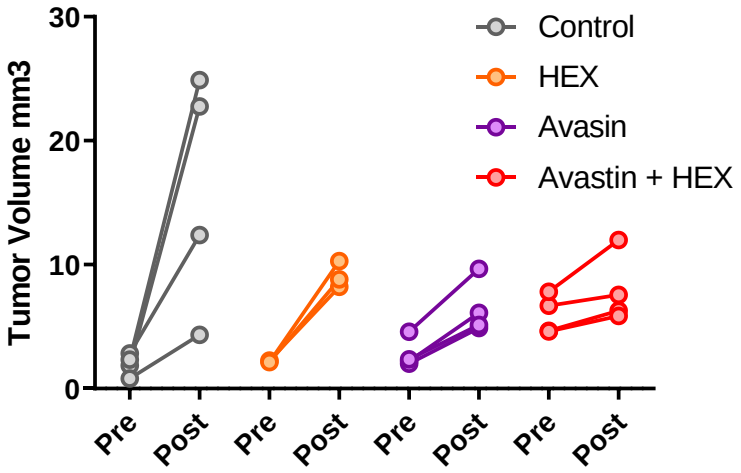

c

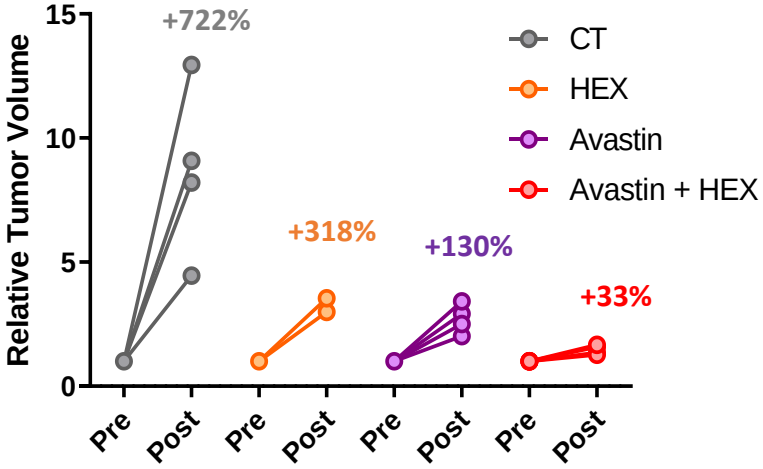

d

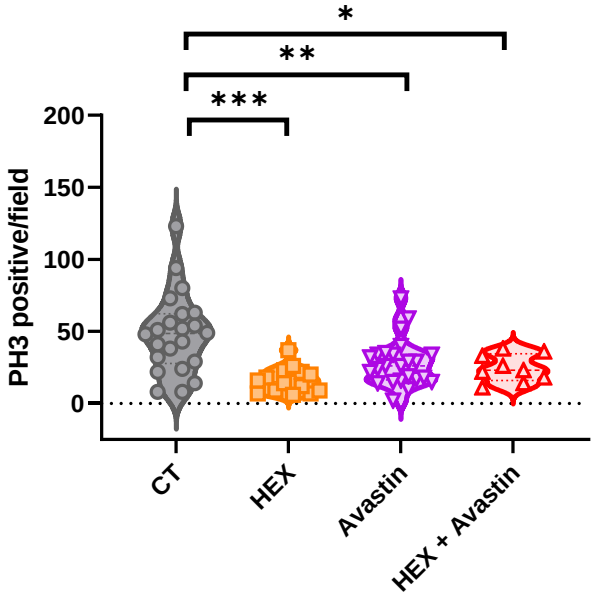

e

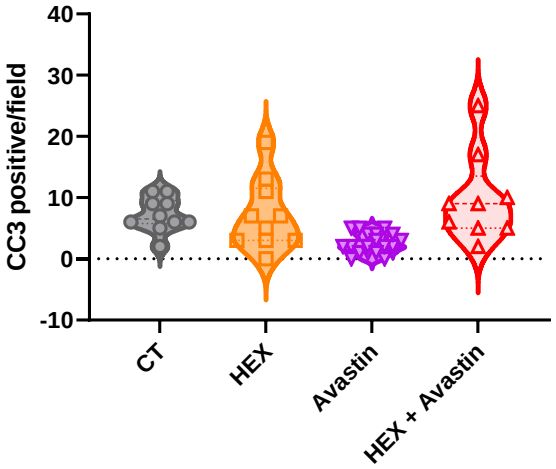

Supplemental Figure 12: **Angiogenesis inhibitor and enolase inhibitor display synergistic activity against non-glycolysis-compromised tumors** Intracranial tumors were generated by implanting U87 *ENO1* intact glioma cells in NSG immunocompromised mice. Tumor development was followed by T2-MRI. Treatment was begun when tumors reached ~2 mm3. **a.** T2-weighted MRI images of animals before and after 8 days of treatment with tumor volumes indicated in mm^3 in the lower part of the image; initial tumor outlines are shown in dotted yellow lines, while tumors after 8 days are shown in solid lines. **b-c.** Summary of tumor volume changes after 8 days on treatment. Animals were treated continuously with a high dose of HEX, once daily for 8 days, while Avastin was administered at 200 mg/kg 3 X in 8 days. The effect of HEX in ENO1-WT gliomas is only marginal, but Avastin treatment led to a modest inhibition of tumor growth. Combination of HEX and Avastin result in a near-all suppression of tumor growth. **d-e.** Histopathological analyses brain sections extracted from mice showed a significant reduction in (phospho-histone H3 positive, an index of proliferation) in tumors treated with the combination of HEX, Avastin and Avastin and HEX, and an increase in dying cells (cleaved caspase 3 positive cells, an index of apoptotic cells), in Avastin and HEX treated tumors.

Supplementary Figure 13

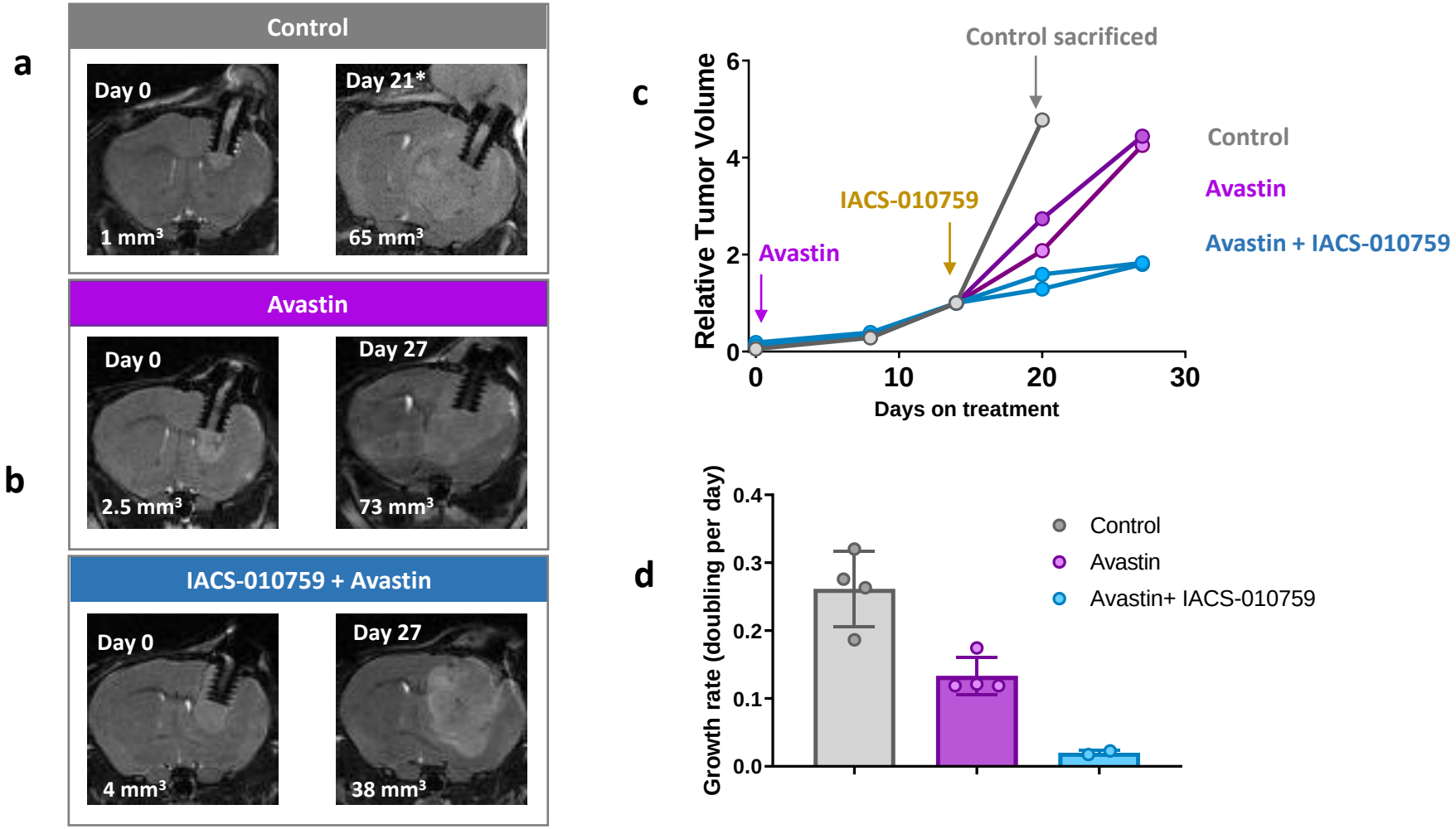

Supplemental Figure 13**: Angiogenesis inhibitor and IACS-010759 display synergistic activity against non-glycolysis-compromised tumors.** *ENO1* WT U87 cells were implanted intracranially in immunodeficient NSG mice. Tumor bearing mice were treated with Avastin alone or with combination of Avastin and IACS-010759. **a-d.** Tumor volumes pre-treatment are outlined with dotted yellow lines (Day0) and post-treatment are outlined with solid yellow lines (Day 27) **(a-b)** Avastin as a single agent moderately delays tumor growth, but Avastin strongly sensitizes *ENO1* intact tumors to inhibition of mitochondrial oxidative phosphorylation, resulting in stasis of tumor growth.

Supplementary Figure 14

a

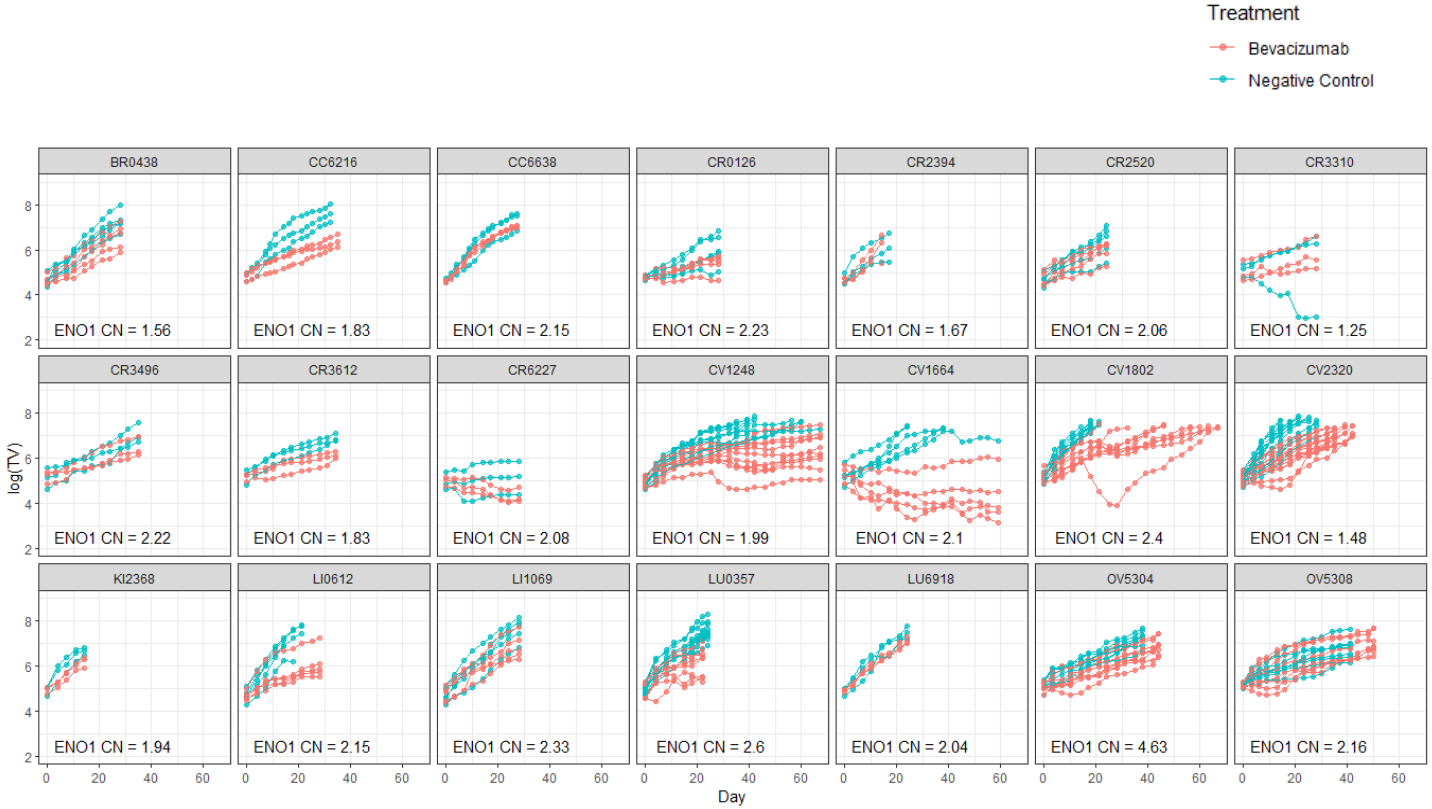

b

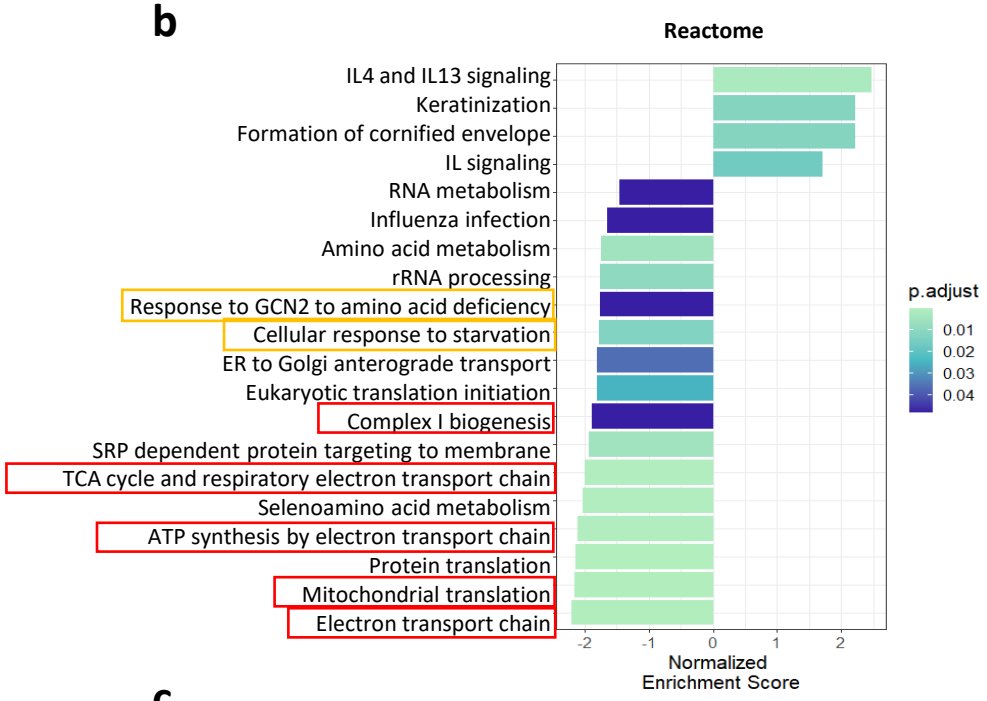

c

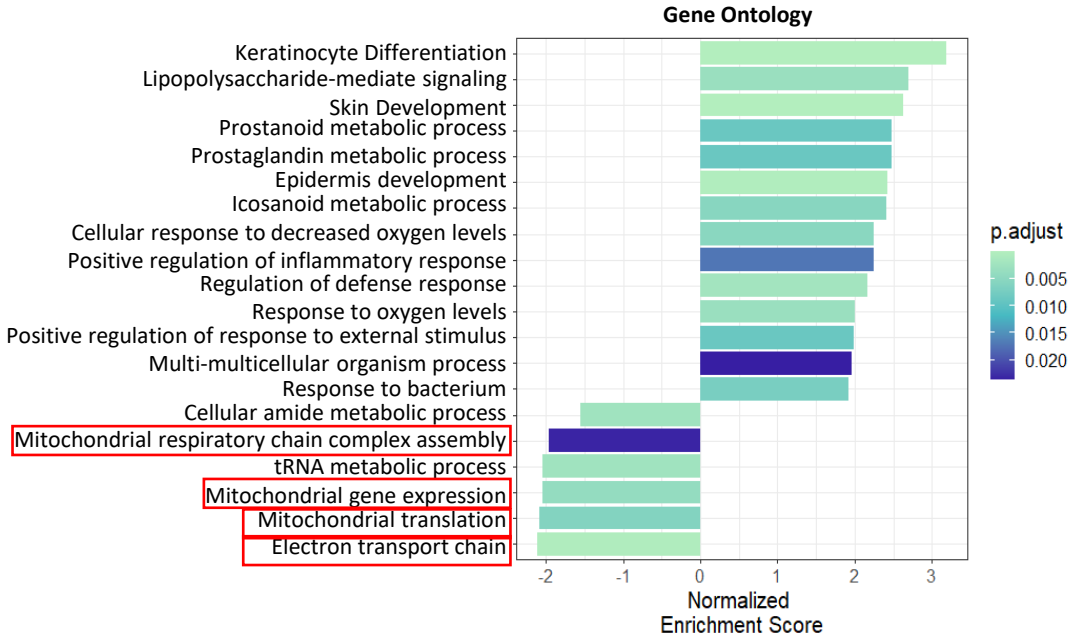

Supplemental Figure 14**: Low expression mitochondrial OxPhos gene is associated with favorable response to Avastin in a broad panel of PDXs.** PDXs in the CrownBio collection differing in anti-tumor responsiveness to Avastin (For example: CV1664 highly responsive vs CV2320 minimally responsive) none of which is *ENO1*-homozygous deleted (ENO1 CNV = 0) **a.** Relative tumor volume versus time on treatment shown for individual mice treated with vehicle group (green) and Avastin(red) dosed at 10 mg/kg IP once per week. **b-c**. The tumors were profiled (pre-treatment) by RNA seq and human transcript reads (genes expressed in malignant cancer cells) were analyzed for markers predicting response to Avastin. Tumor growth data was combined with RNAseq data to determine the effect of Avastin treatment on tumor growth as well as gene:avastin interaction for each gene. GSEA analyses and normalized enrichment scores for reactome (**b**) and gene ontology (**c**) datasets are shown. For GSEA, the significant human genes (p.adj < 0.05, n = 5419) were ranked by sign($\widehat{\beta_4}$)*****$\log_{10}$(*p*-val). A positive NES indicates that activation of the pathway synergizes with Avastin treatment, whereas a negative NES indicates an antagonistic effect. Key findings indicate that those PDXs with lower expression of TCA-cycle and mitochondrial genes (red box) showed a better response to Avastin, while those with higher expression of these genes antagonized anti-tumor effect of Avastin. Similarly, low expression of the amino acid starvation response (orange boxes) was also associated with favorable response to Avastin.